 ©2010 Uspekhi Fizicheskikh Nauk, Russian Academy of Sciences

CONFERENCES AND SYMPOSIA

PACS number: 01.10.Fv

Seventy years of the Pushkov Institute of Terrestrial Magnetism, Ionosphere and Radio Waves Propagation (IZMIRAN)

(Scientific session of the Physical Sciences Division of the Russian Academy of Sciences, 25 November 2009)

DOI: 10.3367/UFNe.0180.201005e.0509

A scientific session of the Physical Sciences Division of the Russian Academy of Sciences dedicated to the 70th anniversary of the Pushkov Institute of Terrestrial Magnetism, Ionosphere and Radio Wave Propagation of the Russian Academy of Sciences (IZMIRAN) (Troitsk, Moscow region) was held in the conference hall of IZMIRAN on 25 November 2009.

The following reports were put on the session agenda posted on the web site www.gpad.ac.ru of the Physical Sciences Division, RAS:

(1) **Gurevich A V** (Lebedev Physical Institute RAS, Moscow) "The role of cosmic rays and runaway electron breakdown in atmospheric lightning discharges";

(2) **Aleksandrov E B** (Ioffe Physical Technical Institute, RAS, St. Petersburg) "Advances in quantum magnetometry for geomagnetic research";

(3) **Dorman L I** (IZMIRAN, Troitsk, Moscow region, CR & SWC, Israel) "Cosmic ray variations and space weather";

(4) **Mareev E A** (Institute of Applied Physics, RAS, Nizhnii Novgorod) "Global electric circuit research: achievements and prospects";

(5) **Tereshchenko E D, Safargaleev V V** (Polar Geophysical Institute, Kola Research Center, RAS, Murmansk) "Geophysical research in Spitsbergen Archipelago: status and prospects";

(6) **Gulyaev Yu V, Armand N A, Efimov A I, Matyugov S S, Pavelyev A G, Savich N A, Samoznaev L N, Smirnov V V, Yakovlev O I** (Kotel'nikov Institute of Radio Engineering and Electronics RAS, Fryazino Branch, Fryazino, Moscow region) "Results of solar wind and planetary ionosphere research using radiophysical methods";

(7) **Kunitsyn V E** (Lomonosov Moscow State University, Moscow) "Satellite radio probing and the radio tomography of the ionosphere";

(8) **Kuznetsov V D** (IZMIRAN, Troitsk, Moscow region) "Space Research at the Pushkov Institute of Terrestrial Magnetism, Ionosphere and Radio Wave Propagation, Russian Academy of Sciences."

Papers based on reports 2 – 8 are published below. The main contents of report 1 are reproduced in A V Gurevich's review, "Nonlinear effects in the ionosphere" [*Phys. Usp.* **50** 1091 (2007)] and in the paper by A V Gurevich et al., "Nonlinear phenomena in the ionospheric plasma. Effects of cosmic rays and runaway breakdown on thunderstorm discharges" [*Phys. Usp.* **52** 735 (2009)].

Uspekhi Fizicheskikh Nauk **180** (5) 509 – 560 (2010)
DOI: 10.3367/UFNr.0180.201005e.0509
Translated by E N Ragozin, L I Dorman, S V Vladimirov; edited by A M Semikhatov

PACS numbers: 07.55.Ge, 91.25.G –, 93.85.Jk
DOI: 10.3367/UFNe.0180.201005f.0509

Advances in quantum magnetometry for geomagnetic research

E B Aleksandrov

The precision measurement of weak magnetic fields is a rapidly advancing area of metrology, which enjoys a wealth of applications in both fundamental and applied research. Among the former are numerous investigations in the realm of fundamental physics, geophysics, geology, cosmophysics, and aeronomy (Fig. 1).

The most prominent example of such investigations in fundamental physics in recent years is given by experiments in the search for violation of basic symmetry laws, in particular, the quest for the constant electric dipole moment of the neutron: the precision of these experiments depends entirely on the accuracy of the measurement and the stabilization of the magnetic field.

Magnetometric methods are most intensively used in geophysics, where the study of terrestrial magnetic field (TMF) variations, ranging from millisecond oscillations to secular drift, permits gathering information about the

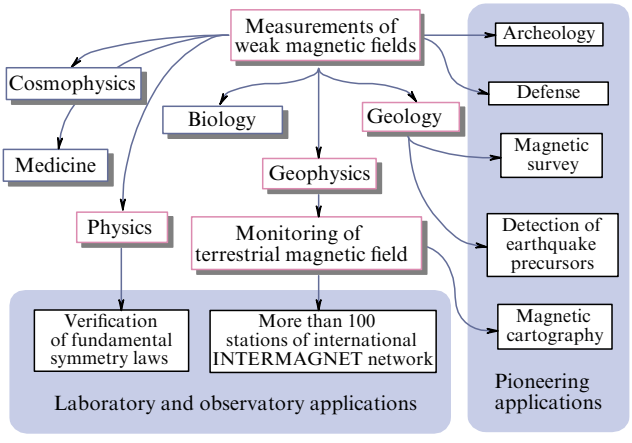

Figure 1. Main applications of quantum magnetometry.

E B Aleksandrov Ioffe Physical Technical Institute, Russian Academy of Sciences, St. Petersburg, Russian Federation
E-mail: ealexandrov@bk.ru

Uspekhi Fizicheskikh Nauk **180** (5) 509 – 519 (2010)
DOI: 10.3367/UFNr.0180.201005f.0509
Translated by E N Ragozin; edited by A M Semikhatov

evolution, structure, and current state of the earth. Vectorial measurements of TMF variations are therefore a necessary constituent of geophysical research. In particular, observations of the state of vector TMF components have been performed for over 150 years at observatories of the Pushkov Institute of Terrestrial Magnetism, Ionosphere and Radio Wave Propagation (IZMIRAN) of the Russian Academy of Sciences and at geomagnetic stations, which number about forty on the territory of the Russian Federation, the CIS, and in the Russian sector of Antarctica.

The TMF is permanently monitored by several international observatory networks. The total number of geomagnetic stations in the world amounts to over 200 in 70 countries. In particular, the International Real-Time Magnetic Observatory Network (INTERMAGNET) comprises more than one hundred magnetometric stations located in several dozen countries of the world; the Sub-Auroral Magnetometer Network (SAMNET) numbers over 20 stations; the International Monitor for Auroral Geomagnetic Effects (IMAGE) network contains 29 stations, and so on. During recent decades, in connection with the development of seismology and the transfer of a substantial part of funding to the research area aimed at prevention of extreme situations, including earthquakes, a rapid growth has occurred in the number of geophysical observatories in seismically hazardous areas, like the western coast of the USA and Southeast Asia; the instruments for these measurements are being continuously improved.

The data of magnetometric observatories, along with those obtained beginning from 1964 using quantum magnetometers on board artificial Earth satellites and explorer spacecraft, are one of the main sources of our knowledge about the internal structure of the earth, the processes occurring in it, and the interaction of solar radiation with the terrestrial atmosphere and magnetosphere.

The applications of magnetometry are primarily related to diversified problems of navigation and magnetic survey, including precision magnetic mapping for the purposes of prospecting for all kinds of minerals, both magnetic and nonmagnetic. For instance, prospecting for underwater petroleum deposits by magnetometric techniques relies on the fact that oil-bearing sedimentary rock has substantially weaker magnetic properties than other geological structures. Furthermore, magnetic mapping is widely used in archeology in searching for and dating ancient artifacts, as well as in defense, for the detection of underwater and underground military objects and ammunition. During the last few decades, precision measurements of magnetic fields in seismic zones have found increasing application for the detection of earthquake precursors. Magnetic measurements are becoming increasingly important in medicine and biology.

The demanding requirements imposed on the precision and sensitivity of magnetic measurement techniques are determined by the fact that the magnetic fields of the objects to be investigated or sought are measured in the background of the TMF, which frequently exceeds them by five or more orders of magnitude. Extracting such signals requires improving the accuracy and sensitivity of magnetometric devices to a level of $10^{-7}-10^{-9}$. Of course, this would have hardly been possible without recourse to the means of atomic and nuclear spectroscopy, which permits referencing magnetic field measurements directly to the values of atomic constants. In this respect, quantum magnetometry is very close to another branch of metrology, the metrology of time. The difference between modern quantum magnetometers and quantum frequency standards consists only in the fact that the principle of operation of the former involves frequency measurements for magnetically dependent transitions, while the principle of operation of the latter is based on frequency measurements for magnetically independent transitions in the same atomic structures. The relative precision attained due to the use of quantum magnetometers in the metrology of weak magnetic fields is second only to the precision of frequency (time) measurements.

1. Quantum magnetometry: brief history and current state of the art

Magnetometry as an area of high-precision investigations began with the making and use of classical devices for the measurement of magnetic fields, which recorded the action of a field on permanent magnets, moving charges, etc. These devices are typically characterized by considerable drifts and do not permit combining a high variational sensitivity (i.e., the capability of recording a small increment of the quantity being measured) and the absoluteness of measurements, which implies the ability to perform measurements relying only on fundamental and atomic constants.

The prerequisites to the advent of quantum magnetometry emerged in 1896, when P Zeeman discovered the effect of spectral line splitting in a magnetic field. In the 1930s, Rabi undertook several investigations to measure nuclear magnetic moments [1]. Quantum magnetometry had its genesis in the 1940s, when Bloch [2] and Varian and Packard [3] came up with the idea of measuring magnetic field strength from the frequency of free precession of the magnetic moment of a proton. The first proton magnetometers were thus made, which were the first devices for the inherently absolute measurement of magnetic fields.

Since that time, magnetometers have been subdivided into classical and quantum ones (Fig. 2); there are two main types of quantum magnetometers: instruments with superconducting sensors, so-called SQUIDs (superconducting quantum interference devices), which are not discussed in this review, and devices that use the Zeeman effect in an atomic structure in one way or another. Among these devices, the highest performance characteristics are exhibited by optically pumped quantum magnetometers (OPQMs) realized with different, primarily alkali, atoms.

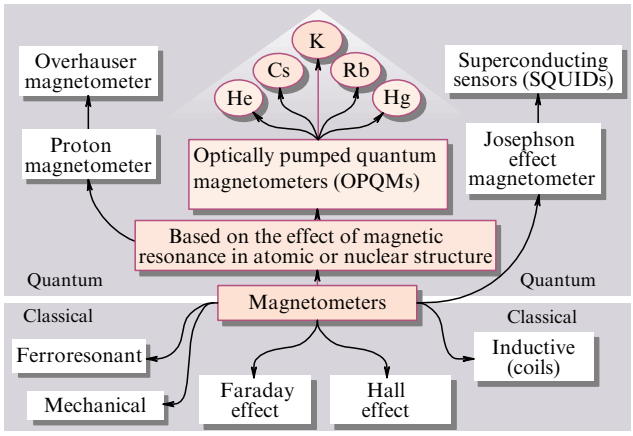

Figure 2. Classification of the main types of magnetometric devices.

Despite the numerous virtues inherent in proton magnetometers, their three main disadvantages limited their area of application, namely: the cyclic mode of operation, which does not allow continuous field measurements; a very low magnitude of static nuclear susceptibility; and a relatively low proton precession frequency, which necessitates no less than several tenths of a second to precisely measure the frequency.

The second of these disadvantages was largely overcome due to Overhauser [4, 5] and Carver and Slichter [6], who demonstrated the feasibility of more than a thousand-fold increase in the proton spin polarization degree and therefore in the proton magnetometer signal using the technique of dynamic polarization of atomic nuclei. The magnetometer based on this principle has come to be known as the Overhauser magnetometer.

The beginning of radio–optical quantum techniques of measuring a magnetic field was initiated by two events that occurred almost simultaneously in the middle of the 20th century:

(i) the invention by Bitter of the optical detection of magnetic resonance [7], which allowed realizing a detection sensitivity several orders of magnitude higher than that for the direct electromagnetic technique;

(ii) Kastler's discovery [8, 9] of optical pumping, an effect whereby the irradiation of atoms by specifically polarized resonance light allows obtaining an extremely high degree of magnetic moment orientation.

These events triggered a rapid development of quantum magnetometry, which led to the making of a family of quantum magnetometers with optical pumping and optical detection of magnetic resonance and enabled attaining an extraordinarily high absolute precision and sensitivity in the measurement of magnetic fields [10–14]. Being unrivaled in absolute sensitivity, quantum magnetometers may even exceed the magnetometers based on SQUIDs in variational sensitivity [15]. However, the competition between these two classes of devices is largely nominal: the physical principles of their operation and, as a consequence, their areas of application differ greatly. Quantum magnetometers are meters of the absolute magnetic field strength, while magnetometers with superconducting sensors are meters of the increment of the magnetic flux through a superconducting circuit.

Due to their supersmall sensor size and high sensitivity, SQUIDs occupy a prominent place in biology and medicine; however, they are hardly employed in geology, geophysics, and cosmophysics. In the subsequent discussion, in order to avoid confusion, the term quantum magnetometer is used in reference only to devices with optical pumping, thereby excluding proton magnetometers and SQUIDs from our consideration.

1.1 Classification of quantum magnetometers

Quantum magnetometers may be classified by the character of paramagnetism of the working substance (electronic or nuclear) and the type of atomic transition in use (Zeeman, hyperfine, multiphoton, and so on); by the method of magnetic resonance excitation; by the way magnetic resonance is detected (recording the variation of magnetic sublevel populations in M_z magnetometers; recording the coherence signal of atomic states in M_x magnetometers). Furthermore, recent decades have seen the emergence of many modifications of the idea of a quantum magnetometer that go beyond the scope of the main classification.

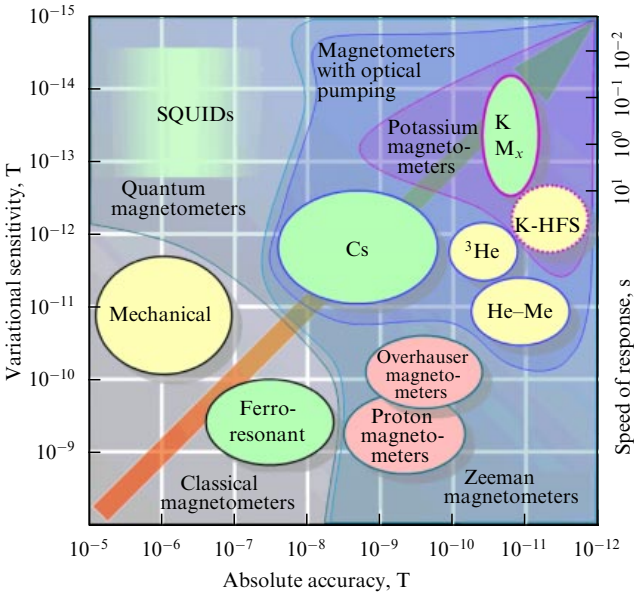

Figure 3. Classification of magnetometer devices by their main metrological parameters.

Figure 3 shows an approximate classification of modular magnetometric devices by the main metrological parameters: short-term sensitivity, precision, and the speed of response. Shown in Fig. 3 are the following resonance magnetometers: cesium (Cs) and potassium (K) M_x magnetometers, a potassium (K-HFS) hyperfine-structure M_z magnetometer, a nuclear helium (^{3}He) M_x magnetometer, and an alkali helium (He–Me) M_z magnetometer. The arrow in the diagram shows the general trend in the development of magnetometric devices. A remark is in order: the data depicted in Fig. 3 are not necessarily complete or perfectly reliable. Direct measurement of the parameters of high-precision devices is impossible when these devices outperform reference devices. Furthermore, some of the listed magnetometers measure quantities that are different from the magnetic induction modulus. The performance of commercial magnetometers claimed by their manufacturers is quite often higher than the results of independent tests, which is especially characteristic of small private companies. Therefore, Fig. 3 is intended to give no more than a general impression about the current situation in magnetometry.

Quantum sensors are also used in the so-called vector, or three-component, magnetometers, which measure the three components of the TMF. The principle of operation of vector magnetometers usually relies on the law of composition of vectors: differently directed known vectors are successively added to the unknown induction vector of the field under measurement and the modulus of the resultant field vector is measured, and the unknown vector is calculated in this way.

Quantum magnetometers may be validly used to measure not only the modulus and components of the magnetic induction vector but also vector components of the gradient of the magnetic induction modulus. In the simplest configuration, a magnetic gradiometer consists of two (or, in extended versions, of three or more) magnetometers spaced at a fixed distance from each other.

It is also possible to configure devices for measuring the second- and higher-order gradients of the magnetic field modulus, as well as the gradients of magnetic vector

Table 1.

Characteristic	INTERMAGNET specifications	OPQM-based magnetometric complex	Gain
Variational sensitivity in the 0.2 Hz band	0.1 nT	0.002 nT	50 fold
Frequency band	0.2 Hz	5 Hz	25 fold
Speed of response	5 s	0.1 s	50 fold
Long-term stability	5 nT yr^{-1}	0.2 nT yr^{-1}	25 fold
Measurement accuracy	$\pm$10 nT	0.2 nT	50 fold

components. However, these systems consist of a large number of modular or vector sensors and are infrequently used (an example is provided by the experiment in the search for the electric dipole moment of the neutron mentioned above).

Although the property of absoluteness of measurement is immanent in quantum meters of magnetic fields, this property may be largely lost in certain cases because of the presence of additional magnetic fields in the sensor, the broadening, shift, or shape distortion of the resonance line, and so on. Those measuring devices that have a high short-term sensitivity but no absolute precision belong to the class of variometers.

Table 1 gives the characteristics of the OPQM-based vector magnetometric complex developed jointly by the Ioffe Physical Technical Institute (PhTI) of the Russian Academy of Sciences and the Vavilov State Optical Institute (SOI). These characteristics are compared with those corresponding to the specifications of the INTERMAGNET international magnetic observatory network.

Quantum magnetometers are additionally classified by their service conditions (stationary observatory devices, vehicle-borne magnetometers, portable devices, and so on); by the way information is extracted (analogue and digital); by the class of accuracy; and so on.

2. Basic physical principles of quantum magnetometry

2.1 Optical pumping and double radio–optical resonance

Proton magnetometers, which afford the absolute measurement accuracy up to 1 nT for a resolution up to 0.1 nT, are still used in magnetic field metrology and in many magnetic observatories. But despite the obvious advantages of these magnetometers, the following disadvantages must be overcome:

1) the cyclic nature of operation, which does not allow continuous field measurements;

2) low sensitivity, which is due to the low magnetic susceptibility of a nuclear paramagnetic;

3) low proton precession frequency, which limits the speed of the instrument response;

4) linear dependence of the sensitivity on the magnitude of the field being measured, which hampers measurements of weak fields;

5) substantial energy consumption arising from the necessity of inducing a strong field.

These disadvantages were largely overcome in a substantial proton magnetometer modification based on of the Abragam–Overhauser effect — the effect of dynamic polarization of nuclei, which permitted abandoning the polarizing field and increasing the degree of proton polarization by 2 – 3 orders of magnitude.

The further development of the idea of a magnetometer reliant on the effect of magnetic moment precession was possible along three main lines: (i) increasing the oscillation frequency to improve the speed of response and sensitivity of the instrument; (ii) increasing the degree of polarization of the working paramagnetic; and (iii) abandoning the inductive extraction of the precession signal. All these tasks were solved, first, by passing from nuclear paramagnetism to electron paramagnetism (with an increase in the gyromagnetic ratio by 2 – 3 orders of magnitude) and, second, by applying the technique of optical pumping and double radio–optical resonance.

The essence of optical pumping consists in the selective optical population of magnetic and/or hyperfine sublevels of an excited atomic state.

We consider a ground state with two sublevels, 1 and 2, and an excited state (Fig. 4). By selective pumping of sublevel 1 of the ground state, it is possible to decrease the population of sublevel 1 at the expense of increasing the population of sublevel 2 if the probability of transitions between sublevels 1 and 2 is low in comparison with the optical excitation probability.

The optical pumping that results in the emergence of a nonzero dipole magnetic moment in a substance is referred to as optical orientation. Optical methods also exist for inducing a quadrupole magnetic moment (ordering) and higher-order moments. The physical foundations of optical pumping are set forth in several publications, beginning from the 1950s; we note the prominent review Ref. [16].

The method of double radio–optical resonance (DRR) is commonly used in combination with optical pumping. The

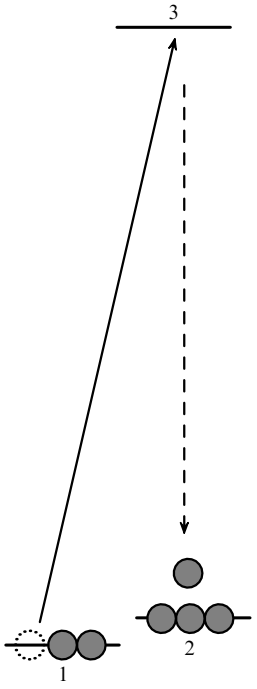

Figure 4. Optical pumping in a three-level scheme.

heart of this method is that the optical resonance excitation of atoms is combined with the induction of radio frequency transitions between sublevels of the ground or excited states. In this case, every event of absorption (or stimulated emission) of a radio frequency photon is attended with the absorption or spontaneous emission of an optical photon. Detecting absorption (emission) in the optical range usually permits increasing the sensitivity of magnetic resonance detection by many orders of magnitude in comparison with that in conventional radiospectroscopy methods, because the energy of the optical photon exceeds the energy of the radio frequency photon by many orders of magnitude.

In 1949, A Kastler proposed detecting magnetic resonance from the variation of intensity and polarization of light emitted by atoms. The success of this technique was primarily predetermined by the possibility of ensuring a low relaxation rate between sublevels 1 and 2. In his first experiment, Kastler used the atomic beam technique to eliminate the relaxation of atoms in the ground state, such that the atoms of the beam experience practically no collisions along the entire trajectory length. The atomic relaxation time, which amounted to the atomic transit time, was of the order of 10^{-4} s.

The next step involved passage to gas cells. It was experimentally determined that the relaxation of angular momentum caused by collisions with vessel walls may be prevented by filling the vessel with a special buffer gas, which moderates the diffusion of oriented atoms to the wall but does not disrupt their orientation.

Similar results, and even better ones than with buffer gas filling, may be obtained by depositing a paraffin or polysiloxane coating on the inner cell surface. These coatings are characterized by an anomalously low adsorption energy for alkali atoms, with the result that the atomic residence time on the walls (of the order of 10^{-10} s) is so short that an appreciable relaxation of electron spins has no time to occur.

In the overwhelming majority of radio–optical magnetometers, the magnetic resonance technique is used whereby the transition frequency between the magnetic sublevels is determined by irradiating the polarized specimen with a probing monochromatic radio frequency field $\mathbf{B}_1$. The magnetic resonance equations with the inclusion of relaxation processes were first written by Bloch [17]. It is easy to derive their stationary solution for the three components of the magnetic moment vector, which are denoted by M_z, v, and u ($v \| \mathbf{B}_1$, $u \perp \mathbf{B}_1$) in the reference frame rotating with the radio frequency about the z axis ($z \| \mathbf{B}$).

According to the Bloch equations, the u component vanishes at the exact resonance, and therefore the transverse component of the angular momentum precesses with a 90° shift relative to the field vector $\mathbf{B}_1$. The per-unit volume absorption of the alternating field energy by the system is defined by the v component, and the u component defines dispersion.

Multiquantum transitions, which may also be validly used in magnetometric devices, are possible in multilevel systems. These processes, which were theoretically predicted in 1929 [18], were experimentally observed for the first time just in the radio frequency range, where it is much easier to reach the requisite spectral power density of electromagnetic radiation [19].

Recently, multiquantum resonances have been finding progressively wider use in quantum magnetometry. These are primarily (i) multiquantum higher-order $n-1$ transitions that link up a system of n quasiequidistant Zeeman levels of one hyperfine state, and (ii) the so-called Λ scheme (see Fig. 4), in which two lower levels, 1 and 2, are linked to the common excited level 3 by two coherent waves whose frequency difference corresponds to the spacing of the lower levels. Under resonance conditions, levels 1 and 2 turn out to be linked together by a two-quantum transition, and coherence emerges between them without populating the intermediate level 3. This effect has been known under many names, among which dark resonance [20], the effect of coherent population trapping [21], and electromagnetically induced transparency [22] are most frequently used.

3. Quantum magnetometers with optical pumping

3.1 Types of magnetic resonance signals and the main versions of quantum magnetometers

Magnetic resonance techniques involve two kinds of observable quantities proportional to the imaginary and real components of the magnetic susceptibility. Accordingly, there are two types of magnetic resonance signals, which are related to the observation of (i) the longitudinal component of the magnetic moment, i.e., permanent magnetization (M_z signal), and (ii) its transverse component, which is described by the variables u and v (M_x signal).

In the M_z-signal case, locking in to the resonance line center requires introducing a low-frequency modulation of the mismatch and using a conventional method of synchronous detection for determining the frequency mismatch $\Delta\omega$.

In the M_x-signal case, it is possible to record the v and u components separately; in particular, it is possible to extract the signal proportional to u, whose contour has a dispersion shape as a function of $\Delta\omega$. Just this form of the signal is most convenient when the resonance is used as a frequency discriminator: at exact resonance, the signal is equal to zero, and in the case of a mismatch, the sign of the signal bears information about the mismatch sign. However, careful control over the phase of the whole signal path is required in this case. Accordingly, magnetometers are distinguished by the way of detecting the magnetic resonance:

1) relatively slow but typically more exact M_z magnetometers;

2) fast-response M_x magnetometers.

In all commercially available radio–optical magnetometers, electronic paramagnets (alkali atoms (Fig. 5) or the metastable atoms of ^{4}He orthohelium (2^3S_1)) are used as the working medium. Alkali metal vapor magnetometers are encountered most frequently; among them are the historically first but now infrequently used rubidium magnetometer, the substantially more popular cesium magnetometer, and a relatively new potassium one.

The vapors of all alkali metals permit an efficient optical orientation: their strongest lines of the first resonance doublet fall into a convenient optical region, from the visible light to the near infrared.

Resonance transitions between the Zeeman sublevels of one hyperfine structure (HFS) level are commonly used in OPQMs; however, OPQMs exist that use transitions between the Zeeman sublevels of different HFS levels (so-called HFS magnetometers) and of multiphoton transitions.

All presently existing commercially available alkali metal vapor magnetometers use radio frequency transitions. HFS

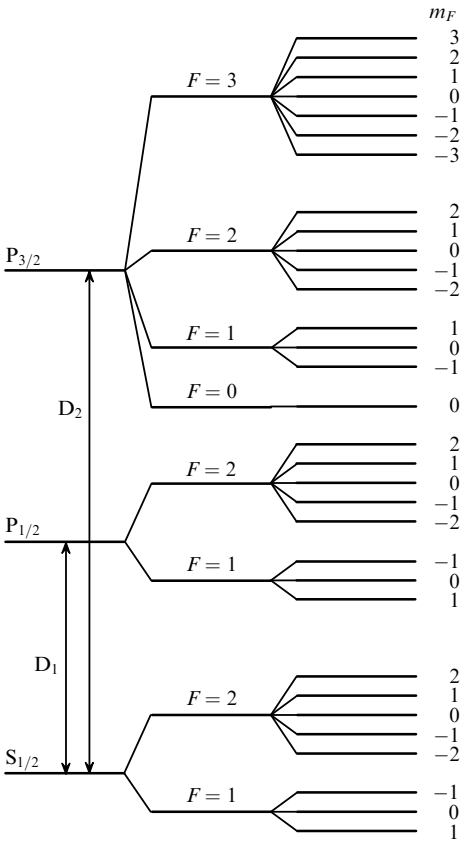

Figure 5. Energy level diagram of an alkali atom with the nuclear spin 3/2 (^{7}Li, ^{23}Na, ^{39}K, ^{41}K, ^{87}Rb isotopes).

magnetometers are mostly known as laboratory and pilot facilities, although they offer certain advantages: in particular, they are characterized by exceptionally high absolute accuracy.

Basically, a resonance quantum magnetometer is a radio spectroscope that automatically tunes to the magnetic resonance line center, which permits determining the magnetic field strength from the resonance frequency. At present, the majority of alkali metal vapor magnetometers are designed according to the M_x scheme, because this magnetometer type is attractive for its inertialess response to magnetic field variations.

3.2 Main metrological characteristics of quantum magnetometric devices

The main metrological characteristics of an OPQM are precision, variational sensitivity (or resolving power), and the speed of response. These parameters are fundamentally limited by the magnetic resonance parameters: the width and the symmetry of the resonance line, the magnitudes of parametric resonance shifts, and the signal-to-noise ratio. A model that allows optimizing the sensitivity of the atomic discriminator to the first approximation was constructed in Ref. [23].

The smaller the width of atomic resonances is, the greater their attractiveness for quantum metrology. But a narrow resonance poses a problem arising from its inertia. Although the M_x magnetometer scheme is not limited by the resonance linewidth as regards the speed of response, this statement is perfectly true as long as the measurement period is not much shorter than the inverse linewidth. On the other hand, for long measurement periods, which characterize precision and long-term magnetometer stability, different drifts and ageings prevail, which are statistically described by the dependences of the variance of readings on the measurement time such as $\sigma(\tau) \sim \tau^{1/2}$, $\sigma(\tau) \sim \tau$, and so on. It is significant that the scale of errors generated by all these factors is proportional to the resonance width Γ.

Apart from the variational sensitivity and the speed of response, a highly important metrological characteristic of magnetic field meters is their absolute accuracy, or the accuracy with which the measured induction value can be expressed in terms of the fundamental constants. In particular, the limiting absolute accuracy of a resonance magnetometer utilizing a narrow isolated potassium line (potassium magnetometer) is determined by the uncertainty in the electron g-factor g_j (which relates the projection of the electron magnetic moment expressed in terms of the Bohr magneton μ_B to the magnetic quantum number m_j), μ_B, and $\hbar$: in a typical TMF, the limiting absolute accuracy of a potassium magnetometer may in principle be about 10 pT. In a potassium magnetometer, the systematic measurement errors of the magnetic resonance frequency may also be reduced to $\sim$ 10 pT because such are the characteristic shifts and uncertainties in measurements of the magnetic resonance frequency in the spectrum of potassium.

3.3 Self-oscillating magnetometer with cesium vapor

At present, a self-oscillating magnetometer with cesium vapor is probably the simplest and most widespread of all quantum devices. The ground state of ^{133}Cs consists of two hyperfine levels with total angular momenta $F = 3$ and $F = 4$, which in a magnetic field respectively split into 7 and 9 sublevels. The magnetic resonance frequencies between adjacent magnetic sublevels of one hyperfine cesium level differ by only ≈ 7 Hz in the average TMF. That is why the set of resonances virtually merge into one common asymmetric contour approximately 50 Hz in width, which corresponds to ≈ 15 nT on the magnetic field scale. This line of resonance between the sublevels of the $F = 4$ state is schematically depicted in Fig. 6 for the TMF.

Because the contribution of different partial resonances to the common line depends heavily on the light and radio field strengths, the direction of the pump light relative to the permanent field direction, the cesium vapor density, and other factors, variations of these parameters introduce uncertainty in the readings. As a result, the cesium magnetometer accuracy does not typically exceed several nT. The dashed line in Fig. 6 shows the line shape variation under the variation of the mutual orientation of the magnetic vector and the direction of the pump light. As is evident from Fig. 6, the

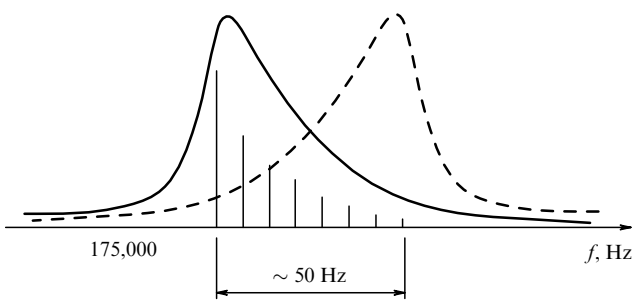

Figure 6. Shape of the magnetic resonance line of Cs in the TMF.

greatest orientation error is close to the spacing of the extreme lines in the resonance spectrum, i.e., ≈ 15 nT in the average TMF.

To suppress orientation shifts and drifts, several tricks are used to symmetrize the resonance (multicell and multizone systems [24–26]), which permit decreasing the orientation shifts to several tenths of an nT.

A cesium magnetometer remains the simplest, most reliable, and most widespread device among quantum magnetometers, and the field of its application is progressively widening. To an extent, this is due to the emergence of available laser pump sources for Cs. An example is provided by a cardiogradiometer with laser-pumped Cs-M_x sensors, which exhibits the sensitivity about 100 fT $Hz^{-1/2}$ for the cell size 20 mm [27].

3.4 Nuclear helium magnetometer

In special cases where a high speed of response is not required, nuclear paramagnetic vapor magnetometers, which are characterized by very long relaxation times, may be the magnetometers of choice. In particular, the optically polarized ^{3}He parahelium nuclei 1^1S_0 in a gas cell whose walls are coated with a monolayer of cesium exhibit the relaxation time up to 1 day. This permits making a unique magnetometer with an inductive readout of the signal of freely precessing helium nuclei, which consumes virtually no energy in the interval between infrequent cycles of optical pumping.

Nuclear helium magnetometers have not gained wide acceptance, first, because of their low speed of response and, second, due to their large weight and size (picking up the signal requires induction coils weighing many kilograms), and, third, owing to the vulnerability of the detecting coils to radio frequency noise. Furthermore, because of the low frequency of nuclear precession, the magnetometer turned out to be sensitive to gyroscopic errors.

Among the virtues of a nuclear helium magnetometer are its practically infinitely narrow line and the capability of operating independently under nonperturbing conditions for a day or more upon completion of a pumping cycle. A semiconductor laser-pumped magnetometer with the sensitivity about 50 pT in the 70 Hz band was described in [28]. In the design of optically pumped nuclear magnetometers, apart from ^{3}He, the ^{199}Hg and ^{201}Hg mercury isotopes were used.

3.5 ^{4}He magnetometer with optical pumping

The optical pumping of atomic ^{4}He in the metastable state was first described in Ref. [30]; since then, a start has been made on the development of atomic ^{4}He magnetometers [31–33]. The principle of their operation involves excitation of atoms to a metastable state, direct optical pumping (polarization) of the 2^3S_1 metastable helium atoms, excitation of the M_z resonance, and optical detection of the M_z signal.

In the most modern modification of the helium magnetometer [34], which used laser pumping of the $2^3S_1 - 2^3P_0$ transition and the frequency modulation of laser radiation in the optical detection of the signal, a sensitivity of the order of 1–4 pT $Hz^{-1/2}$ was reached.

3.6 Alkali–helium magnetometer

An alkali–helium magnetometer is an instrument that may be realized only in the form of an M_z scheme. This instrument uses the effect of spin polarization transfer from oriented alkali atoms to helium in the metastable 2^3S_1 state (orthohelium) in collisions of particles under alkali–helium gas-discharge plasma conditions [35].

The leading role in the development and making of the alkali–helium magnetometer was played by R A Zhitnikov's group (PhTI). Nowadays, the alkali–helium magnetometer is significantly exceeded by potassium magnetometers in sensitivity, precision, and speed of response.

3.7 Isolated narrow-line potassium magnetometer

In the TMF, potassium, unlike cesium and other alkali metals, has an almost completely resolved system of magnetic resonances in the ground state, which permits separating one isolated line and largely ignoring other lines of the spectrum.

The spectrum of magnetic resonances of a natural potassium isotope mixture is schematically shown in Fig. 7. The location of the peak of the strongest and most isolated line is barely dependent on the pumping conditions; the frequency shift of the leading resonance under the influence of the neighboring one does not exceed 0.3 pT in the average TMF, which is four orders of magnitude lower than the systematic error of a cesium magnetometer.

Although the first attempts of using potassium in the OPQM scheme were undertaken back in the 1960s [36], they did not meet with success because of the complexity of working with a structure containing several resonance lines. The first M_x-version magnetometer using the isolated narrow line of potassium was made at SOI [37, 38]; this research is presently being continued at PhTI.

It was in the potassium vapor scheme with a cell 15 cm in diameter with laser pumping that the variational sensitivity 1.8 fT $Hz^{-1/2}$ was reached, which is record-breaking for OPQMs.

3.8 HFS magnetometer

An OPQM based on microwave resonance in the hyperfine structure of the ground state of an alkali metal atom (an HFS magnetometer) was proposed in the 1970s [39]. These schemes offer a number of advantages over the traditional OPQM scheme. First, the Zeeman structure of the majority of HFS transitions turns out to be resolved even in hyperweak fields (of the order of 10^{-7} T). Second, with an HFS magnetometer, it is possible to realize a magnetometer without 'blind zones.' Third, the systematic errors of such a magnetometer may be suppressed to ~ 1 pT by realizing the so-called balance

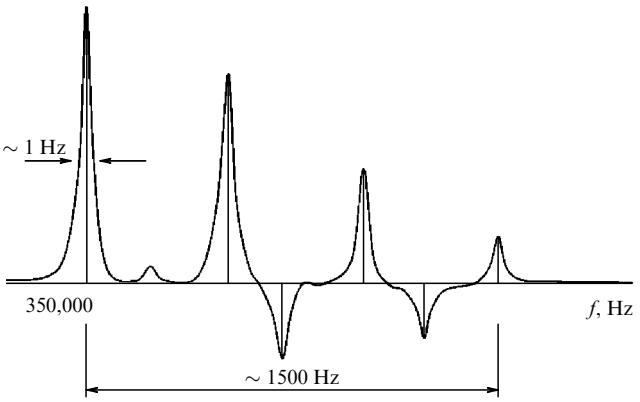

Figure 7. Magnetic resonance spectrum of K in the TMF.

magnetometer version, which measures the frequency difference for transitions between two symmetric pairs of magnetic levels. For optical pumping by unpolarized light, this difference is virtually free from light shifts.

The project of a ^{39}K vapor HFS magnetometer was comprehensively investigated in the 1970s [40]. A sensitivity about 1 pT Hz$^{-1/2}$ was demonstrated in the course of its tests.

It was suggested that ^{87}Rb HFS magnetometers would enable attaining a substantially higher sensitivity: the HFS splitting of the ground state of ^{87}Rb is approximately 15 times that in ^{39}K, which permits effecting a high-efficiency pumping of the hyperfine sublevels of the ground state. But it turned out that an additional source of noise arising from the insufficiently high frequency stability of the reference microwave generator emerges in this case [41]. This problem is solved by replacing reference quartz generators by higher-Q ones, in particular, masers and lasers.

In the case of a balance HFS magnetometer, the necessity of simultaneously measuring the frequencies of two microwave transitions results in a substantial complication of the electronic part of the instrument. Only recently has it been possible to completely overcome this drawback using modern methods of frequency synthesis [42].

3.9 $M_z - M_x$ tandem

In metrology, the requirements of response speed and high measurement accuracy quite often contradict each other, which is resolved by combining two measuring devices into an integrated system, where the readings of the fast device are corrected with the help of the second device, which is slower but more precise [43]. The corresponding device, which is frequently referred to as a tandem, may be a combination of two OPQMs: one of them is based on the spin generator scheme (M_x OPQM), whose output frequency automatically follows the induction of an external field, and the other (M_z OPQM) operates according to the scheme of a passive radiospectrometer locked in to the frequency of the selected magnetic resonance line by means of a feedback loop. In this case, the M_z OPQM uses the magnetic resonance spectrum with a resolved line structure, which affords a high precision of frequency measurements.

In the first tandem [43], rubidium ^{87}Rb isotopes were used; the next version [44] involved cesium in the M_x scheme and potassium in the M_z scheme: unlike the spectrum of rubidium, the magnetic resonance spectrum of potassium is reliably resolved throughout the TMF range. The magnetometer was characterized by the response time 1 ms, resolution 10 pT, and the absolute accuracy ≈ 0.1 nT.

In [45], a Cs – K tandem was described that differed in two parameters simultaneously: first, instead of two sensors, only one sensor containing a Cs – K vapor mixture in a paraffin-coated flask was used, which completely eliminated the problems related to the gradient of the magnetic field. Second, for an M_z resonance, the authors used a four-quantum resonance $m_F = -2 \leftrightarrow m_F = 2$ of the $F = 2$ sublevel of the ground state of K. This was the first use of the special properties of the higher (for the $F = 2$ level) multiplicity resonance $n = 4$, which is hardly shifted by the alternating field [46]. The unique properties of this resonance were investigated in Refs [47, 48]. The readings of the tandem were shown to be stable to within 10 pT under changes in the main parameters by values that were known to exceed their reasonable operational variations.

3.10 Potassium magnetometer utilizing a narrow line with suppressed spin-exchange broadening

One of the main factors responsible for the broadening of resonance lines is the spin-exchange broadening, which is proportional to the density of atoms in the working cell. This limits the possibility of improving the sensitivity of a quantum magnetometer by increasing the optical cell density. However, in 1973, Happer and Tang [49] discovered experimentally that the spin-exchange broadening may be decreased by increasing the atomic density in hyperweak magnetic fields. Four years later, this effect was substantiated theoretically [50].

Since 2002, this effect has been studied by a Princeton University group headed by M Romalis [51 – 54]. In hyperweak magnetic fields (of the order of 10 nT) in a potassium vapor cell at the temperature 170 °C, it was possible to record a resonance width of only a few Hertz, and a sensitivity of the order of 1 fT Hz$^{-1/2}$ was obtained; meanwhile, even for the magnetic field strength of 300 nT, the resonance width amounted to 350 Hz.

3.11 Magnetometer projects using the effect of coherent population trapping

An attempt to use the effect of coherent population trapping (CPT) in the microwave region in quantum magnetometry was first undertaken in [55]. The first reports about the implementation of a magnetometer reliant on a purely optical CPT effect (see [56]) date back to 1998. In Ref. [56], cesium atoms were simultaneously irradiated by the light of two lasers with frequencies spaced at 9.2 GHz, i.e., at the frequency of the CPT splitting of the ground state of Cs. The authors concluded that the magnetometer resolution was equal to ~ 500 fT.

In the scheme investigated in [57], two independent lasers were replaced by one laser with the radiation modulated at the frequency 4.6 GHz. The authors noted that although the 'dark' optical CPT resonance did not experience broadening by the power of laser radiation, it turned out to be broadened due to an inhomogeneous Stark shift, which radically impaired the sensitivity. Proceeding from the signal-to-noise ratio and the resonance width, the authors of Ref. [57] estimated the sensitivity of their magnetometer to be 4 pT for the measurement period 1 s and longer. The research is being pursued in parallel in the National Institute of Standards and Technology (NIST), USA [58, 59], the Lebedev Physical Institute (FIAN) of the Russian Academy of Sciences, and the Institute of Laser Physics (ILPh) of the Siberian Branch of the Russian Academy of Sciences [60].

Magnetometer based on the effect of nonlinear magneto–optical rotation. The nonlinear effect of magneto–optical rotation (the nonlinear Faraday effect) consists in the fact that the polarization rotation angle of quasiresonance light depends on both the magnetic field and the light intensity. The idea of using the effect of polarization rotation emerging in the resonance frequency modulation of a pump light was proposed in [61, 62].

This effect is close to the effect of parametric resonance, which occurs when a harmonic system is irradiated by light at a frequency that is a multiple of the resonance frequency of the system: the light tuned to resonance with the optical transition aligns magnetic moments along the field. When the light frequency is modulated with a frequency Ω_m, the resonance condition is satisfied twice during the modulation period; therefore, the properties of the medium vary with the

frequency $2\Omega_m$. When this frequency coincides with the Larmor frequency $\omega = \gamma B$, where γ is the gyromagnetic frequency (the ratio of the magnetic moment of the atom to its mechanical moment), a parametric resonance occurs.

In their experiments, the authors of [61, 62] observed 1.3 Hz wide resonances, which according to the estimates of the authors, should furnish a sensitivity of the order of 10^{-11} G $Hz^{-1/2}$ (or 1 fT $Hz^{-1/2}$) in hyperweak magnetic fields ($\ll 100$ nT).

3.12 Vector magnetometry with the use of quantum sensors

Quantum magnetometers are scalar, or modulus, instruments that offer a considerable advantage over all other instruments for measuring magnetic fields: their readings are barely dependent on the direction of the magnetic field. Nevertheless, it is due to precisely this property that quantum magnetometers are used for the measurement of the magnetic vector components.

The feasibility of using a scalar sensor in vector magnetometry relies on the dependence of the modulation phase of a probe beam on its direction relative to the magnetic field. A version of this measuring scheme was considered in Ref. [63]. Two beams are used in the scheme: beam L1, which is parallel to the field being measured, and beam L2, which is perpendicular to the first one. Beam L1 effects the optical pumping of alkali metal atoms and beam L2 is used as the probing one.

When beam L1 is exactly parallel to the magnetic field, its modulation is absent. When the magnetic field deflects from the beam direction by an angle Θ, a modulation signal emerges with the amplitude proportional to $\sin\Theta$ and the phase depending on the direction of the magnetic field deflection. Therefore, this scheme permits measuring the field modulus and two of its transverse components. According to the authors' estimates, the device is characterized by the variational sensitivity about 0.1 nT in 1 s in the measurement of transverse field components and by drifts of the order of 2–3 nT per day.

Numerous systems based on the methods of calibrated magnetic field perturbation involve scalar sensors placed in a three-dimensional system of magnetic rings producing a sequence of artificial fields perpendicular to the field being measured; these methods are reviewed in Ref. [64].

Among the successful realizations of vector magnetometers that use alkali metal vapor sensors, we note Refs [65, 66]. Their main distinction, apart from the use of an optically pumped sensor, is the continuous fast rotation of an auxiliary transverse magnetic field. As a result, at the center of the system, a magnetic field forms whose vector rotates in a cone relative to the TMF vector.

In the measurement of transverse TMF components, the axis of the total magnetic vector at the center of the system deflects from the TMF vector, resulting in the modulation of the modulus of the vector at a frequency f. The signal at the modulation frequency f is used to produce fields that completely cancel the corresponding transverse TMF components. The instrument version described in Ref. [66] also compensates 90–95% of the TMF, which permits increasing the sensitivity of measuring the transverse field components by almost an order of magnitude. An instrument based on this principle exhibited an rms intrinsic noise at the level of 0.010–0.015 nT for the measurement period 0.1 s.

These instruments belong to the class of variometers: their measurements are not inherently absolute because additional fields induced by the systems of magnetic rings are added to the field under measurement. A way of simultaneously measuring three TMF vector components was proposed in [67] based on an optically pumped M_x magnetometer, which is characterized by a high absolute accuracy; the short-term sensitivity of measurements is then determined by the sensitivity of the M_x magnetometer.

The essence of the method is as follows. In the sensor region, a system of compensating fields is produced, which alternate harmonically such that the total magnetic vector in the sensor rotates, with its length conserved, about the initial direction of the magnetic field. In each rotation cycle, the vector passes through three positions in which two components of the magnetic field are compensated with a high precision, while the third component, by contrast, is not compensated at all and may be measured. It is shown that using an optically pumped M_x magnetometer and a three-component symmetric system of magnetic rings for a sensor allows simultaneously measuring the three components of the TMF vector with the absolute precision ± 0.1 nT for the measurement period 0.1 s, which may not be accomplished by any presently existing techniques.

3.13 Summary

Quantum magnetometers with the optical pumping of alkali metal vapor may be used to advantage in a variety of geophysical problems that require measurement of the modulus and gradients of a magnetic field, as well as of the components of a magnetic vector. Tasks that simultaneously require a high accuracy and a high speed of response may be carried out by combining quantum measuring devices of various types. For all the diversity of the methods for exciting and detecting magnetic resonance, the major avenue of development of the systems for magnetic field measurements involves narrowing the magnetic resonance line. In the range of TMFs, this implies the use of atomic structures having a well-resolved spectrum like the HFS alkali metal spectrum in the microwave range or the Zeeman spectrum of potassium atoms in the radio frequency range.

References

1. Rabi I I *Phys. Rev.* **51** 652 (1937)
2. Bloch F *Phys. Rev.* **70** 460 (1946)
3. Packard M E, Varian R H *Phys. Rev.* **93** 941 (1954)
4. Overhauser A W *Phys. Rev.* **89** 689 (1953)
5. Overhauser A W *Phys. Rev.* **92** 411 (1953)
6. Carver T R, Slichter C P *Phys. Rev.* **92** 212 (1953)
7. Bitter F *Phys. Rev.* **76** 833 (1949)
8. Kastler A *J. Phys. Radium* **11** 255 (1950)
9. Kastler A *J. Opt. Soc. Am.* **47** 460 (1957)
10. Aleksandrov E B *Opt.-Mekh. Promyshl.* **55** (12) 27 (1988) [*Sov. J. Opt. Technol.* **55** 731 (1988)]
11. Alexandrov E B, Bonch-Bruevich V A *Opt. Eng.* **31** 711 (1992)
12. Alexandrov E B et al. *Laser Phys.* **6** 244 (1996)
13. Alexandrov E B *Phys. Scr.* **T105** 27 (2003)
14. Budker D, Romalis M *Nature Phys.* **3** 227 (2007)
15. Jaklevic R C et al. *Phys. Rev. Lett.* **12** 159 (1964)
16. Happer W *Rev. Mod. Phys.* **44** 169 (1972)
17. Bloch F *Phys. Rev.* **70** 460 (1946)
18. Göppert-Mayer M *Ann. Phys.* **401** 273 (1931) [1]

[1] The volume number is given according to the new numbering accepted in Wiley InterScience site. The print number is 9.

19. Brossel J, Cagnac B, Kastler A *C.R. Acad. Sci. Paris* **237** 984 (1953)
20. Alzetta G et al. *Nuovo Cimento B* **36** 5 (1976)
21. Swain S *J. Phys. B At. Mol. Phys.* **15** 3405 (1982)
22. Harris S E *Phys. Today* **50** (7) 36 (1997)
23. Vershovskii A K, Pazgalev A S *Zh. Tekh. Fiz.* **78** (5) 116 (2008) [*Tech. Phys.* **53** 646 (2008)]
24. Bloom A L *Appl. Opt.* **1** (1) 61 (1962)
25. Hardwick C D *Geopysics* **49** 2024 (1984)
26. Yabuzaki T, Ogawa T *J. Appl. Phys.* **45** 1342 (1974)
27. Bison G, Wynands R, Weis A *Appl. Phys. B* **76** 325 (2003)
28. Moreau O et al. *J. Physique III* **7** 99 (1997)
29. Aleksandrov E B et al. *Usp. Fiz. Nauk* **141** 551 (1983) [*Sov. Phys. Usp.* **26** 1015 (1983)]
30. Colegrove F D, Franken P A *Phys. Rev.* **119** 680 (1960)
31. Keyser A R, Rice J A, Schearer L D *J. Geophys. Res.* **66** 4163 (1961)
32. Chéron B et al. *Opt. Commun.* **115** 71 (1995)
33. Chéron B, Gilles H, Hamel J *Eur. Phys. J. Appl. Phys.* **13** 143 (2001)
34. Gilles H, Hamel J, Chéron B *Rev. Sci. Instrum.* **72** 2253 (2001)
35. Keiser G M, Robinson H G, Johnson C E *Phys. Lett. A* **51** 5 (1975)
36. Mosnier J *Ann. Geophys.* **113** 22 (1966)
37. Aleksandrov E B et al. *Opt. Spektrosk.* **58** 953 (1985) [*Opt. Spectrosc.* **58** 439 (1985)]
38. Aleksandrov E B, Balabas M V, Bonch-Bruevich V A *Pis'ma Zh. Tekh. Fiz.* **12** 749 (1987) [*Sov. Tech. Phys. Lett.* **12** 312 (1987)]
39. Aleksandrov E B, Mamyrin A B, Sokolov A P *Opt. Spektrosk.* **34** 1216 (1973)
40. Aleksandrov E B et al. *Opt. Spektrosk.* **38** 818 (1975) [*Opt. Spectrosc.* **38** 466 (1975)]
41. Aleksandrov E B, Mamyrin A B, Yakobson N N *Zh. Tekh. Fiz.* **51** 607 (1981) [*Sov. Tech. Phys.* **26** 363 (1981)]
42. Aleksandrov E B, Vershovskii A K, Pazgalev A S *Zh. Tekh. Fiz.* **76** (7) 103 (2006) [*Tech. Phys.* **51** 919 (2006)]
43. Allen A H, Bender P L *J. Geomagn. Geoelectr.* **24** 1 105 (1972)
44. Pulz E, Jäckel K-H, Linthe H-J *Meas. Sci. Technol.* **10** 1025 (1999)
45. Aleksandrov E B et al. *Zh. Tekh. Fiz.* **70** (7) 118 (2000) [*Tech. Phys.* **45** 931 (2000)]
46. Aleksandrov E B et al. *Zh. Tekh. Fiz.* **69** (9) 27 (1999) [*Tech. Phys.* **44** 1025 (1999)]
47. Aleksandrov E B, Pazgalev A S *Opt. Spektrosk.* **80** 534 (1996) [*Opt. Spectrosc.* **80** 473 (1996)]
48. Aleksandrov E B, Pazgalev A S, Rasson J L *Opt. Spektrosk.* **82** 14 (1997) [*Opt. Spectrosc.* **82** 10 (1997)]
49. Happer W, Tang H *Phys. Rev. Lett.* **31** 273 (1973)
50. Happer W, Tam A C *Phys. Rev. A* **16** 1877 (1977)
51. Allred J C et al. *Phys. Rev. Lett.* **89** 130801 (2002)
52. Kominis I K et al. *Nature* **422** 596 (2003)
53. Savukov I M, Romalis M V *Phys. Rev. A* **71** 023405 (2005)
54. Savukov I M et al. *Phys. Rev. Lett.* **95** 063004 (2005)
55. Vershovskii A K, Pazgalev A S, Aleksandrov E B *Zh. Tekh. Fiz.* **70** (1) 88 (2000) [*Tech. Phys.* **45** 88 (2000)]
56. Nagel A et al. *Europhys. Lett.* **44** 31 (1998)
57. Stähler M et al. *Europhys. Lett.* **54** 323 (2001)
58. Kitching J et al. *IEEE Trans. Instrum. Meas.* **49** 1313 (2000)
59. Schwindt P D D, Hollberg L, Kitching J *Rev. Sci. Instrum.* **76** 126103 (2005)
60. Taichenachev A V et al. *Pis'ma Zh. Eksp. Teor. Fiz.* **80** 265 (2004) [*JETP Lett.* **80** 236 (2004)]
61. Budker D, Yashchuk V, Zolotorev M *Phys. Rev. Lett.* **81** 5788 (1998)
62. Pustelny S et al. *Phys. Rev. A* **73** 23817 (2006)
63. Fairweather A J, Usher M J *J. Physics E* **5** 986 (1972)
64. Lamden R J *J. Phys. E* **2** 125 (1969)
65. Alexandrov E B et al. *Meas. Sci. Technol.* **15** 918 (2004)
66. Vershovskii A K et al. *Zh. Tekh. Fiz.* **76** (1) 115 (2006) [*Tech. Phys.* **51** 112 (2006)]
67. Vershovskii A K *Opt. Spektrosk.* **101** (2) 341 (2006) [*Opt. Spectrosc.* **101** 309 (2006)]

PACS numbers: **94.30.–d**, 95.85.Ry, 96.50.S–
DOI: 10.3367/UFNe.0180.201005g.0519

Cosmic ray variations and space weather

L I Dorman

1. Introduction

In my report at the Scientific Session of the Russian Academy of Sciences on 25 November 2009 at the Pushkov Institute of Terrestrial Magnetism, Ionosphere, and Radio Wave Propagation (IZMIRAN), the following issues were considered:

1. *Short history of cosmic ray* (*CR*) *variation investigations at the Research Institute of Terrestrial Magnetism* (*IZMIR*) *and at IZMIRAN*: the role of N V Pushkov; E S Glokova's counter telescope; the government project of S N Vernov, N V Pushkov, and Yu G Shafer (1950–1951) on the development and production of a series of big ionization chambers, and involvement of students who graduated with nuclear specialities (but without the permission from the KGB to work at nuclear sites) into the organization of the first Soviet network of CR stations; development of the theory of CR meteorological effects and the method of coupling functions; the publication in 1957 of the world's first monograph on CR variations in Moscow and its English translation in the USA; the mistake made ten times by government officials regarding financing the new government project in 1960–1961 and the great development of the experimental basis for CR variations and all other areas of solar–terrestrial physics in the USSR; and the importance of the CR variation research for fundamental science and practical applications.

2. *CR variations as an element of space weather*: the influence of Earth's atmosphere on CR and the reverse influence of CR variations on processes in Earth's atmosphere and on global climate change; radiation hazards from galactic CRs, from solar CRs, and from energetic particles precipitated from radiation belts.

3. *CR variations as a tool for space weather monitoring and forecasting*: forecasting the part of global climate change caused by galactic CR intensity variations; forecasting the radiation hazard for people and electronics on aircraft, satellites, and spacecraft caused by variations of the galactic CR intensity; forecasting the radiation hazard from solar CR events by using an online one-minute ground neutron monitor network and satellite data; forecasting great magnetic storm hazards by using an online one-hour CR intensity data from a ground-based worldwide network of neutron monitors and muon telescopes

Below, I consider the principles of the science of CR variations and the connection with space weather issues.

L I Dorman Israel Cosmic Ray and Space Weather Center with the Emilio Ségre Observatory, affiliated with Tel Aviv University, Technion, and the Israel Space Agency;
Pushkov Institute of Terrestrial Magnetism, Ionosphere, and Radio Wave Propagation (IZMIRAN), Russian Academy of Sciences, Troitsk, Moscow region, Russian Federation
E-mail: lid@physics.technion.ac.il; lid010529@gmail.com

Uspekhi Fizicheskikh Nauk **180** (5) 519–727 (2010)
DOI: 10.3367/UFNr.0180.201005f.0509
Translated by L I Dorman; edited by A M Semikhatov

2. Principles of the science of cosmic ray variations

The main causes of the observed space–time variations of CR density and anisotropy can have the atmospheric origin, magnetospheric origin, or extraterrestrial or space origin (solar, interplanetary, galactic, and extragalactic origin) (see the extensive review in [1–4]).

At each CR station k for some component i (e.g., the muon component at different zenith and azimuthal angles, the neutron component for the total intensity and different multiplicities, measurements on the ground, on ships, aircraft, balloons, or spacecraft), the intensity $I_{ki}(t)$ at an instant t can be represented as

$$I_{ki}(t) = \int_{R_k(t)}^{\infty} m_i(R,t)\, D(R,t)\, \mathrm{d}R\,, \tag{1}$$

where $R_k(t)$ is the magnetospheric cutoff rigidity (in the case of CR measurements outside the magnetosphere, $R_k(t) = 0$), $m_i(R,t)$ is the integral multiplicity (the total number of secondary particles of type i generated in cascade processes from one primary particle of the rigidity R; for CR measurements in space, $m_i(R,t) = 1$), and $D(R,t)$ is the differential rigidity spectrum of primary CRs (outside the magnetosphere). It follows from Eqn (1) that, in principle, three types of CR variations are possible,

$$\begin{aligned}\delta I_{ki}(t) = {} & -m_i(R_k,t)\, D(R_k,t)\, \delta R_k(t) \\ & + \int_{R_k(t)}^{\infty} \delta m_i(R,t)\, D(R,t)\, \mathrm{d}R \\ & + \int_{R_k(t)}^{\infty} m_i(R,t)\, \delta D(R,t)\, \mathrm{d}R\,,\end{aligned} \tag{2}$$

which have magnetospheric, atmospheric, and extraterrestrial origins. The observed relative variation of the CR intensity is obtained by dividing Eqn (2) by $I_{ki}(t)$:

$$\begin{aligned}\frac{\delta I_{ki}(t)}{I_{ki}(t)} = {} & -W_{ik}(R_k,t)\, \delta R_k(t) \\ & + \int_{R_k(t)}^{\infty} \frac{\delta m_i(R,t)}{m_i(R,t)}\, W_{ik}(R,t)\, \mathrm{d}R \\ & + \int_{R_k(t)}^{\infty} \frac{\delta D(R,t)}{D(R,t)}\, W_{ik}(R,t)\, \mathrm{d}R\,,\end{aligned} \tag{3}$$

where

$$W_{ik}(R,t) = \frac{m_i(R,t)\, D(R,t)}{I_{ki}(t)} \tag{4}$$

are the coupling functions, which may be calculated from a detailed analysis of CR cascade processes and absorption in the atmosphere. This was done for the coupling (or response) functions $W_{ik}(R,t)$ and integral multiplicities (or yield functions) $m_i(R,t)$ in [5–7] (see the extended review in Chapter 3 of [2]).

It follows from Eqn (1) that the coupling functions are normalized:

$$\int_{R_k(t)}^{\infty} W_{ik}(R,t)\, \mathrm{d}R = 1\,. \tag{5}$$

It also follows from Eqn (1) that these very important functions may be assessed experimentally by using Earth as a giant magnetic spectrometer (using exact measurements of geomagnetic effects):

$$\begin{aligned} W_{ik}(R,t) &= -\left.\frac{\partial I_{ki}(t)/\partial R_k}{I_{ki}(t)}\right|_{R_k \to R}\,, \\ m_i(R,t) &= -\left.\frac{\partial I_{ki}(t)/\partial R_k}{D(R,t)}\right|_{R_k \to R}\,. \end{aligned} \tag{6}$$

This can be done according to Eqn (6) in the vertical direction up to rigidities ≈ 17 GV and for inclined directions up to ≈ 69 GV (see [8–10] and the extended review in [4]).

According to [11], the coupling function for any secondary component can be approximated by a special function (called the Dorman function in the scientific literature)

$$W_{ik}(R,t) = \begin{cases} 0, & R < R_k, \\ \alpha_i \beta_i R^{-(\beta_i+1)} (1 - \alpha_i R_k^{-\beta_i})^{-1} \exp\left(-\alpha_i R^{-\beta_i}\right), & R \geqslant R_k. \end{cases} \tag{7}$$

It is easy to see that the normalization condition (5) is satisfied for any values of α_i and β_i. The parameters α_i and β_i for neutron monitors for different multiplicities m (parameters α_m and β_m with $m = 1, 2, 3, \ldots$) and the total neutron component (parameters α_n and β_n) were determined from latitude surveys [8–10] and are in good agreement with the theoretical calculations in [5–7]. The dependence of these coefficients on the average station pressure h (in atm $= 1000$ g cm^{-2}) and the solar activity level characterized by the logarithm of the CR intensity (for which we used the monthly average of Climax NM, $\ln(N_{\mathrm{Cl}})$, available starting from 1953) can be approximated by the functions

$$\begin{aligned}\alpha_{\mathrm{n}} = {} & (-2.915h^2 - 2.237h - 8.654) \ln N_{\mathrm{Cl}} \\ & + (24.584h^2 + 19.460h + 81.230)\,,\end{aligned} \tag{8}$$

$$\begin{aligned}\beta_{\mathrm{n}} = {} & (0.180h^2 - 0.849h + 0.750) \ln N_{\mathrm{Cl}} \\ & + (-1.440h^2 + 6.403h - 3.698)\,,\end{aligned} \tag{9}$$

$$\begin{aligned}\alpha_m = {} & \left[(-2.915h^2 - 2.237h - 8.638) \ln N_{\mathrm{Cl}}\right. \\ & \left. + (24.584h^2 + 19.46h + 81.23)\right] \\ & \times \frac{0.987m^2 + 0.225m + 6.913}{9.781}\,,\end{aligned} \tag{10}$$

$$\begin{aligned}\beta_m = {} & \left[(0.180h^2 - 0.849h + 0.750) \ln N_{\mathrm{Cl}}\right. \\ & \left. + (-1.440h^2 + 6.403h - 3.698)\right] \frac{0.081m + 1.819}{1.940}\,,\end{aligned} \tag{11}$$

where $m = 1, 2, 3, \ldots$. Instead of Climax NM, monthly averages of any other CR observatory can also be used with an appropriate recalculation of the parameters determined by the correlation between monthly data N_{Cl} of Climax NM and a given observatory for several years. For example, the recalculated parameters for the Emilio Segrè Observatory in Israel on Mt. Hermon (ESOI, neutron monitor 6NM-64) are determined by the same Eqns (8)–(11) by using the relation

$$\ln N_{\mathrm{Cl}} = 2.161 \ln N_{\mathrm{ESOI}} - 9.665\,. \tag{12}$$

For Rome 17NM-64, the following relation must be used in Eqns (8) – (11):

$$\ln N_{\mathrm{Cl}} = 1.767 \ln N_{\mathrm{Rome}} - 3.57 . \qquad (13)$$

According to [12, 13], for the coupling functions for some other different CR secondary components, the parameters α_i and β_i in Eqn (7) are as follows: 1) for the neutron component at $h_{\mathrm{o}} = 312$ mb, $\alpha_n = 8.30$ and $\beta_n = 1.45$; 2) for the neutron component at $h_{\mathrm{o}} = 680$ mb, $\alpha_{\mathrm{n}} = 13.62$ and $\beta_{\mathrm{n}} = 1.26$; 3) for the muon component at sea level $h_{\mathrm{o}} = 1030$ mb, $\alpha_\mu = 35.3$ and $\beta_\mu = 0.95$; and 4) for the muon component underground at a depth of 7 m w.e., $\alpha_\mu = 58.5$ and $\beta_\mu = 0.94$.

Above, we considered the direct problem, which answers the question of how changes in the magnetosphere, the atmosphere, and space (outside the magnetosphere) are reflected in CR observation data. But is it possible to solve inverse problem? And if yes, how can it be solved, i.e., how can data on CR variations be used to determine changes in conditions in the magnetosphere, in the atmosphere, and in space? These changes are respectively determined by $\delta R_k(t)$, $\delta m_i(R,t)/m_i(R,t)$, and $\delta D(R,t)/D(R,t) = a(t)\, R^{-b(t)}$, where $a(t)$ and $b(t)$ are functions that can be determined by comparison with observation data of CR variations. With this aim, in the case where it is possible to correct CR variation data on meteorological effects ahead of time (i.e., to determine the term in Eqn (3) with $\delta m_i(R,t)/m_i(R,t)$ by using meteorological data and the theory of CR meteorological effects [14]), a special spectrographic method was developed (when observational data is available, a minimum of three CR secondary components with different coupling functions) that allows solving the system of equations like Eqn (3) for the functions $\delta R_k(t)$, $a(t)$, and $b(t)$ at each instant of time.

In some cases, it is not possible to correct the introduction of CR variation data on meteorological effects, especially in periods of high winds (when the barometer readings jump due to the Bernoulli effect), large snowfalls, and/or when data on vertical air temperature probing are absent. In these cases, the number of unknown values significantly increases, and it is necessary to add the change in air pressure δh_{o}, the depth of snow δS (in g cm^{-2}), and changes in the air temperature distribution $\delta T(h,t)$, air humidity distribution $\delta e(h,t)$, and atmospheric electric field distribution $\delta E(h,t)$. To solve the inverse problem in these cases, the general spectrographic method was developed, using a system of a large number of equations of the same type as Eqn (3) describing CR intensity variations of many different secondary components (see the detailed description in Chapter 3 in [2]). The real-time data of the worldwide network of neutron monitors and muon telescopes now give the possibility, through spherical analysis or the so-called global spectrographic method (see the detailed description in [13] and in Chapter 3 in [2]) with the help of meteorological data and coupling functions, of determining the CR distribution function for any instant of time outside Earth's magnetosphere.

3. Cosmic rays and Earth's atmosphere

This issue has two aspects. The first is how Earth's atmosphere influenced the CRs of galactic and solar origin:

1. CR cascade processes in the atmosphere (which determine the coupling functions and integral multiplicities); see [5 – 7] and the review in Chapter 3 of [2];

2. Meteorological effects (atmospheric electric field [14], barometer, wind, snow, temperature, humidity, and gravity); see a review in [1, 15] and Chapters 5 – 9 of [2].

The second aspect is how CRs of galactic and solar origin influence Earth's atmosphere:

1. Through nuclear reactions of primary and secondary CRs with air and aerosol matter accompanied by the formation of many unstable and stable cosmogenic nuclides, especially ^{14}C (radiocarbon) and ^{10}Be (see [16 – 24] and the extended review in Chapters 10 and 17 in [2]);

2. Through the generation of secondary relativistic electrons by CRs in the atmosphere and EASs (extensive atmospheric showers) playing a crucial role in atmospheric electric field phenomena: thunderstorms, discharges, Earth's electric charge balance (see [25 – 32] and the extended review in Chapter 11 in [2]);

3. Through air ionization influences on the low ionosphere and radio wave propagation, as well as on the formation of clouds and through their influence on long-term global climate change and wheat production (see the extended review in [33, 34] and in Chapters 12 and 14 in [2]). We emphasize that because it is now known how to forecast the galactic CR intensity several years (up to 11 years) ahead, it has become possible to forecast the expected part of climate change caused by long-term CR variations [35 – 39];

4. Through chemical reactions induced by interactions of galactic and solar CRs with air atoms, including the production of nitrates and the effect on the ozone layer (see the extended review in Chapter 13 in [2]).

4. CR variations and Earth's magnetosphere

In Earth's magnetosphere, we now have many satellites that play a very important role in our modern life: TV, communications, navigation, and many others. Especially important is GPS (Global Positioning System, including car navigation systems), which works through a worldwide network of satellites. Satellites usually spend several years in space, and are therefore exposed to the short- and long-term effects of solar and galactic CRs and many other factors of space weather. Certainly, all satellites are insured and because of anomalies (especially large anomalies that can lead to the full destruction of satellite work), insurance companies pay many hundreds of millions of dollars per year. There is a body of evidence on the existence of spacecraft anomalies caused by the space environment. A comparative analysis of the distribution of each of these parameters relative to the satellite malfunction was carried out for the total number of malfunctions (about 6000 events), and separately for high-altitude ($\sim$ 5000 events) and low-altitude (about 800 events) orbit satellites. No relation has been found between low and high-altitude satellite malfunctions. The majority of malfunctions of Kosmos satellites occurred at the same time as failures on other low-altitude orbit spacecraft, and they seemed to be related to space weather parameters. About 50% of the total number of anomalies was identified as unrelated to human or technological factors. It was supposed that the data free from these technological malfunctions might be related to space weather and were taken for correlation analysis. Is it possible to reliably predict those periods when satellite anomalies are expected, and what must be done to avoid satellite anomalies? To investigate this problem, an international team of researches from Italy, Russia, Kazakhstan, Ukraine, and Israel analyzed a large

collection of known satellite anomalies (about 6000), depending on satellite orbits (altitude and inclination to the equatorial plane) and different space weather conditions. The following parameters were used for correlation analysis ([39–48], see the short review in Section 18.17 in [2]):

1) solar and galactic cosmic ray intensities, determined by neutron monitor data;

2) proton (>10 MeV and >60 MeV) and electron (>2 MeV) fluxes according to measurements on satellites;

3) parameters of solar activity (sunspot number, solar radiation at 2800 MHz (10.7 cm), index F10.7);

4) parameters of geomagnetic activity (Ap, AE, and Dst indices).

As an example, we show in Figs 1 and 2 how the frequency of anomalies in different orbits increases as the flux of energetic protons increases. If there is a high probability of an anomaly destroying the normal work of a satellite, experts must decide what to do: for example, when high ionization is expected (at very large fluxes of energetic protons; see Figs 1 and 2), electric power may for a short time be switched off to especially important parts of electronics to exclude discharges along the treks of energetic particles.

Earth's magnetosphere shapes the trajectories of primary CRs, acceptance cones, and cutoff rigidities (see the extensive review in Chapter 4 in [4]). Changes in Earth's magnetosphere are caused by long-term variations of the main geomagnetic field and by electric currents in the magnetosphere and ionosphere. It is important that the planetary distribution of $(\delta R_k)_{\rm obs}$ at any instant of time (especially during magnetic storms) can be determined by the above spectrographic method (see Section 1) by observations of the CR intensity via a worldwide network of stations. This information, together with data on geomagnetic field variations, can be used for determining how the parameters of ring current (main cause of Dst variation) and magnetopause currents change with time. This was done in [49–68] (see the extended review in Chapter 6 of [4]). On the other hand, the trajectory can be calculated for the same time instants in the framework of any theoretical model of the magnetosphere (including the main geomagnetic field): $(\delta R_k)_{\rm theor}$. By comparing $(\delta R_k)_{\rm obs}$ with $(\delta R_k)_{\rm theor}$, it can be estimated what model is more suited to the reality. This can be done with galactic and solar CRs ([69–89]; see the extended review in Chapter 7 of [4]).

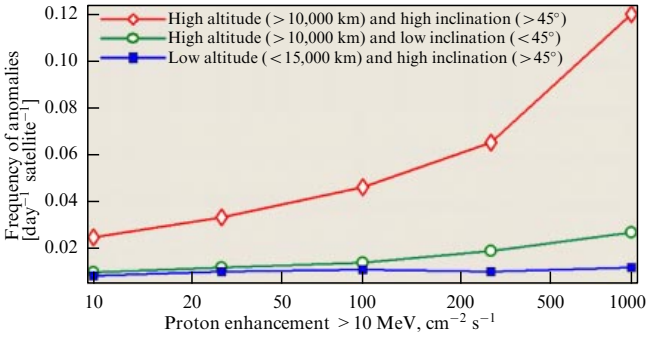

Figure 1. Mean satellite anomaly frequencies in the first two days of proton enhancements > 10 MeV depending on the maximum flux.

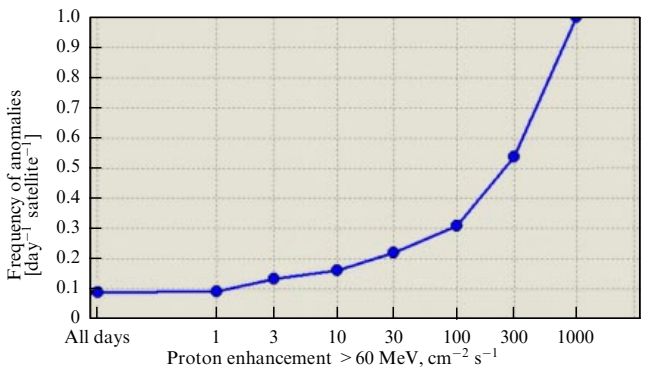

Figure 2. Frequency of satellite anomaly (high-altitude high-inclination group) depending on the maximum proton flux >60 MeV.

5. CR variations and radiation hazards from solar-flare energetic particles

It is well known that solar energetic particle (SEP) events are very anisotropic at the beginning stage, especially during great events as in February 1956, July 1959, August 1972, September–October 1989, July 2000, January 2005, and many others [1, 90–95]. In these cases, determining the properties of primary solar CRs outside the magnetosphere on the basis of experimental data (by the above spectrographic method and coupling functions) and then determining the source function of solar CRs and the parameters of propagation in interplanetary space based on experimental data, i.e., solving the inverse problem, is very difficult both theoretically (in the framework of the kinetic Boltzmann equation or in the framework of the Fokker–Planck equation of anisotropic diffusion; see possible ways of approximately solving this problem in Chapter 2 of [3]) and experimentally, because it is necessary to organize an International Service of CR Variations (similar to the International Meteorological Service) on the basis of the existing worldwide CR stations and some satellites with data collection on a real-time scale through the Internet. An important step was taken in this direction in 2008–2009, when the Neutron Monitor Data Base (NMDB) was founded; it now operates continuously. The extended European part of this international service includes not only West European countries but also Russia, Kazakhstan, Armenia, and Israel.

By the procedure developed in [96–100] for each CR station, the starting moment of a solar CR event can be determined automatically, and then the energy spectrum of solar CR outside the atmosphere can be determined above the individual CR station for different instants of time by the spectrographic method and coupling functions. As result, the planetary distribution of solar CR intensity outside the atmosphere can be obtained, and then, by taking the influence of the geomagnetic field on particle trajectories into account, the solar CR angle distribution outside Earth's magnetosphere can be determined. On the basis of this great experimental material, the inverse problem can be solved automatically in the near future in the framework of the Fokker–Planck equation of anisotropic diffusion and/or in the framework of the kinetic Boltzmann equation [101].

However, we must recall that after one or two scatterings in interplanetary space (i.e., 10–15 min after the beginning of an event), the distribution of solar CRs in interplanetary space becomes practically isotropic, and hence the differences in time evolution of the solar CR intensity on CR stations is determined only by differences in coupling functions and cutoff rigidities. This implies that if we use data not from the very beginning of an event, we can solve the inverse problem,

as the first step, in the framework of the much simpler theory of isotropic diffusion. This allows proceeding based on two well-established facts:

(i) the time of particle acceleration on the Sun and injection into the solar wind is very short in comparison with the time of propagation to Earth, and therefore the solar CR source function can be considered a δ-function of time;

(ii) a very anisotropic distribution of solar CRs developed after a few scatterings of energetic particles becomes nearly isotropic (well-known examples of February 1956, September 1989, and many others).

Therefore, presently, before the International Service of CR Variations mentioned above (collecting one-minute data from nearly all CR stations of the worldwide network on a real-time scale) is organized, we operate on the basis of solving the inverse problem in the framework of simple isotropic diffusion of solar CRs in interplanetary space (in this case, it is enough to use the observation data of several different CR components on one station or only a few stations). We therefore consider isotropic diffusion with a point-like instantaneous source function

$$Q(R, r, t) = N_{\rm o}(R)\,\delta(r)\,\delta(t)\,, \tag{14}$$

where r is the distance to the Sun, t is the time after the solar CR ejection into interplanetary space, and $N_{\rm o}(R)$ is an unknown function to be determined from comparison with experimental data. We suppose that the diffusion coefficient depends on the rigidity R of energetic particles and on the distance r to the Sun as

$$\kappa(R, r) = \kappa_1(R)\left(\frac{r}{r_1}\right)^{\beta}, \tag{15}$$

where $\kappa_1(R)$ and $\beta(t)$ are unknown functions to be determined from comparison with experimental data, and $r_1 = 1$ a.u. is the radius of Earth's orbit. In this case, the solution of the diffusion equation is given by

$$N(R, r, t) = \frac{N_{\rm o}(R)\, r_1^{3\beta/(2-\beta)} \big(\kappa_1(R)\, t\big)^{-3/(2-\beta)}}{(2-\beta)^{(4+\beta)/(2-\beta)}\,\Gamma\big(3/(2-\beta)\big)} \times \exp\left(-\frac{r_1^{\beta} r^{2-\beta}}{(2-\beta)^2 \kappa_1(R)\, t}\right), \tag{16}$$

where t is the time after solar CR ejection into the solar wind.

We have four unknown parameters: the time of solar CR ejection into the solar wind $T_{\rm e}$, β, $\kappa_1(R)$, and $N_{\rm o}(R)$. We assume that according to ground and satellite measurements at the distance $r = r_1 = 1$ a.u. from the Sun, we know $N_1(R)$, $N_2(R)$, $N_3(R)$, and $N_4(R)$ at UT times T_1, T_2, T_3, and T_4. In this case, the times after ejection of solar CRs into the solar wind are

$$t_1 = T_1 - T_{\rm e} = x\,, \quad t_2 = T_2 - T_1 + x\,, \quad t_3 = T_3 - T_1 + x\,, \quad t_4 = T_4 - T_1 + x\,. \tag{17}$$

For each $N_i(R, r = r_1, T_i)$, we use Eqns (16) and (17) to obtain

$$N_i(R, r = r_1, T_i) = \frac{N_{\rm o}(R)\, r_1^{3\beta/(2-\beta)} \big(\kappa_1(R)(T_i - T_1 + x)\big)^{-3/(2-\beta)}}{(2-\beta)^{(4+\beta)/(2-\beta)}\,\Gamma\big(3/(2-\beta)\big)} \times \exp\left(-\frac{r_1^2 (2-\beta)^{-2}}{\kappa_1(R)(T_i - T_1 + x)}\right), \tag{18}$$

where $i = 1, 2, 3, 4$. To determine x, we consecutively eliminate the unknown parameters $N_{\rm o}(T)$, $\kappa_1(R)$, and β. We first eliminate $N_{\rm o}(R)$ by using four equations like (18) to write the three equations

$$\frac{N_1(R, r = r_1, T_1)}{N_i(R, r = r_1, T_i)} = \left(\frac{x}{T_i - T_1 + x}\right)^{-3/(2-\beta)} \times \exp\left[-\frac{r_1^2}{(2-\beta)^2 \kappa_1(R)}\left(\frac{1}{x} - \frac{1}{T_i - T_1 + x}\right)\right], \tag{19}$$

where $i = 2, 3, 4$. To eliminate $\kappa_1(R)$, we take the natural logarithm of both parts of Eqns (19) and then divide one equation by another; as result, we obtain the two equations

$$\frac{\ln(N_1/N_2) + \big[3/(2-\beta)\big] \ln\big[x/(T_2 - T_1 + x)\big]}{\ln(N_1/N_3) + \big[3/(2-\beta)\big] \ln\big[x/(T_3 - T_1 + x)\big]} = \frac{1/x - 1/(T_2 - T_1 + x)}{1/x - 1/(T_3 - T_1 + x)}\,, \tag{20}$$

$$\frac{\ln(N_1/N_2) + \big[3/(2-\beta)\big] \ln\big[x/(T_2 - T_1 + x)\big]}{\ln(N_1/N_4) + \big[3/(2-\beta)\big] \ln\big[x/(T_4 - T_1 + x)\big]} = \frac{1/x - 1/(T_2 - T_1 + x)}{1/x - 1/(T_4 - T_1 + x)}\,. \tag{21}$$

After eliminating the unknown parameter β from Eqns (20) and Eqn (21), we obtain an equation for x:

$$x^2(a_1 a_2 - a_3 a_4) + xd(a_1 b_2 + b_1 a_2 - a_3 b_4 - b_3 a_4) + d^2(b_1 b_2 - b_3 b_4) = 0\,, \tag{22}$$

where

$$d = (T_2 - T_1)(T_3 - T_1)(T_4 - T_1)\,, \tag{23}$$

$$a_1 = (T_2 - T_1)(T_4 - T_1) \ln\frac{N_1}{N_3} - (T_3 - T_1)(T_4 - T_1) \ln\frac{N_1}{N_2}\,, \tag{24}$$

$$a_2 = (T_3 - T_1)(T_4 - T_1) \ln\frac{x}{T_2 - T_1 + x} - (T_2 - T_1)(T_3 - T_1) \ln\frac{x}{T_4 - T_1 + x}\,, \tag{25}$$

$$a_3 = (T_2 - T_1)(T_3 - T_1) \ln\frac{N_1}{N_4} - (T_3 - T_1)(T_4 - T_1) \ln\frac{N_1}{N_2}\,, \tag{26}$$

$$a_4 = (T_3 - T_1)(T_4 - T_1) \ln\frac{x}{T_2 - T_1 + x} - (T_2 - T_1)(T_4 - T_1) \ln\frac{x}{T_3 - T_1 + x}\,, \tag{27}$$

$$b_1 = \ln\frac{N_1}{N_3} - \ln\frac{N_1}{N_2}\,, \quad b_2 = \ln\frac{x}{T_2 - T_1 + x} - \ln\frac{x}{T_4 - T_1 + x}\,, \tag{28}$$

$$b_3 = \ln\frac{N_1}{N_4} - \ln\frac{N_1}{N_2}\,,$$
$$b_4 = \ln\frac{x}{T_2 - T_1 + x} - \ln\frac{x}{T_3 - T_1 + x}\,. \qquad (29)$$

As can be seen from Eqns (25) and (27)–(29), the coefficients a_2, a_4, b_2, and b_4 very weakly (logarithmically) depend on x. Therefore, we solve Eqn (22) by the iteration method: as a first approximation, we use $x_1 = T_1 - T_e \approx 500$ (which is the minimum time propagation of relativistic particles from the Sun to Earth's orbit without scattering). Then, from Eqns (25) and (27)–(29), we determine $a_2(x_1)$, $a_4(x_1)$, $b_2(x_1)$, and $b_4(x_1)$, and from Eqn (22), we determine the second approximation x_2, and so on. After determining x, i.e., using Eqn (17), we determine t_1, t_2, t_3, t_4, the final solutions for β, $\kappa_1(R)$, and $N_o(R)$. We determine the unknown parameter β from Eqns (20) and (21):

$$\beta = 2 - 3\left[\ln\frac{t_2}{t_1} - \frac{t_3(t_2 - t_1)}{t_2(t_3 - t_1)}\ln\frac{t_3}{t_1}\right] \times \left[\ln\frac{N_1}{N_2} - \frac{t_3(t_2 - t_1)}{t_2(t_3 - t_1)}\ln\frac{N_1}{N_3}\right]^{-1}. \qquad (30)$$

Then we determine unknown parameter $\kappa_1(R)$ from Eqn (19):

$$\kappa_1(R) = \frac{r_1^2(t_1^{-1} - t_2^{-1})}{3(2-\beta)\,\ln(t_2/t_1) - (2-\beta)^2\ln(N_1/N_2)} = \frac{r_1^2(t_1^{-1} - t_3^{-1})}{3(2-\beta)\,\ln(t_3/t_1) - (2-\beta)^2\ln(N_1/N_3)}\,. \qquad (31)$$

After determining the parameters β and $\kappa_1(R)$ we can determine the last parameter $N_o(R)$ from Eqn (18):

$$N_o(R) = N_i(2-\beta)^{(4+\beta)/(2-\beta)}\Gamma\left(\frac{3}{2-\beta}\right) r_1^{-3\beta/(2-\beta)} \times \left(\kappa_1(R)\,t_i\right)^{3/(2-\beta)} \exp\left(\frac{r_1^2}{(2-\beta)^2 k_1(R)\,t_i}\right), \qquad (32)$$

where $i = 1, 2, 3$.

Thus, by finding x, we find the time of ejection $T_e = T_1 - x$ and then the transfer time T of observation data from the UT after ejection $t = T - T_e$. By substituting the obtained β, $\kappa_1(R)$, and $N_o(R)$ in Eqn (16), it is easy to predict how the intensity of solar CRs changes with time at any distance from the Sun in interplanetary space or in Earth's atmosphere at any depth and any cutoff rigidity (by using Eqn (3) and the method of coupling functions).

We used the results described above in the method of great radiation hazard prediction based on online CR one-minute ground and satellite data [98, 99]. To test the method and estimate how many minutes of observation after the beginning of a solar CR event we need to predict all events with sufficient accuracy, we used one-minute data obtained during the very anisotropic solar CR event in September 1989 by a neutron monitor on the top of Gran Sasso in Italy, and one-minute satellite data on protons with the energy $\geqslant 0.1$ GeV. It is important that this neutron monitor detected one-minute data not only of the total neutron intensity but also of neutron multiplicities ($\geqslant 1$, $\geqslant 2$, $\geqslant 3$, up to $\geqslant 8$) with different coupling functions [see Eqns (7)–(11)]. Taking satellite data into account and using the spectrographic method and coupling functions, this allowed minute-by-minute determining the energy spectrum of solar CRs outside Earth's magnetosphere, i.e., the functions $N_i(R, r = r_1, T_i)$ solving the system of equations (18). Then, on the basis of the inverse problem solution described above, we determined the unknown ejection time $t_1 = T_1 - T_e = x$ from Eqn (22), the parameters β from Eqn (30), $\kappa_1(R)$ Eqn (31), and $N_o(R)$ from Eqn (32). With the obtained values of these parameters, we then used Eqn (16) and the coupling functions to determine the expected CR intensity variations in the neutron monitor and GOES (geostationary operational environmental satellite), and to compare them with real observations. The results of the comparison (see Fig. 3) show that for high-energy particles (more than several GeV, measured by a neutron monitor) about 15–20 min was needed for approximate forecasting, and about 35 min was needed for exact forecasting of all events. For forecasting in a small energy region (about 100 MeV), we need to use data for about 30–40 min to give the exact forecast for about two days. Then, from Eqn (16)

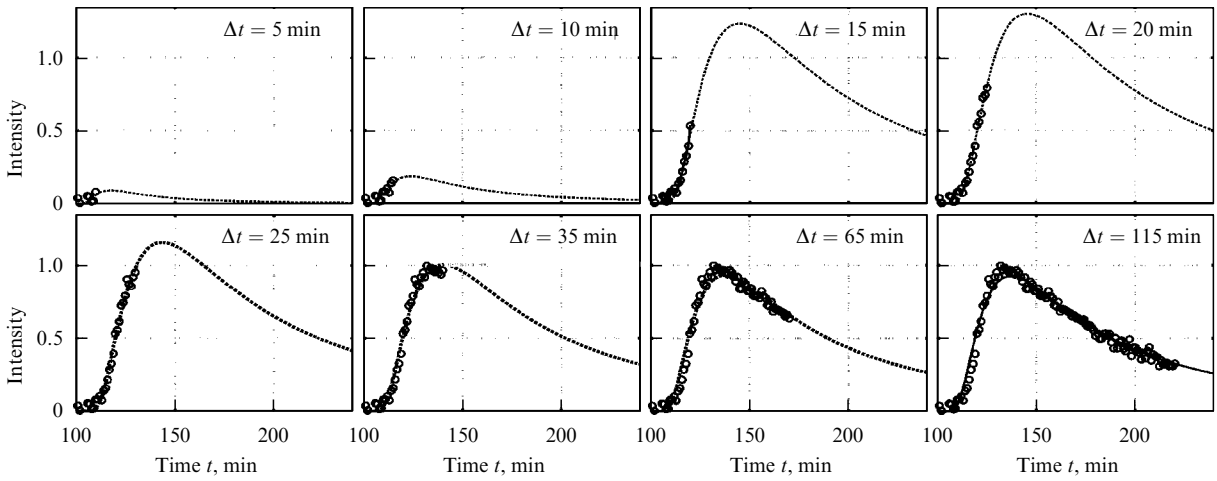

Figure 3. Results of calculating the x, β, $\kappa_1(R)$, and $N_o(R)$ parameters based on the first 5, 10, 15, ... minutes of observation with a neutron monitor ($\Delta t = 5$ min, $\Delta t = 10$ min, $\Delta t = 15$ min, ...) and using Eqn (16) to estimate the expected time dependence of the solar CR intensity, followed by a recalculation with the help of a coupling function in terms of the projected variation in the count rate in a neutron monitor. The unit along the vertical axis is the observed maximum of the increase in the solar CR flux intensity based on the neutron monitor date at Gran Sasso. The horizontal line is the time (in minutes) from10.00 UT, 29 September 1989.

and the coupling functions, we can also estimate the total expected radiation hazard during all events for spacecraft at different distances from the Sun, for satellites in the magnetosphere at different orbits, for aircraft at different altitudes, and for different objects in the atmosphere and on the ground.

6. Conclusion

The science of CR variations, which lies between nuclear physics, astrophysics, the physics of the Sun, heliosphere, and magnetosphere, geophysics, and meteorology, has long had mainly a fundamental character without any important practical applications. Only in the last 15 – 20 years, in connection with the impressive development of space research, the broad use of satellites, the founding of GPS, the extension of airlines to altitudes about 10 km, and especially the great jump in developing microelectronics (very sensitive to cosmic radiation), has the practical application of CR variations, especially for space weather monitoring and forecasting, started developing intensively. This application is promoted by the world-wide network of CR stations founded in the last 50 – 60 years and equipped with neutron monitors and muon telescopes (in the energy range of more than a few GeV) and a series of satellites launched in the last 30 years that has continuously measured CR intensity variations in much smaller energy intervals and made their one-minute data available through the Internet. The methods described above have important prospects for development using the anisotropic part, at the very beginning of a solar CR event [101]. With the founding of the International CR Variation Service in the near future (as mentioned above, the first step in this direction was made in 2008 – 2009 and with the founding of NMDB, the extended European part of this service), it will become possible to forecast the expected radiation dose for about two days, not 20 – 40 min after the beginning of a solar CR event (as was described above) but sufficiently earlier, about 5 – 15 min after the beginning of an event, as described in [101] (which can have great practical significance). Moreover, the founding of a well-functioning International CR Variation Service will allow continuously determining the change in time of the angle–energy CR distribution outside Earth's magnetosphere by one-hour CR data from the world-wide network of neutron monitors and muon telescopes (by the global spectrographic method: see Chapter 3 in [2]). This important information allows forecasting the approach of powerful interplanetary shock waves and coronal mass ejections (CMEs) for 15 – 20 hours to Earth; by interaction with Earth's magnetosphere, CMEs cause big magnetic storms that are dangerous for human health (with the frequency of myocardial infarcts, brain strokes, and auto accidents increasing) and cause some part of the anomalies (malfunctions) in the work of satellites [42 – 48] and large induction currents at high latitudes that disturb the work of electrical high-voltage power networks and large-scale pipelines [42, 102]. Unfortunately, in this short paper, we were not able to describe this important issue in more detail, but we plan in the near future to devote a special paper to this important aspect of the CR variation research.

References

1. Dorman L I *Variatsii Kosmicheskikh Luchei* (Cosmic Ray Variations) (Moscow: Gostekhteorizdat, 1957) [Translated into English (Washington, DC: US Department of Defence, Ohio Air-Force Base, 1957)]
2. Dorman L I *Cosmic Rays in the Earth's Atmosphere and Underground* (Dordrecht: Kluwer Acad. Publ., 2004)
3. Dorman L I *Cosmic Ray Interactions, Propagation, and Acceleration in Space Plasmas* (Dordrecht: Springer, 2006)
4. Dorman L I *Cosmic Rays in Magnetospheres of the Earth and other Planets* (Dordrecht: Springer, 2009)
5. Dorman L I, Yanke V G, in *Proc. of the 17th Intern. Cosmic Ray Conf., Paris, France* Vol. 4 (1981) p. 326
6. Dorman L I, Yanke V G, V K Korotkov V K, in *Proc. 17th of the Intern. Cosmic Ray Conf., Paris, France* Vol. 4 (1981) p. 330
7. Clem J M, Dorman L I *Space Sci. Rev.* **93** 335 (2000)
8. Aleksanyan T M, Dorman L I, Yanke V G, Korotkov V K, in *Proc. of the 19th Intern. Cosmic Ray Conf., La Jolla, USA* Vol. 5 (1985) p. 300
9. Moraal H et al. *J. Geophys. Res.* **94** (A2) 1459 (1989)
10. Dorman L I et al. *J. Geophys. Res.* **105** (A9), 21047 (2000)
11. Dorman L I, in *Proc. of the 11th Intern. Cosmic Ray Conf., Budapest, Invited Papers and Rapporteur Talks* (1969) p. 381
12. Dorman L I, Gushchina R T, Smart D F, Shea M A *Effective Cut-Off Rigidities of Cosmic Rays* (Moscow: Nauka, 1972)
13. Dorman L I *Cosmic Rays*: *Variations and Space Explorations* (Amsterdam: North-Holland, 1974)
14. Dorman L I *Meteorological Effects of Cosmic Rays* (Moscow: Nauka, 1972)
15. Dorman L I et al. *J. Geophys. Res.* **108** (A5) 1181 (2003)
16. Dorman L I, in *Proc. of the 15th Intern. Cosmic Ray Conf., Plovdiv* Vol. 4 (Budapest: Dept of Cosmic Rays Central Research. Institute for Physics of the Hungarian Acad. of Sci., 1977) p. 374
17. Dorman L I, in *Proc. of the 15th Intern. Cosmic Ray Conf., Plovdiv* Vol. 4 (Budapest: Dept of Cosmic Rays Central Research. Institute for Physics of the Hungarian Acad. of Sci., 1977) p. 378
18. Dorman L I, in *Proc. of the 15th Intern. Cosmic Ray Conf., Plovdiv* Vol. 4 (Budapest: Dept of Cosmic Rays Central Research. Institute for Physics of the Hungarian Acad. of Sci., 1977) p. 383
19. Dorman L I, in *Proc. of the 15th Intern. Cosmic Ray Conf., Plovdiv* Vol. 4 (Budapest: Dept of Cosmic Rays Central Research. Institute for Physics of the Hungarian Acad. of Sci., 1977) p. 387
20. Dorman L I, in *Proc. of the 15th Intern. Cosmic Ray Conf., Plovdiv* Vol. 4 (Budapest: Dept of Cosmic Rays Central Research. Institute for Physics of the Hungarian Acad. of Sci., 1977) p. 395
21. Dorman L I, in *Proc. of the 15th Intern. Cosmic Ray Conf., Plovdiv* Vol. 4 (Budapest: Dept of Cosmic Rays Central Research. Institute for Physics of the Hungarian Acad. of Sci., 1977) p. 400
22. Dorman L I "Peculiarities of cosmic ray research by radio-carbon method", *Proc. 6th All-Union Meeting on the Problem* "Astrophysics Phenomena and Radio-Carbon" (Tbilisi, 1976), Tbilisi, METSNIEREBA, 49-96 (1978).
23. Dorman L I, in *Towards the Millennium in Astrophysics*: *Problems and Prospects. Intern. School of Cosmic Ray Astrophysics 10th Course, Erice, Italy, 1996* (Eds M M Shapiro, R Silberberg, J P Wefel) (Singapore: World Scientific, 1998) p. 303
24. Dorman L I, in *Towards the Millennium in Astrophysics*: *Problems and Prospects. Intern. School of Cosmic Ray Astrophysics 10th Course, Erice, Italy, 1996* (Eds M M Shapiro, R Silberberg, J P Wefel) (Singapore: World Scientific, 998) p. 323
25. Gurevich A V, Zybin K P, Roussel-Dupré R *Phys. Lett. A* **165** 463 (1992)
26. Gurevich A V, Zybin K P, Roussel-Dupré R A *Phys. Lett. A* **254** 79 (1999)
27. Gurevich A V, Milikh G M *Phys. Lett. A* **262** 457 (1999)
28. Gurevich A V et al. *Phys. Lett. A* **282** 180 (2001)
29. Gurevich A V, Zybin K P *Usp. Fiz. Nauk* **171** 1177 (2001) [*Phys. Usp.* **47** 1119 (2001)]
30. Ermakov V I, Stozhkov Y I, in *Proc. 11th Intern. Conf. Atmospheric Electricity, Alabama, USA* (1999) p. 242
31. Ermakov V I, Stozhkov Yu I "Mechanism of thundercloud electricity production," Preprint FIAN, No. 25, pp. 28 (2002)
32. Ermakov V I, Stozhkov Y I, in *Proc. 28th Intern. Cosmic Ray Conf., Tsukuba* Vol. 7 (2003) p. 4157
33. Velinov P, G, Nestorov G, Dorman L *Cosmic Ray Influence on the Ionosphere and Radio Wave Propagation* (Sofia: Bulgarian Ac. Sci. Press, 1974)

34. Dorman L I, in *Climate Change*: *Observed Impacts on Planet Earth* (Ed. T M Letcher) (Amsterdam: Elsevier, 2009) p. 43
35. Dorman L I *Ann. Geophys.* **23** 3003 (2005)
36. Dorman L I, in *Proc. of the 18th ESA Symp. on European Rocket and Balloon Programmes and Related Research, Visby, Sweden, 3–7 June 2007* (ESA SP-647, Ed. L Conroy) (Noordwijk: ESTEC, 2007)
37. Dorman L I *Adv. Space Res.* **35** 496 (2005)
38. Belov A V et al. *Adv. Space Res.* **35** 491 (2005)
39. Dorman L I *Adv. Space Res.* **37** 1621 (2006)
40. Dorman L I, in *Proc. of the 26th Intern. Cosmic Ray Conf., Salt Lake City, Utah, USA August 17–25, 1999* Vol. 6 (Eds D Kieda, M Salamon, B Dingus) (1999) p. 382
41. Dorman L I, in *European Rocket and Balloon Programs and Related Research*: *Proc. of the 14th European Space Agency Symp., Potsdam, Germany, 31 May–3 June 1999* (ESA-SP, Vol. 437, Ed. B Schürmann) (1999) p. 207
42. Dorman L I, in *Proc. of the 22nd ISTC Japan Workshop on Space Weather Forecast in Russia/CIS* Vol. 2 (Ed. Y Muraki) (Nagoya: Nagoya Univ., 2002) p. 133
43. Belov A et al., in *Proc. of the 28th Intern. Cosmic Ray Conf., Tsukuba, Japan, July 31–August 7* Vol. 7 (Eds T Kajita et al.) (2003) p. 4213
44. Belov A et al., in *Effects of Space Weather on Technology Infrastructure* (Ed. I A Daglis) (Dordrecht: Kluwer Acad. Publ., 2004) p. 147
45. Belov A V et al. *Geomagn. Aeron.* **44** 502 (2004) [*Geomagn. Aeron.* **44** 461 (2004)]
46. Dorman L I et al. *Ann. Geophys.* **23** 3009 (2005)
47. Dorman L I et al. *Adv. Space Res.* **36** 2530 (2005)
48. Iucci N et al. *Space Weather* **3** S01001 (2005)
49. Dorman L I et al. *Izv. Akad. Nauk SSSR. Ser. Fiz.* **32** 1896 (1968)
50. Dorman L I et al., in *Issledovaniya po Geomagnetizmu, Aeronomii i Fizike Solntsa* (Research in Geomagnetism, Aeronomy and Physics of the Sun) Vol. 20 (Moscow: Nauka, 1971) p. 367
51. Dvornikov V M *Izv. Akad. Nauk SSSR. Ser. Fiz.* **36** 2427 (1972)
52. Dorman L I et al., in *Proc. of the 13th Intern. Cosmic Ray Conf., Denver, Colorado, USA* Vol. 2 (1973) p. 1032
53. Dorman L I et al., in *Proc. of the 13th Intern. Cosmic Ray Conf., Denver, Colorado, USA* Vol. 2 (1973) p. 1690
54. Dorman L I et al., in *Proc. of the 15th Intern. Cosmic Ray Conf., Plovdiv* Vol. 3 (Budapest: Dept of Cosmic Rays Central Research. Institute for Physics of the Hungarian Acad. of Sci., 1977) p. 347
55. Debrunner H et al. *Planet. Space Sci.* **27** 577 (1979)
56. Dorman L I, Krestyannikov Yu Ya, Sergeev A V, in *Proc. of the 16th Intern. Cosmic Ray Conf., Kyoto, Japan* Vol. 3 (Eds S Miyake, N G Kaigi) (Tokyo: Inst. for Cosmic Ray Res., Univ. of Tokyo, 1979) p. 535
57. Dorman L I et al., in *Trudy Mezhdunar. Seminara po Kosmofizicheskim Aspektam kosmicheskikh Luchei, Alma-Ata, 1980* (Intern. Seminar on Cosmophys. Aspects of Cosmic Ray Studies, Alma-Ata, 1980, p. 45)
58. Dorman L I, Krestyannikov Yu Ya, Sergeev A V, in *Proc. of the 17th Intern. Cosmic Ray Conf., Paris, France* Vol. 4 (1981) p. 241
59. Belov A V, Dorman L I, Yanke V G, in *Proc. of the 18th Intern. Cosmic Ray Conf., Bangalore* Vol. 10 (1983) p. 144
60. Flückiger E O, Smart D F, Shea M A *J. Geophys. Res.* **91** (A7) 7925 (1986)
61. Flückiger E O, Shea M A, Smart D F, in *Proc. of the 20th Intern. Cosmic Ray Conf., Moscow* Vol. 4 (1987) p. 216
62. Baisultanova L M, Belov A V, Dorman L I, Yanke V G, in *Proc. of the 20th Intern. Cosmic Ray Conf., Moscow* Vol. 4 (1987) p. 231
63. Dvornikov V M, Sdobnov V E, Sergeev A V, in *Proc. of the 20th Intern. Cosmic Ray Conf., Moscow* Vol. 4 (1987) p. 220
64. Flückiger E O, Smart D F, Shea M A *J. Geophys. Res.* **95** (A2) 1113 (1990)
65. Baisultanova L M, Belov A V, Yanke V G, in *Proc. of the 24th Intern. Cosmic Ray Conf., Rome, Italy, August 28–September 8* Vol. 4 (Eds N Inucci, E Lamanna) (1995) p. 1090
66. Boberg P R et al. *Geophys. Res. Lett.* **22** 1133 (1995)
67. Danilova O A, Tyasto M I, in *Proc. of the 24th Intern. Cosmic Ray Conf., Rome, Italy, August 28–September 8* Vol. 4 (Eds N Inucci, E Lamanna) Vol. 4 (1995) p. 1066
68. Bobik P, Kudela K, Usoskin I, in *Proc. of the 27th Intern. Cosmic Ray Conf., Hamburg, Germany, 7–15 August* Vol. 10 (2001) p. 4056
69. Belov A et al. *J. Geophys. Res.* **110** (A9) A09S20 (2005)
70. Desorgher L "MAGNETOCOSMICS: Geant4 application for simulating the propagation of cosmic rays through the Earth's magnetosphere," http://reat.space.qinetiq.com/septimess/magcos/ (2004)
71. Flückiger E O et al."The ground level enhancement on January 20, 2005, in the context of extreme solar cosmic ray particle events and geomagnetic super storms," *AOGS-2006* Abstract 59-ST-A1215, Singapore (2006)
72. Smart D F, Shea M A *Adv. Space Res.* **28** 1733 (2001)
73. Smart D F, Shea M A, Flückiger E O *Space Sci. Rev.* **93** 305 (2000)
74. Struminsky A, in *Proc. of the 27th Intern. Cosmic Ray Conf., Hamburg, Germany, 7–15 August, 2001* Vol. 9 (2001) p. 3558
75. Struminsky A, Manohar L, in *Proc. of the 27th Intern. Cosmic Ray Conf., Hamburg, Germany, 7–15 August, 2001* Vol. 10 (2001) p. 4052
76. Tsyganenko N A, Usmanov A V *Planet. Space Sci.* **30** 985 (1982)
77. Tsyganenko N A *Planet. Space Sci.* **35** 1347 (1987)
78. Tsyganenko N A *Planet. Space Sci.* **37** 5 (1989)
79. Stern D P, Tsyganenko N A *EOS Trans. AGU* **73** No. 46, 489, 493, 494 (1992)
80. Alexeev I I et al. *J. Geophys. Res.* **106** (A11) 25683 (2001)
81. Alexeev I I et al. *Space Sci. Rev.* **107** 7 (2003)
82. Maltsev Yu P, Ostapenko A A *Geomagn. Aeron.* **41** 761 (2001) [*Geomagn. Aeron.* **41** 726 (2001)]
83. Maltsev Y, Ostapenko A *Ann. Geophys.* **22** 2989 (2004)
84. Tsyganenko N A *J. Geophys. Res.* **107** (A8) 1179 (2002)
85. Tsyganenko N A *J. Geophys. Res.* **107** (A8) 1176 (2002)
86. Tsyganenko N A, Sitnov M I *J. Geophys. Res.* **112** (A6) A06225 (2007)
87. Tsyganenko N A, Stern D P *J. Geophys. Res.* **101** (A12) 27187 (1996)
88. Tsyganenko N A, Singer H J, Kasper J C *J. Geophys. Res.* **108** (A5) 1209 (2003)
89. Tyasto M I et al. *Adv. Space Res.* **42** 1556 (2008)
90. Dorman L I *Geophysical and Astrophysical Aspects of Cosmic Rays* (Progress in Physics of Cosmic Ray and Elementary Particles, Vol. 7, Eds J G Wilson, S A Wouthuysen) (Amsterdam: North-Holland, 1963) p. 1
91. Dorman L I *Variatsii Kosmicheskikh Luchei i Issledovanie Kosmosa* (Cosmic Ray Variations and Space Research) (Moscow: Nauka, 1963)
92. Dorman L I *Uskoritel'nye Protsessy v Kosmose* (Acceleration Processes in Space) (Moscow: VINITI, 1972)
93. Dorman L I *Kosmicheskie Luchi Solnechnogo Proiskhozhdeniya* (Cosmic Rays of Solar Origin) (Moscow: VINITI, 1978)
94. Dorman L I, Miroshnichenko L I *Solnechnye Kosmicheskie Luchi* (Solar Cosmic Raus) (Moscow: Fizmatgiz, 1968) [Translated into English (Washington, DC: NASA, 1976)]
95. Miroshnichenko L I *Solar Cosmic Rays* (Dordrecht: Kluwer Acad. Publ., 2001)
96. Dorman L, Zukerman I *Adv. Space Res.* **31** 925 (2003)
97. Dorman L I, in *Proc. of the 29th Intern. Cosmic Ray Conf., Pune, India, August 3–10, 2005* Vol. 1 (Eds B S Acharya et al.) (Mumbai: Tata Inst. of Fundamental Res., 2005) p. 281
98. Dorman L I "Using cosmic rays for monitoring and forecasting dangerous solar flare events," in *Neutrinos and Explosive Events in the Universe* (Eds M M Shapiro, T Stanev, J P Wefel) (Dordrecht: Springer, 2005) p. 131
99. Dorman L I, in *Proc. of the 17th ESA Symp. on European Rocket and Balloon Programmes and Related Research, Sanefjord, Norway, 2005* (Ed. B Warmbein) (Noordwijk: ESA Publ. Division, 2005) p. 219
100. Dorman L I et al. *IEEE Trans. Plasma Sci.* **32** 1478 (2004)
101. Dorman L I, in *Proc. of the 30th Intern. Cosmic Ray Conf., Merida, Mexico, July 3–11* Vol. 1 (Eds R Caballero et al.) (Mexico City: Univ. Nacional Autónoma de México, 2008) p. 175
102. Dorman L I et al., in *Proc. of the 28th Intern. Cosmic Ray Conf., Tsukuba, Japan, July 31–August 7* Vol. 6 (Eds T Kajita et al.) (2003) p. 3553

PACS numbers: 92.60.Pw, 93.85.Jk, 94.20.Ss
DOI: 10.3367/UFNe.0180.201005h.0527

Global electric circuit research: achievements and prospects

E A Mareev

1. Introduction

The atmosphere is the most volatile and vulnerable of Earth's shells forming the human environment, and therefore the physics of atmospheric processes attracts progressively closer attention in connection with ecological problems, weather forecasting (including cosmic weather), and climate studies. At the same time, the terrestrial atmosphere is a remarkable subject of physical–mathematical research in the area of hydrodynamics and turbulence theory, the theory of dynamical systems, optics, cosmic ray physics, and atmospheric electricity [1 – 7]. Investigations of atmospheric electricity, being one of the fundamental areas of atmospheric physics, is attracting considerable attention recently in connection with the emergence of new experimental data obtained by ground-based and satellite-borne observations, balloon-borne probing, aircraft-borne measurements, triggering lightning experiments, and laboratory modeling [7 – 9].

A new impetus to the development of concepts related to thunderstorm electricity was lent by observation of optical phenomena in the upper atmosphere correlating with thunderstorm activity — sprites, elves, and jets [8]. Various physical issues of thunderstorm electricity have been discussed, in particular, in reviews published in *Physics–Uspekhi* [10, 11]. Recent experimental and theoretical work has also led to a deeper understanding of the physical processes in the classic area of atmospheric electricity research — the study of the global electric circuit (GEC). Therefore, it is quite reasonable that several new reviews in leading international and Russian journals [12 – 15] concerned with GEC have emerged, although none of them provide an integral picture of experimental and theoretical achievements in the area. This brief report is, in essence, a detailed plan of such a review.

2. Global electric circuit concept. Observation of the global electric circuit and its variations

The GEC is a distributed current circuit formed by high-conductivity layers of the upper ocean, Earth's crust, and the atmosphere, whose conductivity is negligible in the boundary layer, but sharply (exponentially) increases with altitude (Fig. 1).

According to Wilson's concept formulated 90 years ago [16], the main sources of electromotive force (EMF), which maintains the potential of the ionosphere, are clouds, which have an electric structure (primarily cumulonimbus and nimbostratus clouds), while the areas of fair weather are zones of return currents (Fig. 2). As is well known, Wilson's concept was basically confirmed by experiment already in the late 1920s in a comparison of the diurnal variation of the atmospheric electric field above the oceans measured in fair weather conditions [the so-called Carnegie curve (Fig. 3)] with the diurnal variation of the number of thunderstorms on the terrestrial globe [17]. It turned out that both curves have a maximum at about 19 – 20 h UT and a minimum at about 4 h UT. That is why the diurnal variation of the atmospheric electric field and current has come to be known as unitary (see the well-known section "Atmospheric electricity" in *The Feynman Lectures on Physics* [18]). But numerous subsequent ground-based measurements of electric fields and currents revealed that several factors hinder extracting the unitary variation from observations near the terrestrial surface above the land: radioactivity, enhanced density of aerosol particles in the boundary layer, their charging and transfer (which perturbs the conductivity and the electric charge density), and the so-called electrode effect [14, 19, 20]. In Fig. 3, for instance, the Carnegie curve is shown together with the daily variation of the electric field plotted during 28 days of ground-based observations in fair weather in June and August of 1999 for the mid-latitude Borok geophysical observatory (GO) [14]. A morning peak caused by the development of high-intensity convection is clearly seen.

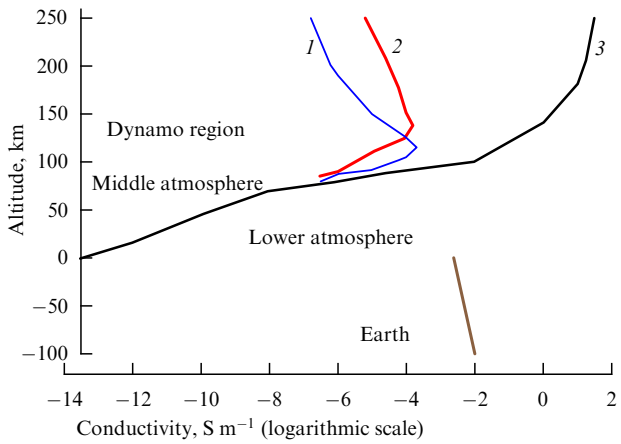

Figure 1. Typical profiles of transverse (*1* — Hall's, *2* — Pedersen's) and longitudinal (*3*) GEC conductivity [13].

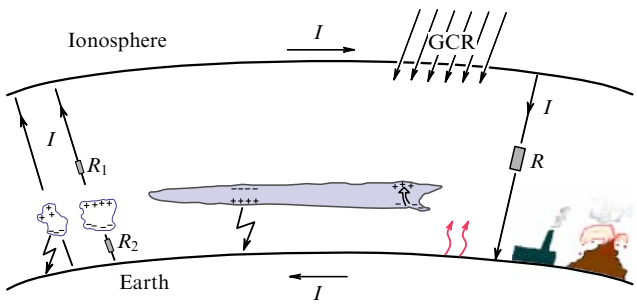

Figure 2. Schematic representation of the GEC, with the resistance $R \approx 230\ \Omega$ and the total charging current $I \approx 10^3$ A. Separately depicted are mesoscale convective systems with the horizontal scale length 150 – 200 km. Typical respective resistances of the above- and below-cloud regions are $R_1 \approx 10^4$ and $R_2 \approx 10^5\ \Omega$. GCR: galactic cosmic rays.

E A Mareev Institute of Applied Physics, Russian Academy of Sciences, Nizhnii Novgorod, Russian Federation
E-mail: mareev@appl.sci-nnov.ru

Uspekhi Fizicheskikh Nauk **180** (5) 527 – 534 (2010)
DOI: 10.3367/UFNr.0180.201005h.0527
Translated by E N Ragozin; edited by A M Semikhatov

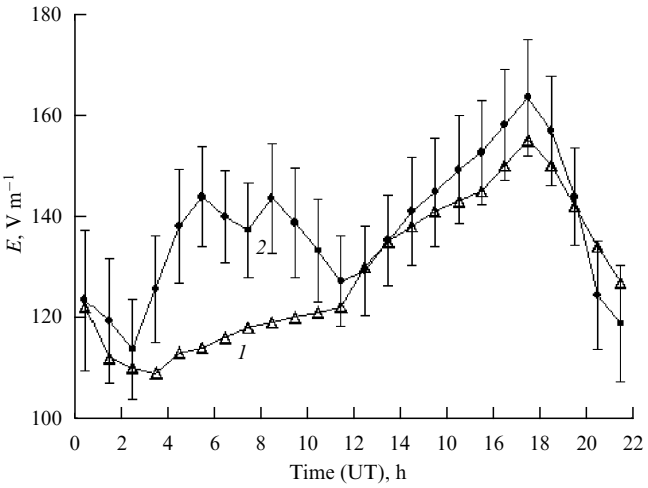

Figure 3. Unitary variation of the intensity of the atmospheric electric field (*1* — the Carnegie curve) and the average field strength according to Borok observatory observations during June and August 1999 (curve *2*). Vertical segments show the rms deviations of the hour-average field values [14].

Recent experimental data show that even at the initial stage of energy transfer from the heated underlying terrain to the atmosphere, a part of the energy is converted to electric energy in the course of convection, which manifests itself in the formation of aero–electric structures of different scales [21, 22]. Under fair weather conditions, the energy of individual structures may range from several to several hundred joules [23]. Under fog conditions, the electric energy accumulated by intense structures and their contribution to field perturbation may be substantially greater. During experiments in the Borok GO in July 2002, for instance, field perturbations with the horizontal scale length $L \approx 10$ km, height $h \approx 200$ m, and energy $W \approx 3 \times 10^4$ J were observed [24].

The theoretical analysis of the role played by convective generators in the global circuit, which takes the dynamics of convection development into account, is currently far from completion [25, 26]. We note that under the correct treatment of convective generators, the magnitude of the current that contributes to the maintenance of the ionospheric potential should depend on the magnitude of this potential, which is an inherent feature of this generator. An improved analysis of the seasonal behavior of unitary variation, according to which the peak is observed during the summer in the Northern Hemisphere, also shows the role of local effects in ground-based measurements [27, 28].

Special emphasis was recently placed on electric field measurements at high latitudes, primarily in Antarctica [29–31], where the number of cloudless days is quite large and the boundary layer is more stable due to the low temperature, although additional complications caused by geophysical effects emerge. Taking the effect of magnetospheric sources and the corresponding data averaging into account, it has been possible to reveal the diurnal variation at the South Pole and the Vostok Station [30, 31]. Therefore, despite the complexity of ground-based measurements, the exclusion of local and regional effects permits revealing the manifestations of global variations of the ionospheric potential. But the most direct way of measuring this quantity is to measure the vertical electric field strength profile in the atmosphere [12, 28, 32].

At present, the following experimental facts, along with the diurnal variation, may be considered confirmations of the existence of the global circuit:

1) the continuity of the current density with the height up to the altitudes of several dozen kilometers (see, e.g., Ref. [33], where data are outlined to show that at altitudes below 31 km, the positive j_+ and negative j_- current densities remain invariable, $j_+ \approx j_- \approx 2.5$ pA m^{-2});

2) the close values of the Earth–ionosphere potential difference measured at globally spaced points (Darwin, Australia: 220 kV; Weston, USA: 235 kV) [32].

We note that the potential difference between Earth and the upper part of the atmosphere obtained in balloon-borne measurements inside thunder clouds is also close to the values of the ionospheric potential despite the large values of the field and its variations [34] (see, e.g., Ref. 5 in Section 3).

One of the most important recent experimental achievements in the area of atmospheric electricity is the continuous (beginning in 1995) space observations of the number of lightning flashes made aboard the NASA satellites Microlab-1 (instrument: Optical Transient Detector (OTD), 1995–2000) and TRMM (Tropical Rainfall Measuring Mission) (instrument: Lightning Image Sensor (LIS), launched in 1997) [35–37]. An analysis of these observations, in particular, allowed elucidating several questions associated with the diurnal variation and, first and foremost, providing a quantitative estimate of the relative contribution from different regions of the highest thunderstorm activity to the global circuit: Africa (the Congo river basin), South America (the Amazon basin), and Southeast Asia [38, 39]. It also allowed revealing intense centers of thunderstorm activity at higher latitudes. The results of investigations confirmed that the thunderstorm activity of the African source prevailed, but its contribution to the diurnal variation was not the greatest, which is related to the governing role of quasistationary currents caused by thunder clouds and by nimbostratus clouds (including those not accompanied by a lightning storm but having a developed electric structure). The basic problem of the current balance between thunder and nimbostratus clouds and the GEC on the whole remains insufficiently studied, which invites additional ground-based and balloon- and aircraft-borne measurements [40, 41].

It is noteworthy that a significant (though episodic) contribution to the global circuit may also be due to generators arising from the charging of particles in dispersed multiphase dust and aerosol flows [42]. In this case, a significant role may be played by the difference in mobility of ions and ion clusters [43], including those related to seismic activity [44].

It is well known that a significant contribution to the GEC potential and current distributions is made by ionospheric and magnetospheric generators, along with generators located in the lower part of the atmosphere [14, 45]. In the polar cap, the morning–evening potential difference 40–100 kV (with the total current of the order of 10^6 A) is generated by the magnetospheric dynamo, which is a magnetohydrodynamic (MHD) generator that converts the kinetic energy of the solar wind to electric energy. Under low geomagnetic activity, for a horizontal source size of the order of 500 km, the contribution of the electric fields of magnetospheric convection may be responsible for about 20% of the variations of the high-latitude surface electric field [45]. Under magnetic storm conditions, the field perturbations and the latitude scale of the influence of this generator are

substantially greater. The electric field variations caused by the dynamo action of tidal waves in the E-region of the ionosphere amount to 5% of the average mid-latitude field intensity (the potential difference at ionospheric altitudes is 5 – 15 kV and the total current is of the order of 10^5 A).

The authors of Refs [46–49] draw attention to the existence of another potentially important source of atmospheric electricity, a planetary electric generator, which is due to the non-solid-state character of rotation of the planetary plasma shell. The output voltage of the planetary generator, of the order of the unipolar induction EMF $U = M\omega_0/cR$ (where M is the magnetic moment of the planet, and ω_0 and R are its angular velocity and radius), is applied to the atmospheric gap as the highest-resistance part of the global electric circuit.

Two regimes of planetary generator operation are considered in the model constructed in Refs [47, 48]: 1) an 'idle' regime, which corresponds to the planet with 'fair' weather and with currents of other sources nonexistent in the atmosphere; 2) an operation regime that involves the distributed EMF of unipolar induction and thunderstorm external currents. Reasonable characteristics of GEC parameters have been obtained. An experimental investigation of the role of the planetary generator in the global circuit invites simultaneous measurements of the ionospheric potential and the atmospheric current at mid-latitudes and on the equator.

Because of the significance of the role of sources located in the upper atmosphere, the ionospheric and magnetospheric current systems are sometimes included in the GEC concept [44, 50].

We note that recent years have seen the emergence of the practice to consider, along with the classical quasistationary current circuit termed the "direct current (DC) circuit" in the English-language literature, its attendant circuit, the "alternating current (AC) circuit," which is the Earth–ionosphere resonator [15]. An analysis of the corresponding global electromagnetic resonances (the so-called Schumann resonances) yields a wealth of information about thunderstorm activity sources on the terrestrial globe [15, 51, 52].

In recent years, deeper insight has been gained into the role of cosmic rays in the global circuit and particularly in thunder clouds, although several problems remain unsolved, which are related, in particular, to lightning initiation and to the generation of high-energy particles and X- and gamma-ray photons under thunderstorm conditions [10, 52–54].

It is noteworthy that some authors' 'challenges to the GEC concept' [50, 53] are most likely associated with too narrow an understanding of the classical GEC concept, quite frequently treated, in particular, as a 'spherical capacitor' model [55]. The definition of the GEC as a distributed current circuit and a detailed accounting for different generators (electrohydrodynamic as well as magnetohydrodynamic) permit considering the GEC concept as a well-established self-consistent theory, which nevertheless calls for further development.

3. Modeling the global electric circuit. Generators and their models. Lightning discharges

The foundations of the model for describing the GEC in the framework of a steady-state approximation were formed by the mid-1980s. The most common steady-state model was proposed by Roble and Hays [45, 56]. For sources, the authors of this model considered point dipole current sources in the background of given altitudinal and latitudinal conductivity profiles.

The theoretical description of the GEC relies on the consideration of fields and currents of individual stationary sources in planar geometry [57 – 59]. This consideration is remarkable, more specifically, in that it exhibits the necessity of GEC formation "with the participation of the ionosphere." In fact, by considering a point source of the current in a medium with as exponentially increasing conductivity, it is easy to find an analytic expression for the potential (Green's function)

$$\varphi(R,z) = \frac{I}{4\pi\sigma_0}\exp\left(-\frac{z+h}{2H}\right)\frac{\exp\left[-r/(2H)\right]}{r}\,,$$
$$r = \left[R^2 + (z-h)^2\right]^{1/2}, \qquad (1)$$

where $\sigma = \sigma_0 \exp(z/H)$, h is the coordinate of the point-like source, and z and R are the vertical and horizontal coordinates of the observation point. In the presence of a perfectly conducting boundary at $z = 0$, the total potential is found by adding expression (1) to the potential of a point current $-I\exp[-h/(2H)]$ placed at the point $z = -h$ [59]. By calculating the field $\mathbf{E} = -\nabla\varphi$ for $z > h$ and integrating $j_z = E_z$ with respect to transverse coordinates, it is easy to find the upward-flowing current (towards the upper layers of the atmosphere) as $I_0 = I[1 - \exp(-h/H)]$. This expression shows, first, that the exponential increase in the conductivity necessarily implies that a part of the current in the vicinity of a cloud flows to the ionosphere and, second, that the fraction of current flowing to the ionosphere (in comparison with the fraction that closes to Earth in the neighborhood of the cloud) increases sharply with the cloud altitude above the earth. For distributed current sources with a small transverse size, the picture is qualitatively the same (Fig. 4).

The Roble–Hays model with a 5° resolution in latitude and longitude allowed obtaining the distribution of the potential in the atmosphere under some model assumptions about the mean distribution of point-like sources in the main regions of thunderstorm activity. Subsequently elaborated were models that took transient point-like sources, distributed point-like sources of small transverse size, and conductivity perturbations into account [60 – 63], but these effects were not included in the GEC model.

As the experimental data about stationary electric sources in the atmosphere were being accumulated, an evident necessity was recognized to include several new facts into

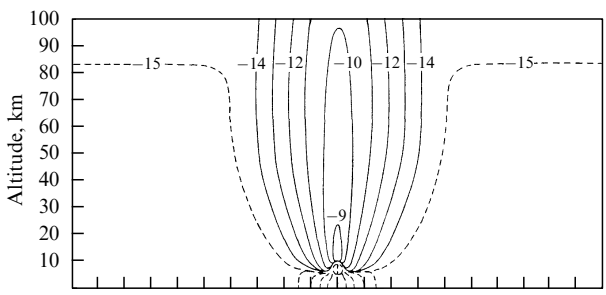

Figure 4. Isolines of the vertical current density component in the vicinity of a source above a conducting surface [59]. The numbers at the curves correspond to the values of $\log_{10}(j_z[\mathrm{A\ m^{-2}}])$. The centers of ±50 C charges are at the altitudes 5 and 10 km.

the model that were revealed during relatively recent experimental campaigns. First and foremost, balloon-borne measurements of the electric structure of developed thunder clouds demonstrated the existence of a complex multilayer electric structure (with up to eight layers); the regions with different convection rates could have different electric structures [63]. Furthermore, direct measurements of the electric structure of large-scale thunderstorm conglomerates — mesoscale convective systems (MCSs) — revealed the existence of a single quasistationary layered electric structure in stratiform regions with the transverse scale size of several hundred kilometers. The approach developed in [34] permitted both of these thunderstorm generator features to be included in simulations.

In the case of distributed steady-state electric sources, the system of Maxwell equations reduces to static current equations, which can be solved analytically under certain conditions. According to the approach outlined in Ref. [34], to model a large-scale electric cloud structure, it suffices to specify the altitudinal conductivity profile and construct the distribution of vertical external currents that provide the observed altitude profile of the electric field. To state it in different terms, it is required to solve the inverse problem of current statics and reconstruct the source from the known measured distribution of the electric field; after that, by solving the direct problem, the current density and electric field can be found both inside the cloud and in its neighborhood. In accordance with observations, the complex altitudinal electric structure of convective systems is conveniently represented as a set of horizontal layers of the vertical external current:

$$\mathbf{j}_{\rm ex}(\mathbf{r},z)=\begin{cases}0, & z<z_-\,, \quad z>z_+;\\ j_{\rm ex}(\mathbf{r})\,\mathbf{z}_0, & z_-<z<z_+,\end{cases} \tag{2}$$

where z_- and z_+ are the lower and upper layer boundaries, $j_{\rm ex}(\mathbf{r})$ is the distribution of the external current amplitude in the horizontal plane, and $\mathbf{z}_0$ is the vertical unit vector. In a simple case, the conductivity distribution has the form

$$\sigma(z)=\begin{cases}\sigma_1, & z\leqslant 0\,,\\ \sigma_0\,\exp\left(\dfrac{z}{H}\right), & z>0\,,\end{cases} \tag{3}$$

where $\sigma_0\approx 5\times 10^{-14}$ S m^{-1} is the specific electric conductivity of the atmosphere at the terrestrial surface, $\sigma_1\approx 10^{-3}$ S m^{-1} is the electric conductivity of Earth, and $H\approx 6\times 10^3$ m is the reduced height of atmospheric conductivity. Profile (3) is in a reasonably good agreement with the conductivity distribution in domains of fair weather for altitudes below approximately 70 km. In accordance with the static-current approximation, the electric field is assumed to be potential, $\mathbf{E}=-\nabla\varphi$, and the conduction current density is of the form $\mathbf{j}=-\sigma\nabla\varphi$. In this case, the total current continuity condition gives the following equation for the electric potential:

$$\operatorname{div}\left[-\sigma\nabla\varphi+\mathbf{j}_{\rm ex}(\mathbf{r},z)\right]=0\,. \tag{4}$$

The boundary conditions for Eqn (4) follow from the continuity of the potential and the vertical component of the total current density at the interfaces of the media and the layer, as well as from the unperturbed state of the potential φ at long distances from the source: $\varphi(r\to\infty,z)=0$, $\varphi(r,z\to\infty)=0$. It is significant that the use of a planar external current layer as an element of electric structure is justified both for thunderstorms with a moderate transverse size and for an extended stratiform region of mesoscale convective systems, whose electric structure, as shown by direct measurements, differs little at different points of the domain and at different stages of the evolution of the system.

Examples of calculations performed in accordance with the approach outlined above may be found in Refs [34, 64, 65]. Figures 5 and 6 illustrate the results of these calculations. The resultant model enabled calculating electric fields and currents in the vicinity of an MCS and estimating the total current flowing toward the ionosphere. The calculated data showed that the contribution of MCSs to the global electric circuit may greatly exceed the contribution of individual thunderstorms. An important conclusion was that despite a significant perturbation of the electric potential in the convection region (ranging up to several hundred megavolts), the leading contribution to the total vertical current and the structure of fields and currents in the vicinity of an MCS is due to the stratiform region (for the type-B MCS model considered, for instance, the total vertical current from the stratiform region is -25 A, while the contribution from

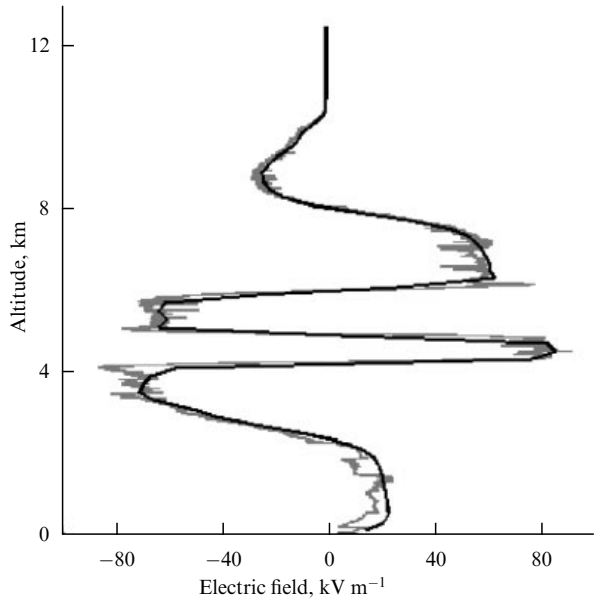

Figure 5. The altitude profile of the electric field (bright curve) obtained via balloon-borne measurements in the stratified type-A MCS stratiform region above Oklahoma on May 24, 1991 and a model electric field distribution (dark curve) [65].

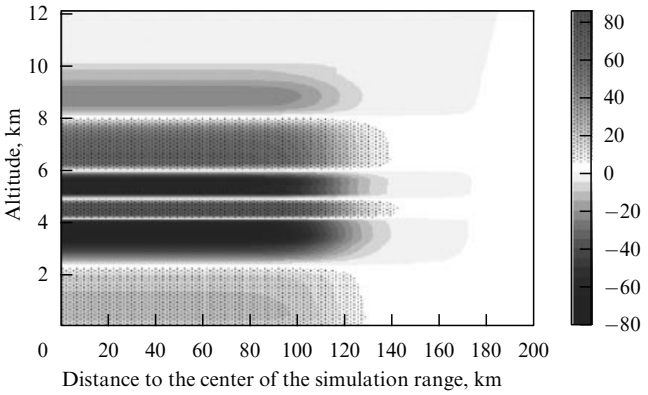

Figure 6. Distribution of the vertical component of the electric field formed by a stratiform region of mesoscale convective systems [65].

the convection region does not exceed 0.5 A). Depending on the number, transverse dimension, position, and amplitude of external current layers, the total contribution from an MCS to the global circuit may be 'positive' as well as 'negative,' when the system is a sink in the global circuit. This circumstance impels giving much consideration to the statistics and evolutionary features of MCSs in future GEC research.

The described approach to the modeling of sources also enabled deriving analytic expressions for the cloud energy and the average rate of its dissipation in the atmosphere with an exponential conductivity profile [66]. It was assumed that the external current has a smooth transverse distribution $j_{ex} = j_0 \exp(-r^2/a^2)$ and flows in the layer between the z_- and z_+ levels corresponding to the lower and upper levels of electric charge localization. Rather simple expressions are obtained when the transverse cloud size a is small or, conversely, large in comparison with the conductivity gradient scale length H. The expressions obtained in Ref. [66] permit investigating the dependence of source energy characteristics on the parameters a, H, σ_0, z_-, and z_+, comparing the contribution of different cloud regions, and estimating the role of the horizontal field component in the energy balance of the circuit. They yield reasonable values for the energy and its dissipation rate for current density values of the order of $1-10$ nA m^{-2}, which maintains the charge distribution in the cloud.

An important line in the further development of GEC simulations is the inclusion of transient processes [67–69]. In particular, the question of the contribution to the GEC from lightning and transient currents flowing after lightning flashes remains insufficiently investigated. It is commonly assumed that the electric charge transferred by a lightning flash from a cloud to ground is rapidly redistributed over the terrestrial surface and therefore makes a direct contribution to the total charge of Earth and to the effective charging current (or discharging current, depending on the flash polarity) of the GEC. It is well known, however, that this rapid process (the duration of a typical negative flash is not longer than several hundred milliseconds) is followed by a slow transient stage caused by charge redistribution in the surrounding atmosphere. The transient stage (ranging up to several dozen or hundred seconds in duration) results in a partial neutralization of the charge transferred to ground and in charge transfer to the ionosphere. The charges transferred to ground and the ionosphere after the transient stage are the total contribution from the lightning flash to the GEC.

The dynamics of transient currents were investigated in Ref. [67]. Cloud-to-ground flashes and intracloud flashes were found to generate, along with short-duration currents, transient currents of substantial magnitude. The cloud-to-ground flashes of 'normal polarity' (i.e., those that transfer a negative charge to Earth) charge the global circuit, while intracloud flashes of 'normal polarity' result in its relaxation. The efficiency of cloud-to-ground-type flashes (i.e., the ratio between the charges transferred to the ionosphere and to Earth) depends heavily on the charge location altitude in the conducting atmosphere and varies from 15% to 90% in the range from 1 km to 14 km above Earth in the model with an exponential conductivity. The efficiency of intracloud flashes is on average much lower than for cloud-to-ground flashes, but their average contributions to the GEC current may be comparable because the number of intracloud flashes is much larger than the number of cloud-to-ground flashes. The estimates of the global balance of transient currents showed that the contribution of the transient currents caused by lightning flashes during a period of high-intensity thunderstorm activity may be of the same order of magnitude as the contribution of the quasistationary current. In the global current balance, however, the contribution of transient currents is unlikely to exceed 20%.

The last decade or so has seen the introduction of GEC models that take the influence of conductivity anisotropy at high altitudes, the features of large-scale atmospheric conductivity distribution, and nonstationary effects into account [68–72]. A new impetus to the development of nonstationary models, including 'electrotechnical' ones [73], was lent by the discovery and active studies of discharges in the middle atmosphere correlating with thunderstorm activity in the troposphere.

A common avenue of GEC simulation is the development of self-consistent models capable of taking both nonstationary effects and the nonuniformity of conductivity distribution into account, including the effects related to cosmic ray flux perturbations, high-energy particle precipitation, aerosol particle ejections (for instance, in volcanic eruptions), and radioactivity. The development of the electric dynamo applied to different layers of the atmosphere, including the middle atmosphere, also appears to be important for the GEC theory [74]. In the future, it is highly desirable to elaborate combined models that self-consistently include the hydrodynamics and electrodynamics of the upper atmosphere [75] and the general circulation of the atmosphere and the ocean [76]. Such a GEC model remains to be constructed.

4. The global electric circuit as an open dissipative system

The main part of the energy flux supporting the global electric circuit comes in the form of solar radiation energy (1.37×10^3 W m^{-2}), which is the source of labile energy (which comprises internal, $\sim 8.6 \times 10^{23}$ J, and potential, $\sim 3.6 \times 10^{23}$ J, energies), the kinetic energy of the atmosphere (ranging from 6×10^{20} J to 9×10^{20} J depending on the season), and electric field energy. Of special significance to the dynamics of electric field energy accumulation and dissipation in the atmosphere are the processes of water phase transformation: just the delivery of the latent heat of water vapor condensation to the atmosphere (which amounts in magnitude to about one fourth of the solar energy flux) is responsible for the maintenance of intense ascending flows and the formation of hydrometeors, which play the key role in the electrization of clouds. The corresponding 'pyramids' of the electric energy storage and dissipation in the atmosphere are presented in Ref. [14].

To date, the authors of only a few studies have discussed the problem of the dynamics of electric energy accumulation and dissipation in a thunderstorm cloud. Based on in situ field measurements, the energy values 5×10^{11} J and 2×10^{12} J for two mesoscale convective systems, and 2×10^{11} J for a high-power thunderstorm cloud with an anvil were obtained in [77]. This is sufficient for generating several hundred/thousand ordinary lightning flashes and only 10–100 high-energy positive cloud-to-ground flashes.

The foregoing estimates are supported by the simulation results in [34]; their three-dimensional model of field and current distributions in the neighborhood of mesoscale convective systems yields a value of the order of 10^{11} J for

the total energy accumulated in a system 200 km in size, with the ohmic loss of 3×10^9 W. Therefore, the electric energy accumulated inside a thunderstorm cloud is equal to about $10^{10} - 10^{11}$ J, but may exceed 10^{12} J for severe clouds. Because the average fair-weather current is equal to 2 pA and the average vertical current of a thunder cloud, which charges the global circuit, is usually estimated at 1–2 A, the average number of thunderstorms on the planet may be taken to be equal to 10^3. Their average accumulated energy may be estimated at 3×10^{13} J.

As suggested by the observations of sferics [15], normally up to 10 high-power sferics (the so-called Q-bursts) are detected in 1 s, whence it follows that several dozen high-power thunderstorms simultaneously boom on the globe, which yields 5×10^{13} J in total. We emphasize that the quasistationary currents of a part of severe thunderstorms and MCSs discharge the circuit [34], although they undoubtedly make a substantial contribution to the total electric energy of the atmosphere.

An additional contribution to the total electric energy is made by nimbostratus clouds. According to calculations, the average energy dissipated in the vicinity of a thunder cloud due to conduction currents is of the order of 3×10^8 W, and may range up to 3×10^9 W for intensive clouds, which yields the global total of 3×10^{11} W. A part of the energy is also dissipated by lightning flashes and sprites. For the flash energy 2×10^9 J and an average frequency of lightning flashes 50 s^{-1} [35], we obtain the global average dissipation power 10^{11} W. The average value of total electric energy dissipation per unit time is 4×10^{11} W.

For comparison, we mention that the electrostatic energy concentrated in the 'global capacitor' is estimated as $W = j_0^2 R_E^2 H/(2\sigma_0^2) \approx 4.4 \times 10^{18}$ erg $= 4.4 \times 10^{11}$ J, where R_E is the radius of Earth, $H \approx 6$ km, $\sigma_0 \approx 10^{-14}$ S m^{-1}, and the atmospheric current amplitude $j_0 \approx 2 \times 10^{-12}$ A m^{-2}. The rate of energy dissipation due to ohmic losses is $P = 4\pi\sigma_0 W \approx 5 \times 10^8$ W.

Therefore, the electric energy generated by thunderstorm clouds and by intensive nimbostratus clouds amounts to $3 \times 10^{13} - 10^{14}$ J on average, which is two to three orders of magnitude higher than the energy concentrated in the global spherical Earth–ionosphere capacitor. The average rate of the electric energy dissipation due to conduction currents and lightning flashes is equal to $3 \times 10^{11} - 3 \times 10^{12}$ W; this corresponds to the electric energy lifetime about 100 s [66]. The foregoing estimates characterize the global circuit as the most agile of the existing geophysical systems with a rather high energy storage.

5. Global electric circuit in the climat system of Earth and other planets of the Solar System

GEC climatology studies were started after Williams's work, which drew attention to the possible dependence of lightning activity (and accordingly of the state of DC and AC global circuits) on the average temperature [80]. Experimental data related to the evolution of the ionospheric potential during the 20th century are discussed in Refs [12, 15, 19]. Reliable and systematic measurement data on this quantity available to date are insufficient to judge about statistically significant variations for several decades, although a significant increase in the ionospheric potential was observed during the 1960–1967 period, which was obviously related to nuclear weapon tests in the atmosphere [12]. Nor is the role played by generators and dissipation regions in the GEC in the course of its evolution or the influence of 'space weather' quite clear [19].

We note that the GEC occupies a unique place among natural systems subject to climat changes. First, as noted above, due to the special character of the conductivity distribution with altitude, the global circuit naturally averages the Earth–ionosphere potential difference and thereby determines a global index — the ionospheric potential that depends on the level of global thunderstorm activity [15]. Second, thunderclouds are an extreme weather phenomenon attended with destructive rainfalls, squalls, and hail; it is natural that the study of climatic trends in extreme events arouses special interest [78, 79]. Third, there are several physical mechanisms through which electric phenomena themselves may influence the climate (see, e.g., Refs [81, 82]). It is therefore necessary to investigate both these mechanisms and the feedback relations between atmospheric electric phenomena and the variations of the climat system state.

In the last few years, high-resolution physical–mathematical models have become one of the most important instruments for studying the climate [76]. But the inclusion of atmospheric electric effects in climate models encounters several problems. The most important of them is the necessity of parameterizing the quantity and intensity of thunderclouds and lightning flashes in relation to the main physical characteristics of convective cloudiness; a step in the spatial grid in atmospheric and oceanic circulation models, even in the highest-resolution models, is large in comparison with the scale length of convection responsible for thundercloud formation [83]. The problems of the parameterization of thunderclouds as a source of nitric oxides in the atmosphere, which are responsible for the perturbations of atmosphere composition (including ozone and hydroxyl radical), and the disturbance of the radiation balance are being widely discussed at present [84]. In particular, numerical experiments were performed with the use of a high-resolution chemistry-climate model [85] and the average-climate parameterization of thunderstorm activity to study the influence of thunderstorms on the composition and radiation balance of the atmosphere and the backreaction of climate changes on the frequency and intensity of thunderstorm phenomena [86]. Further development of the physical parameterizations will allow climate models to include the feedback relations between changes in nitric oxide content and the subsequent change in the densities of ozone and other atmospheric gases, which is able to affect meteorological conditions and hence the rate of nitric oxide production in lightning discharges and the state of the GEC.

The interest in electric effects in planetary atmospheres, which is related to investigations of the possible role of atmospheric electricity in climatic processes, the formation of biospheres, and the interrelation between 'planetary' and 'space weather,' is largely stimulated by the new data obtained using interplanetary spacecraft (including Cassini, Mars Express, and Venus Express) [9]. A brief analysis of the features of the GECs for the atmospheres of other planets of the Solar System can be found in Ref. [87].

6. Summary

Several new results have recently been obtained, which have led to a deeper understanding of the physical processes in the global electric circuit.

1. A new description of the global atmospheric electric circuit has been proposed and substantiated. This description relies on the findings of an analysis of the energy characteristics of the quasistationary field in thunderstorm and fair weather regions. The resultant estimates characterize the global circuit as the most agile system among the existing geophysical systems with a rather high energy level. The further development of research into the energy characteristics of the global circuit should involve a more comprehensive study and simulations of sources, an elaboration of gasdynamic lightning models, and a monitoring of thunderstorm and lightning activities.

2. The transient currents that flow after lightning flashes and the contribution of these currents to the global electric circuit have been investigated.

3. Several (primarily numerical) new models have been developed, which permit describing nonstationary and electromagnetic processes in the global electric circuit in planar and spherical geometries. Models of stationary global current systems have also been developed. It is hoped that the nonstationary models of the global circuit will soon be brought to a level enabling the description of large-scale geophysical perturbations and the long-term evolution of the system, gaining a deeper insight into the properties of atmospheric electricity for other planets of the Solar System. Of special interest are the studies of thunderstorm and lightning climatology and simulations of the global atmospheric electric circuit in different scenarios of climate change.

Acknowledgements. This work was supported by the Russian Foundation for Basic Research (Grant No. 09-05-13600-ofi_ts), Program No. 4 of the Presidium of the RAS, and Program No. 11 of the Physical Sciences Division of the RAS.

References

1. Houghton J *The Physics of Atmospheres* 3rd ed. (Cambridge: Cambridge Univ. Press, 2002)
2. Dymnikov V P *Ustoichivost' i Predskazuemost' Krupnomasshtabnykh Atmosfernykh Protsessov* (Stability and Predictability of Large-Scale Atmospheric Processes) (Moscow: IVM RAN, 2007)
3. Visconti G *Fundamentals of Physics and Chemistry of the Atmosphere* (Berlin: Springer-Verlag, 2001)
4. Golitsyn G S *Dinamika Prirodnykh Yavlenii, Klimat, Planetnye Atmosfery, Konvektsiya, Volnovye i Sluchainye Protsessy* (Dynamics of Natural Phenomena. Climate, Planetary Atmospheres, Convection, Wave and Stochastic Processes) (Moscow: FIZMATLIT, 2004)
5. Lorenz E N *J. Atmos. Sci.* **63** 2056 (2006)
6. Onishchenko O G, Pokhotelov O A, Astaf'eva N M *Usp. Fiz. Nauk* **178** 605 (2008) [*Phys. Usp.* **51** 577 (2008)]
7. Rakov V A, Uman M A *Lightning: Physics and Effects* (Cambridge: Cambridge Univ. Press, 2003)
8. Fullekrug M, Mareev E A, Rycroft M J (Eds) *Sprites, Elves and Intense Lightning Discharges* (Dordrecht: Springer, 2006)
9. Leblanc F et al. (Eds) *Planetary Atmospheric Electricity* (New York: Springer, 2008)
10. Gurevich A V, Zybin K P *Usp. Fiz. Nauk* **171** 1177 (2006) [*Phys. Usp.* **44** 1119 (2001)]
11. Bazelyan E M, Raizer Yu P *Usp. Fiz. Nauk* **170** 753 (2000) [*Phys. Usp.* **43** 701 (2000)]
12. Markson R *Bull. Am. Met. Soc.* **88** 223 (2007)
13. Rycroft M et al. *Space Sci. Rev.* **137** 83 (2008)
14. Anisimov S V, Mareev E A *Fizika Zemli* (10) 8 (2008) [*Izv. Phys. Solid Earth* **44** 760 (2008)]
15. Williams E R *Atmos. Res.* **91** 140 (2009)
16. Wilson C T R *Phil. Trans. R. Soc. Lond. A* **221** 73 (1921)
17. Whipple F J W *Quart. J. R. Met. Soc.* **55** 351 (1929)
18. Feynman R R, Leighton R B, Sands M *The Feynman Lectures on Physics* Vol. 2 (Reading, Mass.: Addison-Wesley Publ. Co., 1964) [Translated into Russian: *Feinmanovskie Lektsii po Fizike* Vol. 5 (Moscow: Mir, 1977) p. 174–198]
19. Harrison R G *Surv. Geophys.* **25** 441 (2004)
20. Mareev E A *Space Sci. Rev.* **137** 373 (2008)
21. Anisimov S V, Mareev E A, Bakastov S S *J. Geophys. Res.* **104** (D12) 14359 (1999)
22. Anisimov S V, Mareev E A, Shikhova N M, Dmitriev E M *Geophys. Res. Lett.* **29** (24) 70-1 (2002)
23. Anisimov S V et al. *Atmos. Res.* **76** 16 (2005)
24. Mareev E A, Anisimov S V, in *Proc. 12th Intern. Conf. on Atmospheric Electricity, Versailles, France, 2003*, p. 797
25. Willett J C *J. Geophys. Res.* **88** 8453 (1983)
26. Morozov V N *Nonlinear Proc. Geophys.* **13** 243 (2006)
27. Adlerman E J, Williams E R *J. Geophys. Res.* **101** (D23) 29679 (1996)
28. Mühleisen R, in *Electrical Processes in Atmosphere*: *Proc. XV Intern. Conf. on Atmospheric Electricity, 1974*, p. 467
29. Frank-Kamenetsky A V et al. *J. Geophys. Res.* **106** (A1) 179 (2001)
30. Burns G B et al. *J. Geophys. Res.* **110** (D10) D10106 (2005)
31. Reddell B D et al. *J. Geophys. Res.* **109** (A9) A09308 (2004)
32. Markson R, Ruhnke L H, Williams E R *Atmos. Res.* **51** 315 (1999)
33. Gringel W, Rosen J M, Hofmann D J, in *The Earth's Electrical Environment* (Eds E P Krider, R G Roble) (Washington, DC: Natl. Acad. Press, 1986) p. 166
34. Davydenko S S et al. *J. Geophys. Res.* **109** D11103 (2004)
35. Christian H J et al. *J. Geophys. Res.* **108** (D1) 4005 (2003)
36. Mach D M et al. *J. Geophys. Res.* **112** D09210 (2007)
37. Bailey J C et al., in *Proc. of the 13th Int. Conf. on Atmospheric Electricity, Beijing, China, 2007* Vol. 2 p. 657
38. Williams E R, Heckman S J *J. Geophys. Res.* **98** (D3) 5221 (1993)
39. Williams E R, Sátori G *J. Atmos. Solar-Terr. Phys.* **66** 1213 (2004)
40. Mach D M et al. *J. Geophys. Res.* **114** D10204 (2009)
41. Thomas J N, Holzworth R H, McCarthy M P *Atmos. Res.* **91** 153 (2009)
42. Mareev E A, in *Nelineinye Volny-2008* (Nonlinear Waves-2008) (Executive Editors A V Gaponov-Grekhov, V I Nekorkin) (N. Novgorod: IPF RAN, 2009) p. 143
43. Smirnov V V *Ionizatsiya v Troposfere* (Ionization in the Troposphere) (St. Petersburg: Gidrometeoizdat, 1992)
44. Pulinets S A et al. *Usp. Fiz. Nauk* **168** 582 (1998) [*Phys. Usp.* **41** 515 (1998)]
45. Roble R G, Tzur I, in *The Earth's Electrical Environment* (Eds E P Krider, R G Roble) (Washington, DC: Natl. Acad. Press, 1986) p. 206
46. Bespalov P A, Chugunov Yu V *Dokl. Ross. Akad. Nauk* **337** 467 (1994) [*Dokl. Phys.* **39** 553 (1994)]
47. Bespalov P A, Chugunov Yu V, Davydenko S S *J. Atmos. Terr. Phys.* **58** 605 (1996)
48. Bespalov P A, Chugunov Yu V *Izv. Vyssh. Uchebn. Zaved. Radiofiz.* **40** 138 (1997) [*Radiophys. Quantum Electron.* **40** 87 (1997)]
49. Soldatkin A O, Chugunov Yu V *Fiz. Plazmy* **29** 72 (2003) [*Plasma Phys. Rep.* **29** 65 (2003)]
50. Bering E A (III), Few A A, Benbrook J R *Phys. Today* **51** (10) 24 (1998)]
51. Nickolaenko A P, Hayakawa M, Sekiguchi M *Geophys. Res. Lett.* **33** L06823 (2006)
52. Rycroft M J, Israelsson S, Price C *J. Atmos. Solar-Terr. Phys.* **62** 1563 (2000)
53. Harrison G *Geophys. Res. Lett.* **29** (14) 1660 (2002)
54. Gurevich A V et al. *Usp. Fiz. Nauk* **179** 779 (2009) [*Phys. Usp.* **52** 735 (2009)]
55. Imyanitov I M, Shifrin K S *Usp. Fiz. Nauk* **76** 593 (1962) [*Sov. Phys. Usp.* **5** 292 (1962)]
56. Hays P B, Roble R G *J. Geophys. Res.* **84** 3291 (1979)
57. Holzer R E, Saxon D S *J. Geophys. Res.* **57** 207 (1952)
58. Willett J C *J. Geophys. Res.* **84** 4999 (1979)
59. Volland H, in *CRC Handbook on Atmospherics* Vol. 1 (Ed. H Volland) (Boca Raton, FL: CRC Press, 1995) p. 65
60. Tzur I, Roble R G *J. Geophys. Res.* **90** 5989 (1985)
61. Driscoll K T, Blakeslee R J, Koshak W J *J. Geophys. Res.* **99** (D5) 10653 (1994)
62. Stansbery E K, Few A A, Geis P B *J. Geophys. Res.* **98** (D9) 16591 (1993)

63. Stolzenburg M et al. *J. Geophys. Res.* **103** (D12) 14059 (1998)
64. Davydenko S S, Marshall T C, Stolzenburg M *Atmos. Res.* **91** 165 (2009)
65. Davydenko S S, Sergeev A S, Mareev E A, in *Trudy VI Ross. Konf. po Atmosfernomy Elektrichestvu* (Proc. VIth Russ. Conf. on Atmospheric Electricity), *N. Novgorod, 1–7 October 2007*, p. 11
66. Mareev E A, Anisimov S V *Atmos. Res.* **91** 161 (2009)
67. Mareev E A et al. *Geophys. Res. Lett.* **35** L15810 (2008)
68. Kartalev M D et al. *J. Atmos. Solar-Terr. Phys.* **68** 457 (2006)
69. Dumin Yu V *Adv. Space Res.* **30** 2209 (2002)
70. Tinsley B A, Zhou L *J. Geophys. Res.* **111** D16205 (2006)
71. Plotkin V V *Geomagn. Aeron.* **44** 624 (2004) [*Geomagn. Aeron.* **44** 624 (2004)]
72. Ma Z, Croskey C L, Hale L C *J. Atmos. Solar-Terr. Phys.* **60** 845 (1998)
73. Rycroft M J et al. *J. Atmos. Solar-Terr. Phys.* **69** 2485 (2007)
74. Mareev E A, Trakhtengerts V Yu *Izv. Vyssh. Uchebn. Zaved. Radiofiz.* **39** 797 (1996) [*Radiophys. Quantum Electron.* **39** 527 (1996)]
75. Namgaladze A A et al. *J. Atmos. Terr. Phys.* **53** 1113 (1991)
76. Dymnikov V P, Lykossov V N, Volodin E M *Izv. Ross. Akad. Nauk. Fiz. Atm. Okeana* **42** 618 (2006) [*Izv. Atmos. Ocean. Phys.* **42** 568 (2006)]
77. Marshall T C, Stolzenburg M *J. Geophys. Res.* **107** (D7) 4052 (2002)
78. Zipser E J et al. *Bull. Am. Met. Soc.* **87** 1057 (2006)
79. Price C *Atmos. Res.* **91** 479 (2009)
80. Williams E R *Mon. Weather Rev.* **122** 1917 (1994)
81. Mareev E A, in *Topical Problems of Nonlinear Wave Physics, NWP-2008: Intern. Symp., Nizhny Novgorod, 20–26 July, 2008*, p. 65
82. Futyan J M, Del Genio A D *Geophys. Res. Lett.* **34** L15705 (2007)
83. Arakawa A *J. Climate* **17** 2493 (2004)
84. Schumann U, Huntrieser H *Atmos. Chem. Phys.* **7** 3823 (2007)
85. Galin V Ya, Smyshlyaev S P, Volodin E M *Izv. Ross. Akad. Nauk. Fiz. Atm. Okeana* **43** 437 (2007) [*Izv. Atmos. Ocean. Phys.* **43** 399 (2007)]
86. Smyshlyaev S P, Mareev E A, Galin V Ya *Izv. Ross. Akad. Nauk. Fiz. Atm. Okeana* **46** (3) (2010) [*Izv. Atmos. Ocean. Phys.* **46** (3) (2010)]
87. Aplin K L *Surv. Geophys.* **27** 63 (2006)

PACS numbers: 94.05.Sd, **94.20.–y**, **94.30.–d**
DOI: 10.3367/UFNe.0180.201005i.0535

Geophysical research in Spitsbergen Archipelago: status and prospects

V V Safargaleev, E D Tereshchenko

1. Spitsbergen — a geophysical site for space weather research

The geographic position of the Spitsbergen archipelago provides a unique opportunity to solve a number of geophysical questions having important scientific and applied value. First and foremost, these are questions related to forecasting space weather.

During daytime, geomagnetic field lines connect the ionosphere over Spitsbergen with magnetospheric regions through which the energy and plasma of solar wind enter the near-Earth space. The energy collected in the magnetospheric tail is released in the course of substorms, and continuous energy influx from solar wind supports the recurrence of these most striking manifestations of space weather. The solar wind plasma that appears inside the magnetosphere mixes with the background plasma, which has essentially different properties, thus creating favorable conditions for the development of various plasma instabilities. These disturbances are also elements of space weather.

To investigate space phenomena far from Earth, the most convenient tools are 'agents' transferring information along the geomagnetic field lines, i.e., charged particles and Alfvén waves. Electrons precipitating into the ionosphere generate aurora. During the winter months, the ionosphere over Spitsbergen is not exposed to sunlight, even in daytime; this provides a unique possibility to investigate magnetopause processes by observing the daytime aurora. Disturbances generated in the process of the ion–cyclotron instability development in an anisotropic plasma are attributed, in particular, to Alfvén-type waves. The plasma anisotropy and associated wave turbulence are observed by satellites in the solar wind region directly bordering the daytime magnetopause. When the anisotropic plasma appears inside the magnetosphere on the field lines leaning on the ionosphere above Spitsbergen, the wave activity is detected by induction magnetometers as short-period geomagnetic pulsations (Pc1). The interaction of the solar wind and the interplanetary magnetic field (IMF) frozen in it with the magnetosphere also appears as a large-scale convection of magnetospheric and ionospheric plasmas. In the daytime ionosphere over Spitsbergen, the character of convection can be studied by a set of incoherent scatter EISCAT (European Incoherent Scatter Radar Systems) radars in Tromsø (TRO, Norway) and Longyearbyen (LYR, Spitsbergen), as well as by one of the auroral SuperDARN (Super Dual Auroral Radar Network) radars in Hankasalmi (HANK, Finland).

Therefore, consistent optic, magnetic, and radar observations in Spitsbergen provide a comprehensive approach to the investigation of an important formation stage of space weather, the energy and plasma influx from interplanetary space (solar wind) into the near-Earth space (magnetosphere). We note in this regard that although satellite measurements are intensively used in solving space weather problems, an analysis of ground observation data is still an effective approach, especially from the standpoint of the balance between costs and efficiency, in experimental investigations of magnetopause processes. Indeed, even if a satellite crosses the magnetopause in the 'right' place at the 'right' time (which is quite improbable), the measurements that interest us last for a few minutes only. A lasting series of ground-based observations allow following the development of a phenomenon (e.g., an abrupt change in the IMF sign or a discontinuity of the solar wind plasma pressure) for longer time intervals covering its prehistory.

The use of the ionosphere as a kind of 'screen' on which magnetospheric processes are presented also stimulates investigations of the 'screen' itself. The high variability of the Arctic-latitude ionosphere requires continuous observation. It is ineffective to obtain regular data on electron content by expensive direct rocket or satellite measurements. Cheaper, but no less informative, are the methods of remote ground-based sensing and satellite radiography. These methods allow determining the ionospheric electron density by radio waves propagating through it. Ionosonde sounding is a comparatively inexpensive method; however, it can be

VV Safargaleev, E D Tereshchenko Polar Geophysical Institute, Kola Scientific Center, Russian Academy of Sciences, Murmansk, Russian Federation
E-mail: Vladimir.safargaleev@pgia.ru

Uspekhi Fizicheskikh Nauk **180** (5) 535–541 (2010)
DOI: 10.3367/UFNr.0180.201005i.0535
Translated by S V Vladimirov; edited by A M Semikhatov

used only for investigation of the lower layers of the ionosphere. The space resolution of an ionosonde is not high. Radars make measurements with a better space resolution than the ionosonde, but they have a narrow field of view and require high expenses for their regular use.

A relatively inexpensive way to estimate the state of the ionospheric electron concentration in a space region of a few thousand kilometers along the meridian and with a height of the order of 1000 km is the satellite radio tomography method [1]. An additional advantage of this method is that it does not depend on weather and geophysical factors. Currently, satellite radiotomography is practically the only available method of continuous diagnostics of global electron density formations in the ionosphere, including gravity waves. The method can also be effectively used for localization of artificial disturbances: rocket launches, industrial emissions, and ionospheric inhomogeneities appearing because of the action of a powerful radio wave on the ionosphere.

Ionospheric research methods based on the action of powerful short-wave (SW) beams have been intensively developed over the last two to three decades. Because of ionospheric absorption of the energy of radiated radio waves, various physical phenomena are generated in the ionosphere (see, e.g., review [2]). Investigation of heating effects allows better understanding the structure of the ionosphere and the character of its natural processes. In addition, ionosphere artificial modification experiments also have an applied value. For example, one of the manifestations of heating — the generation of artificial ionospheric inhomogeneities — is used to study the influence of natural ionospheric inhomogeneities on the performance of satellite radio navigation systems.

Concentration of various diagnostic tools in northern Scandinavia stimulated, in due time, the construction of a heating facility at the EISCAT radar near Tromsø (Norway). The range of problems that this facility can solve is wide; but the participation of Russian scientists in experiments conducted there is limited and reduces to episodic expeditions. The absence of necessary portable mobile equipment, poor financing, customs formalities — this is an incomplete list of problems explaining the low activity of domestic academic science in auroral ionospheric studies by active influence methods.

A tendency to improve the situation appeared after the 2004 launch of the SPEAR (Space Plasma Exploration by Active Radar) project. The SPEAR heating facility was constructed in the framework of a project at ESR (EISCAT Svalbard Radar) near Longyearbyen (Spitsbergen). The geography of heating experiments expanded into a cusp region (during daytime), which is extremely interesting from the geophysical standpoint, and the boundaries between closed and open field lines (during nighttime). A few years earlier, the Polar Geophysical Institute (PGI) of the Kola Scientific Center, RAS, had resumed scientific investigations in the Barentsburg Observatory (BAB), which is approximately 40 km west of SPEAR. The first joint experiment on the registration of possible ionosphere modification effects by the SPEAR heating facility was conducted in February–March 2007. By that time, the PGI Observatory had already had a set of measurement facilities, including various optical, magneto- and radiometric devices.

The ionosphere is associated with a set of factors significantly affecting radio wave propagation. The high-latitude ionosphere is a more changeable formation than the middle latitude ionosphere. The tomographic investigations of ionospheric inhomogeneities done in the Spitsbergen archipelago, as well as those of the characteristics of the generation and propagation of electromagnetic waves in extremely and super low frequency (ELF–SLF) ranges in the Earth–ionosphere waveguide, can be used in solving the problems of radio communication, radiolocation, and radionavigation in the Arctic.

All the above determines the interest of the international geophysical community in investigations in Spitsbergen, an interest that is currently being realized through the establishment in the archipelago of one of the best and most convenient international scientific sites in the Arctic, with developed infrastructure and strong international connections. A new stage in PGI studies in Spitsbergen began in 2000, after the Russian Federation governmental regulation "On Financing the Activity of Russian Organizations in the Spitsbergen Archipelago" and the creation of the Interdepartmental Commission on Securing Russian Interests and Industrial and Scientific Activity in the Archipelago. It was at that time that the foundations of the northernmost Russian geophysical observatory facility were laid. Nowadays, this observatory, equipped with an extensive armory of observation tools, is an integral part of the international geophysical platform (Fig. 1).

The basis for the PGI regular observations in Barentsburg is a facility including a magnetovariational station and inductive magnetometers, a radio–tomographic receiving station, a GPS (Global Positioning System) and GLONASS (Global Navigation Satellite System) signal receiver, various optical devices, an electric field sensor, a neutron monitor, and an ozonometer to measure tropospheric ozone variations. To conduct specific experiments, additional devices are used, specifically, an SW radio interferometer facility and a precision ELF broad-band receiver. On the basis of experimental data obtained at the PGI Observatory over the number of recent years of its existence, more than 40 publications and scientific communications have been prepared. In the next sections, we briefly review those that, in our opinion, constitute a significant step forward in the above three scientific areas: space weather research, artificial ionosphere modification by SW waves, and propagation of SLF waves in the ionospheric waveguide. To conclude this section, we note that the organization and conduction of observations in severe Arctic conditions require extensive efforts and determination of the researchers. Therefore, the authors use the opportunity provided by this paper to thank those PGI researchers whose professional activity facilitated the development of the observatory and the acquisition of high-quality data.

2. Comprehensive studies of ionospheric disturbances related to processes in the magnetopause and adjoining domains

A large part of the PGI scientific results obtained in Spitsbergen is based on the data of annual collaborative campaigns for the investigation of daytime aurora dynamics in the context of ionospheric convection. These campaigns are organized by Oulu University (Finland) and the Swedish Institute of Space Physics (Kiruna, Sweden). These scientific institutions are members of the International EISCAT Association, and have long-standing partner relations with the PGI.

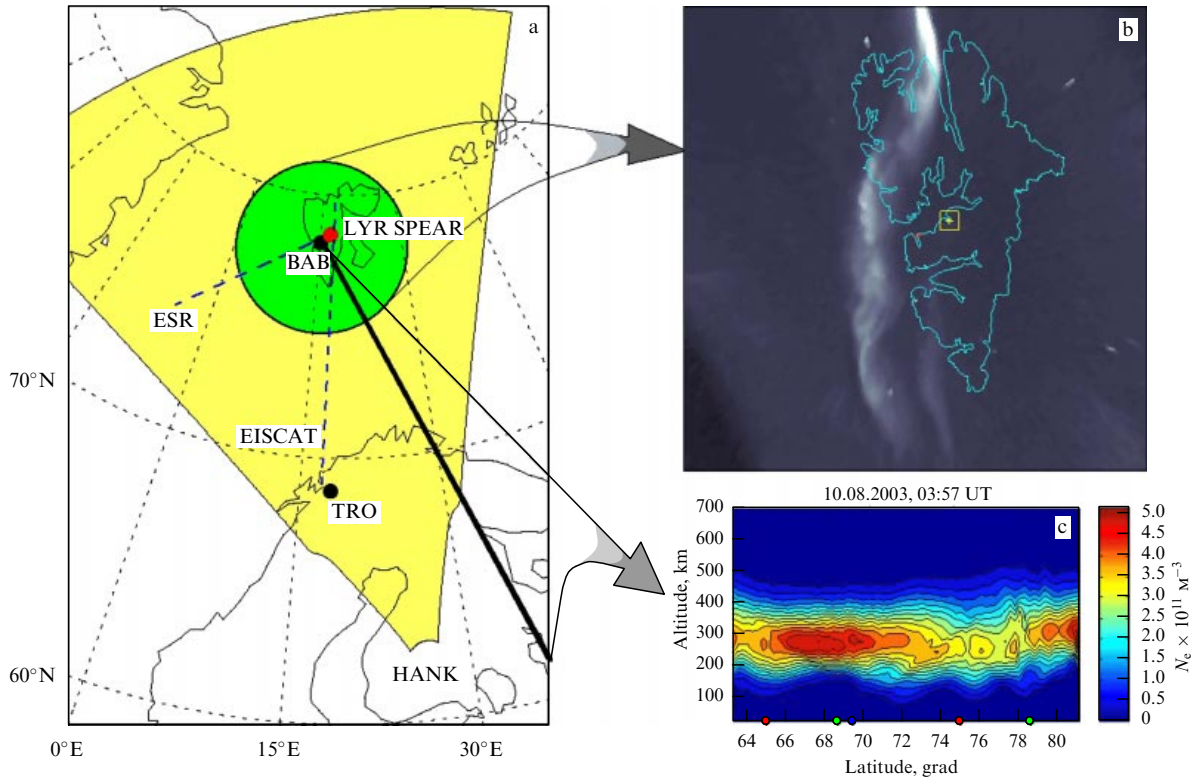

Figure 1. (a) The positions of the Barentsburg Observatory (BAB) and the SPEAR heating facility relative to the field of view of HANK, ESR, and EISCAT radars. The bold solid line shows the profile along which the points of the PGI tomographic chain are located. The circle corresponds to the field of view of the PGI TV camera. (b) The projected TV frame, with the square schematically showing the SPEAR heating facility. (c) An example of tomographic reconstruction of ionospheric disturbances; dots on the horizontal axis correspond to receiving points.

In the campaigns, both antennas of the ESR radar in Longyearbyen and the EISCAT radar in Tromsø are in operation. The movable ESR antenna that is oriented along the geomagnetic latitude or at a small angle to it measures the speed of plasma convection along the auroral arcs. The Tromsø radar antenna is tilted such that its beam crosses the vertical (or skewed, depending on the problem) beam of the ESR antenna at the height 120–150 km, and hence the measurements are within the field of view of the full sky observation camera in Barentsburg (Fig. 1a). In such experiments, an important role is played by the correct spatial matching of optical and radar measurements. With this aim, an exact positioning of a TV camera with respect to Earth is done with the help of a software package developed by Swedish colleagues (the so-called camera geometric calibration). As a result of the calibration procedure, each pixel of the image corresponds to a point on the ground with certain coordinates. After that, it is not difficult to match aurora images with radar and satellite measurements.

Solar wind interaction with the daytime magnetosphere is a continuous process; however, it appears especially clear during distinctive interplanetary medium parameter changes, such as an abrupt change of the IMF sign or a discontinuity in the solar wind pressure. Theoretically, energy and plasma influx into the magnetosphere are considered to occur at the time of reconnection of Earth's lines and those of the IMF. For the southern IMF, the reconnection occurs near the under solar point and the reconnected field lines are transported by solar wind through the polar cap to the tail, where their collection is interpreted as a magnetic energy increase. In this process, the number of closed field lines on the day side decreases, and the cusp is shifted to the lower-latitude region. For the northern IMF, the reconnection occurs behind the cusps. The solar wind plasma located on the field lines adjoining the magnetopause appears on the newly created closed field lines, which is interpreted as trapping of the transition layer plasma. An increase in the number of closed field lines in the daytime magnetosphere leads to a shift of the cusp toward the high latitudes.

The picture becomes more complex if we take the large-scale magnetospheric convection into account, which does not allow the field lines to 'accumulate' on the night side for the southern IMF, and transports the closed field line 'excess' from the day side to the night one for the northern IMF. The convection can also play a positive role. Because of the magnetic field frozen into plasma, the magnetospheric convection is reflected in large-scale motions of the ionospheric plasma. Therefore, the convection property of certain responses to IMF changes can be used as an additional information source in the studies of solar wind and magnetosphere interaction processes by ground means.

One of the most effective means for studying processes in the magnetopause and adjoining regions is, traditionally, the investigation of the structure and dynamics of the daytime aurora. In the above context, this is investigation of the auroral response to the change of the IMF sign. Theoretically, the solar wind interaction scheme looks understandable; but technical complications appear in attempting to investigate it experimentally. First, an abrupt change of the IMF sign typically occurs at the front of the solar wind inhomogeneity and is accompanied by a noticeable change in the plasma pressure. As a result, we see the combined effect of a field flip and a pressure jump in the auroras. Second, calculating the beginning time for the interaction of the

inhomogeneity with the magnetopause involves an uncertainty because of the inaccuracy of time calculation for the inhomogeneity propagation, since ACE (Advanced Composition Explorer) satellite data for measurements at the distance 250 R_E (R_E is Earth's radius) are typically used. The third difficulty appears because the source of the daytime aurora is near the daytime cusp or the polar cap boundary (see, e.g., [3]). The magnetosphere there consists of layers whose sizes are small when projected on the ionosphere; this makes it more difficult to associate the auroral source with a magnetospheric domain. A wrong association can lead to a wrong interpretation of observed optical phenomena.

Typical forms for daytime aurora are the so-called poleward-moving auroral forms (PMAFs). In pioneering work on the investigation of daytime auroras in Spitsbergen, a hypothesis was put forward that the reconnection can be the reason for PMAF-type auroral activity [4]. Further use of this hypothesis by a Norwegian research group that has a developed network of optical observations in Spitsbergen led to the conclusion that almost every case of near-midday PMAF is an ionospheric manifestation of reconnected field tubes that drift into the magnetospheric tail, even though the interpretation is ambiguous due to the above reasons. An alternative approach was attempted in Refs [5, 6], where cases were described where the structures were observed on closed field lines, and their dynamics were not due to convection only. That work demonstrated the importance of optical studies combined with other measurements and initiated the idea of regular collaboration campaigns in Spitsbergen.

A phenomenon that is described below was detected during one of the campaigns; it represents a unique situation in which the above difficulties were almost absent. First, it turned out that we were dealing with a response to IMF changes only. Second, we used data from the Geotail satellite, which is not far from the magnetopause. This allowed relating the PMAF to just the IMF twist to the north with a sufficient degree of confidence; this was later confirmed by the ionospheric convection pattern recovered on the basis of radar data. Third, not long before the beginning of the phenomenon, a satellite of the DMSP (Defence Meteorogical Satellites Program) series was above the aurora; according to its data, the forms were on closed field lines.

To interpret the results of optical observations, HANK radar data (part of the SuperDARN network) were invoked, as were the data of the Finnish network of interference magnetometers complemented by the PGI's magnetometer in Barentsburg. As a result of such a comprehensive approach in the analysis of the phenomenon, we concluded the following (see also [7]). After the twist of the IMF B_z component to the north, the HANK radar detected an ionospheric inhomogeneity over Spitsbergen as an anomalous reflected signal. The anomaly was accompanied by an activity burst in the Hz range, and in Barentsburg only, i.e., it was detected by the highest high-latitude induction magnetometer (Fig. 2a). The anomalous echo and the geomagnetic activity burst were due to the trapping of anisotropic plasma of the transition layer, as is schematically shown in Fig. 2b. Drifting along the boundary between the BPS (boundary plasma sheet) and the LLBL (low-latitude boundary layer), the plasma bunch caused LLBL widening and, as a consequence, a shift of the source of three auroral arcs that had existed before that (Fig. 3b).

This optical phenomenon seems to be a typical PMAF in a keogram (Fig. 3a). We note that the IMF variation had the shape of a short-time positive pulse. By using data from far ACE and Wind satellites, it is quite possible to relate PMAFs in time with the back side of the inhomogeneity, i.e., with the IMF turned to the south, because of a large calculation error of the inhomogeneity propagation time to the magnetopause and in the absence of additional radar data on the character of the ionospheric convection. The arc dynamics can then be explained by the drift of the reconnected field lines to the tail, and the anomalous echo in the Hank data and the burst of magnetic activity in Barentsburg can be related to the cusp shifting toward low latitudes. Therefore, our investigation is methodologically important for diagnostics of the magnetopause processes by ground-based means.

3. Investigation of the ionosphere over Spitsbergen by the active modification method

Currently, scientific progress as a whole not only is determined by the development of observational techniques but also depends significantly on international cooperation. Along with space weather research, another impressive example of the international approach to solutions of important geophysical problems in Spitsbergen is the polar ionosphere modification experiments by powerful SW radiation.

Active ionosphere modification, with the aim to investigate the properties of this natural plasma shell, has been used in geophysics since the 1980s. But in Spitsbergen, in the cusp and the polar cap region, the SPEAR heating facility began operations only in 2004. Artificial ionospheric radiation (AIR) — a broadband noise-like radiation appearing as a result of ionospheric plasma excitation by powerful electromagnetic radiation — was discovered in EISCAT (Tromsø) heating experiments [8]. Although the interest in spatial characteristics of this radiation has existed from the moment of its discovery, the AIR observations have long been restricted to measuring the signal intensity, separating the spectral components of the radiation, studying the radiation dynamics, and so on. Localization of the AIR generation region remained an unsolved problem for a long time because of the high requirements for the equipment.

The SW radio interferometric facility capable of determining the direction of an incoming signal by the phase difference method was constructed at the PGI in 2002–2003. The interferometer works in the 1.5–32 MHz frequency range, with the 300 kHz bandwidth and a wide dynamic range (about 100 dB). The facility allows conducting phase difference and amplitude measurements of artificial as well as natural signals.

In February–March 2007, the PGI took part in the ionosphere heating experiment in Spitsbergen. To date, we have acquired considerable experience, and our equipment has been tested at middle and auroral latitudes during the Sura and EISCAT heating experiments. In the polar cap region, such observations were unprecedented. Although the heating facility power was only two thirds of the projected one (the effective radiation power only slightly exceeded 10 MW), we were able to confidently record artificial ionospheric radiation [9].

Artificial ionospheric radiation is a weak noise-like signal in the frequency range $\approx 200-300$ kHz whose amplitude is 60 dB less than the amplitude of the heating facility wave reflected by the ionosphere. The radiation and properties of its spectral characteristics significantly depend on nonlinear

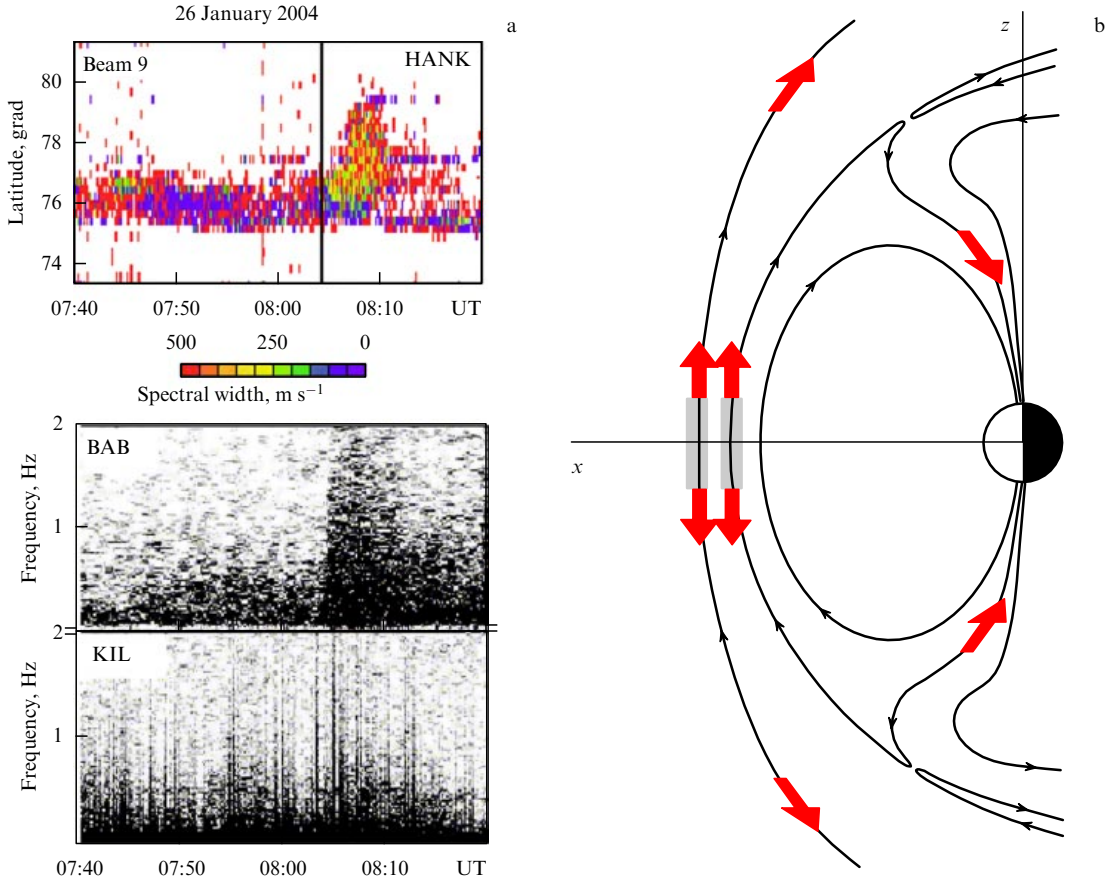

Figure 2. (a) The anomalous echo in the HANK radar data and wave activity in Barentsburg (BAB) and at the Kilpisjärvi (KIL) auroral station. (b) A scheme illustrating the 'trapping' of the solar wind anisotropic plasma (the grey area) and the appearance of Hz waves in the high-latitude ionosphere (bold arrows) in the reconnection process for the northern IMF.

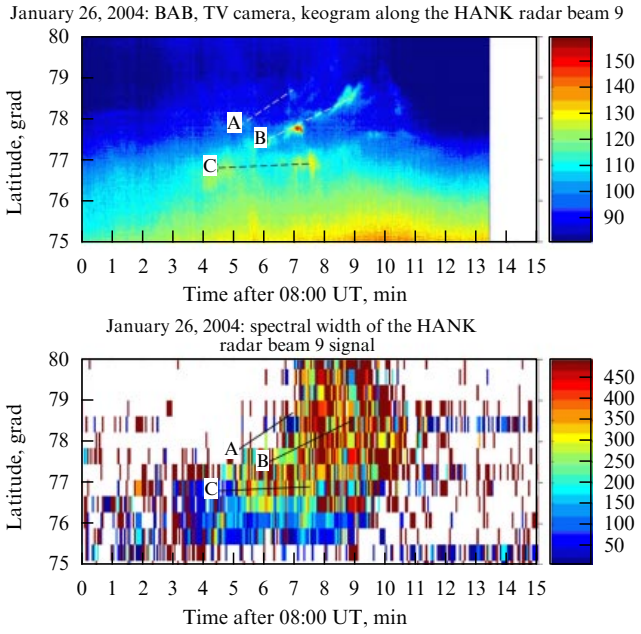

Figure 3. A keogram illustrating the dynamics of three auroral arcs, A, B, and C, along the ninth beam of the HANK radar (a), and the mutual motion of the arcs and the anomalous radar echo region (b).

processes excited in the ionospheric plasma as a result of heating, as well as on the value of the plasma frequency, the local gyrofrequency harmonic, and the orientation of geomagnetic field lines with respect to the heating facility.

As an example, Fig. 4a shows the spectrum of the artificial radiation recorded on March 9, 2007, for the heating frequency 4.45 MHz, the effective radiating power of the heating facility 13 MW, and radiation directed along the geomagnetic field lines. In this Figure, the characteristics of the artificial radiation stationary spectrum are clearly seen, such as the main downshifted maximum (DM) and its second harmonic 2DM, the broad continuum (BC) and broad upshifted maximum (BUM) signals in the region of negative and positive frequency shifts, respectively, as well as the upshifted maximum (UM) in the region of positive frequency shifts. The central part of the spectrum corresponding to heat waves reflected from the ionosphere is suppressed by a rejection filter set up at the intermediate frequency of the SW interferometer receiver.

The AIR registration by the PGI installation, which was incompletely integrated in Barentsburg at that time, demonstrated a possibility in principle of AIR generation by heating in the geophysical conditions of Spitsbergen. In its current modification, the facility is capable of not only recording the fact of AIR generation but also determining the direction to its source in the ionosphere (Fig. 4b), as was done in one of EISCAT heating facility experiments [10].

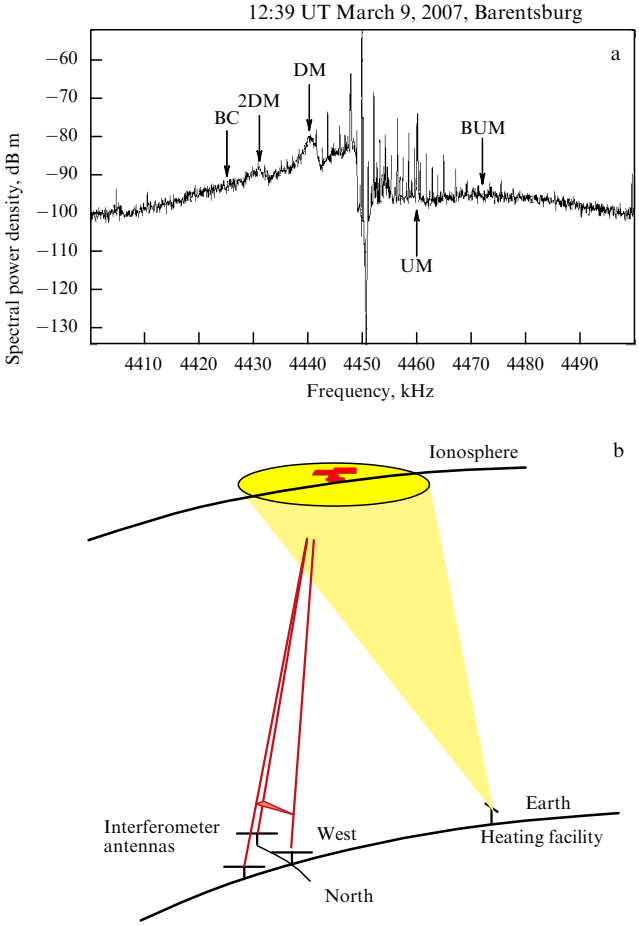

Figure 4. (a) The AIR spectral power density recorded at 12 : 39 UT on March 9, 2007 in the Barentsburg Observatory. (b) A scheme of the AIR source localization experiment by the PGI interferometer.

4. Characteristics of the high-latitude propagation of an artificial electromagnetic signal in the 0.1 – 10 Hz range

Wave propagation in various frequency ranges is studied by using theoretical (numerical) ionosphere models. Continuous improvement of the models, aiming to most adequately represent real situations, is important for applications. It is known that the spectrum of near-Earth background noise in the 0.1 – 10 Hz frequency range has a number of features related to the ionospheric structure. As is known from the theory [11], there are two reflecting ionospheric regions for a wave in the range from 0 to 10 Hz. The first reflecting region, where the electron concentration increases with increasing the height, is below the F-layer maximum, thus forming the Earth–lower ionosphere waveguide for such waves. The existence of the second reflecting region is due to a characteristic drop in the electron number density above the F-layer maximum. Together with the first region, this region forms the outer waveguide, the ionospheric Alfvén resonator (IAR). The interference of waves reflected from resonator walls leads to a nonmonotonic frequency dependence of their amplitudes and hence to the formation of so-called spectral resonance structures in the noise background. It is probable that IAR can also have a similar influence on signals of artificial origin in this frequency range.

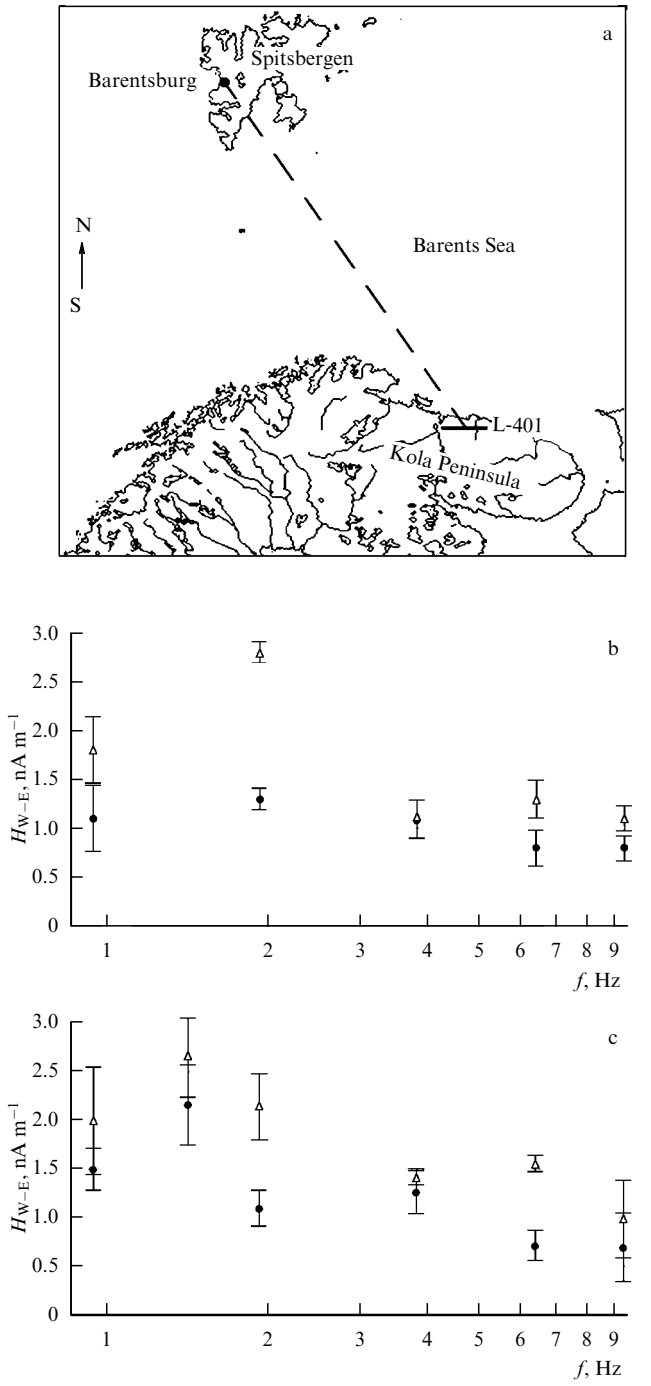

Figure 5. A scheme of ELF signal radiation and reception experiments (a), and results of signal amplitude measurements on September 5 and 6, 2007 (b) and on August 18 and 20, 2009 (c).

To check this hypothesis, a comprehensive experiment designed to generate and receive 0.1 – 200 Hz ELF electromagnetic radiation was conducted in September 2007. An L-401 transmission line 107 km in length, which was grounded at the ends, available in the northern part of the Kola Peninsula, and predominantly west–east oriented, was used as a radiating antenna (Fig. 5a). A quasimonochromatic current in the antenna was supported by an ELF transmitter with the power 100 kW. The radiation occurred at several frequencies in the 0.1 – 10 Hz range, and the current amplitude in this range was 150 – 180 A.

The magnetic field created by this antenna was measured at the distance 1200 km from the transmitter, in the Barentsburg Observatory, by a three-component induction magnetometer. The radiation experiments were conducted within a few days, mostly at night, when the IAR formation probability is high.

The main result of these experiments is that in a number of cases, a nonmonotonic dependence of the received signal on the frequency was detected for the horizontal magnetic field component (Fig. 5b, c). We believe that this is due to the IAR influence on the propagating signal, because the scheme of the experiment allowed investigating the field in the region with a significant contribution of the wave propagating in the outer waveguide (above the F-layer) to the total field.

We also estimated the effectiveness of various ionospheric models for interpretation of the results of the conducted measurements. We showed that the results of the international reference ionosphere (IRI) model calculations agree poorly with the experimental data. The upper atmosphere model (UAM) calculations better correspond to the experiment, but they are also imperfect. The results of experimental ionospheric studies (such as satellite tomography) should be used to refine the ionospheric characteristics obtained by model calculations.

5. The future of geophysical investigations in Spitsbergen

The future of geophysical investigations in Spitsbergen is seen, first, in increasing international cooperation. The times have passed when observations were made in isolation and only data from two or three instruments were used to analyze phenomena. Studies by Russian, Norwegian, Swedish, Finnish, and Chinese researchers clearly demonstrate the effectiveness of coordinated observations and a comprehensive approach to data analysis. Understanding that, in 2009 the Norwegian Research Council put forward an initiative to integrate the maximum possible number of observation points operating in Spitsbergen into a unified measurement–information system aimed at the global modeling of the Arctic atmosphere. This Svalbard Integrated Observing System (SIOS) project was financially supported by the European Union. The Polar Geophysical Institute is a member of the consortium running the preliminary stage of the project; it is part of a group researching the influence of magnetospheric processes on the Arctic climate.

References

1. Kunitsyn V E, Tereshchenko E D, Andreeva E S *Radiotomografiya Ionosfery* (Radiotomography of the Ionosphere) (Moscow: Fizmatlit, 2007)
2. Frolov V L et al. *Usp. Fiz. Nauk* **177** 330 (2007) [*Phys. Usp.* **50** 315 (2007)]
3. Sandholt P E et al. *J. Geophys. Res.* **103** (A10) 23325 (1998)
4. Vorobjev V G et al. *Planet. Space Sci.* **23** 269 (1975)
5. Kozlovsky A, Kangas J *J. Geophys. Res.* **107** (A2) 1017 (2002)
6. Kozlovsky A E et al. *Ann. Geophys.* **21** 2303 (2003)
7. Safargaleev V et al. *Ann. Geophys.* **26** 517 (2008)
8. Thidé B, Kopka H, Stubbe P *Phys. Rev. Lett.* **49** 1561 (1982)
9. Tereshchenko E D et al., in *VII Intern. Suzdal URSI Symp. "Modification of Ionosphere by Powerful Radio Waves," Book of Abstracts* (Moscow, 2007) p. 42
10. Tereshchenko E D et al. *Ann. Geophys.* **24** 1819 (2006)
11. Polyakov S V, Rappoport V O *Geomagn. Aeron.* **21** 610 (1981)

PACS numbers: **94.20.–y**, 94.50.Ci, **96.30.–t**
DOI: 10.3367/UFNe.0180.201005j.0542

Results of solar wind and planetary ionosphere research using radiophysical methods

N A Armand, Yu V Gulyaev, A L Gavrik, A I Efimov, S S Matyugov, A G Pavelyev, N A Savich, L N Samoznaev, V M Smirnov, O I Yakovlev

1. Introduction

We describe the results of space plasma studies using remote methods developed at the Kotelnikov Institute of Radioengineering and Electronics (IRE) of the Russian Academy of Sciences. The main result of circumsolar plasma research is the determination of the radial velocity dependence for the motion of plasma fluxes and solar wind turbulence modes at various distances from the Sun. Priority data on altitude profiles of Martian and Venusian night ionospheres have been obtained using the radio sensing method. Two monitoring methods for Earth's ionosphere have been suggested and realized. In the first method, ionospheric radio sensing is done on the spacecraft–Earth's surface point path. In the realization of the second method, two Earth satellites are used, one of which is the source of radio waves sounding the ionosphere, and the other is the receiver of plasma-modified signals.

The aim of this contribution is to briefly describe the main results of various space plasma studies done at the IRE, Department of Space Radiophysics, from 1970 to 2009. The work performed was devoted to investigations of solar wind and Martian and Venusian ionospheres, and to the development of new monitoring methods of Earth's ionosphere by using spacecraft signals. In Figure 1, dashed lines show the radio wave propagation paths from spacecraft to points on Earth's surface. For solar wind research, we used signals of Soviet (Mars-2 and Venera-10 (-15,-16)), European (Helios and Ulysses), and American (Galileo and MGS (Mars Global Surveyor)) spacecraft. It was possible to investigate the plasma shells of Mars and Venus after the Soviet Mars-2 and Venus-9 (-10) spacecraft were launched into the first artificial satellite orbits of these planets. The monitoring of Earth's ionosphere by a new radio sensing method was realized on satellite–satellite paths. For this, we have used radio links between the Mir Station and geostationary satellites, as well as between GPS (Global Positioning System) satellites and the research CHAMP (Challenging Minisatellite Payload) and FORMOSAT-3 satellites. At the first stage, the influence of various media on the amplitude, phase, frequency, and spectrum of decimeter radio waves was

N A Armand, Yu V Gulyaev, A L Gavrik, A I Efimov, S S Matyugov, A G Pavelyev, N A Savich, L N Samoznaev, V M Smirnov, O I Yakovlev
Kotelnikov Institute of Radioengineering and Electronics, Russian Academy of Sciences, Fryazino branch, Fryazino, Moscow region, Russian Federation
Email: efimov@ms.ire.rssi.ru

Uspekhi Fizicheskikh Nauk **180** (5) 542 – 548 (2010)
DOI: 10.3367/UFNr.0180.201005j.0542
Translated by S V Vladimirov; edited by A M Semikhatov

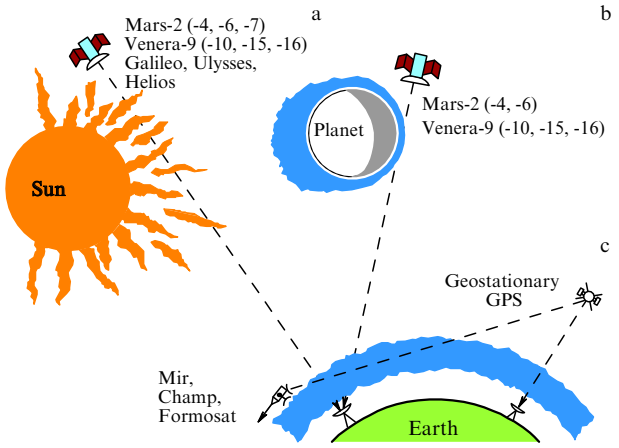

Figure 1. Scheme for radio sensing of circumsolar plasma (a), planetary ionospheres (b), and Earth's ionosphere (c).

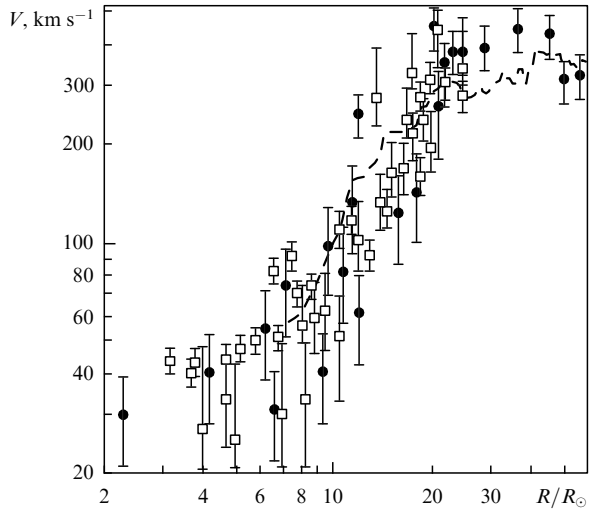

Figure 2. The solar wind velocity dependence on the heliocentric distance according to radio sounding data. Black dots correspond to Venera-10 data, 1976; squares, to Venera-15 (-16) data, 1984; the dashed line, to Galileo data, 1997.

studied. Results of this first stage are published in [1]. At the second stage, inverse problems were solved: the plasma parameters at various distances from the Sun or planetary surfaces were determined using radio data. This contribution describes the main results of the second stage of research.

2. Solar wind investigation

At the beginning of our studies, it had been known that solar wind plasma fluxes are strongly nonuniform and the speed of their motion near Earth is 300 – 400 km s^{-1}. The region of solar wind formation and acceleration, located at heliocentric distances in the range 2–40 solar radii R_0, was poorly investigated. In particular, the main theoretical difficulty was that the initial plasma energy near the Sun was insufficient for solar wind acceleration up to supersonic speeds.

First of all, it was necessary to obtain the experimental dependence of the solar wind velocity V on the heliocentric distance R, localize the transition from subsonic to supersonic flows of plasma streams, and find the region of sharp solar wind acceleration. We performed several long-term cycles of circumsolar and interplanetary plasma radio sounding using deep-space communication centers separated over large distances. Moving plasma inhomogeneities lead to correlated fluctuations of radio wave frequencies on diverse paths, which allows measuring the time delay of such fluctuations at one point compared to that at another point, and thus determining the solar wind velocity. Figure 2 shows the dependence of the solar wind velocity V on the heliocentric distance R in terms of the solar radius R_0, obtained in 1976 and 1984 by Venera-10 (-15, -16) spacecraft. The first experimental dependence $V(R)$ showed that the main plasma acceleration occurs over the distances $(8-20)R_0$. In the region $(7-12)R_0$, a transition from the subsonic to the supersonic state occurs, and at $R > 40R_0$, the velocity is stabilized at 300 – 400 km s^{-1}.

In 1996 – 1997, on the basis of Galileo spacecraft radio sensing data collected in collaboration with European researchers, the $V(R)$ dependence, shown in Fig. 2 by a dashed line, was also obtained. This result fully confirmed the accuracy of the above conclusions on the solar wind velocity regime in the region of its main acceleration.

It was proposed that the effect of rapid solar wind acceleration is due to intensive Alfvén waves arriving from the corona; these waves transfer additional energy to solar wind via dissipation. To confirm this hypothesis, the Alfvén waves needed to be detected in the corona and supercorona of the Sun. On the basis of the analysis of polarization angle variations (Faraday rotation) of linearly polarized radio waves sounding the plasma, and with the use of a correlation analysis procedure for the Faraday rotation fluctuations observed at points on Earth's surface separated by a long distance, it was established that intensive Alfvén waves indeed exist at distances $(4-10)R_0$ and move with velocities 400 – 1000 km s^{-1}.

Solar wind can be regarded as a statistically nonuniform medium, similar to a turbulent gas. In this approach, three characteristics are introduced into the theory: the index p of the power-law spatial spectrum of inhomogeneities, the minimum scale l, and the maximum external scale L_0. At small distances from the Sun ($R < 60\,R_0$), these characteristics can be determined by the radio sounding method only, by analyzing fluctuations of the radio wave phases, frequencies, and amplitudes. Figure 3 shows the experimental dependence of the spectral index p of the spatial inhomogeneity on the heliocentric distance. It follows from the presented data that for $R > 25\,R_0$, the medium is indeed similar to a turbulent gas, with $p \approx 3.7$ (this corresponds to the Kolmogorov spectrum), the index p monotonically decreases for $R < 18\,R_0$, and for distances $(4-6)R_0$, we have $p \approx 3$, which is characteristic of plasma waves. The black dots give the values of p obtained in the solar wind sounding by the Venera-15 (-16) spacecraft (1984). The low values of the spectral index in the region of small distances $R < 10\,R_0$ correspond to small-scale inhomogeneities. The dashed line in Fig. 3 characterizes the data obtained in 1997 experiments of solar wind radio sensing by signals from Jupiter's European satellite, Galileo; these experimental data were processed at the IRE and published in collaboration with the researchers who had performed the experiment.

The spatial spectrum of inhomogeneities is also described by two characteristic linear scales. The maximum scale L_0 is related to features of plasma emission from various regions of the solar low corona: it is proportional to the distance R. Near

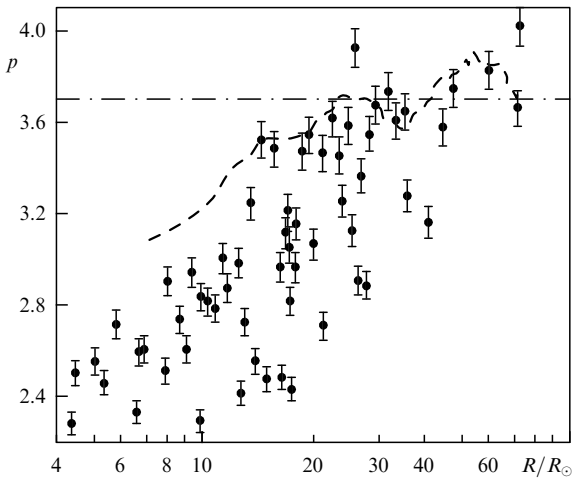

Figure 3. The spectral index of the spatial turbulence spectrum of solar plasma according to the radio sounding data by Venera-15 (-16) spacecraft, 1984 (black dots), and by Galileo spacecraft, 1997 (the dashed line).

the corona, the maximum scale is of the order of the Sun's radius. The minimum scale determines the characteristic sizes of the medium inhomogeneities at which energy is rapidly transferred from turbulence or wave phenomena into heat, i.e., plasma heating occurs. Apparently, the minimum scale l approximately corresponds to the proton gyroradius, and its value also increases with the distance from the Sun.

Thus, both characteristic scales in the solar wind inner regions increase approximately linearly with the increase in the heliocentric distance. The inertial interval width of the spectrum of plasma inhomogeneities, which occupies about four orders in magnitude, remains approximately the same at various distances from the Sun. However, processes responsible for the evolution of the index p for the external and internal scales are different.

The main results of solar wind investigations were obtained for the equatorial region of solar wind [2–12]. Recently, reliable data on solar wind emitted by high-latitude regions of the solar corona, where the plasma flow velocities are very large, were obtained by the radio sounding method.

3. Results of Martian and Venusian ionospheric studies

The investigation of ionospheres using the radio sounding method is possible when a spacecraft emitting radio signals immerges into or emerges from the planetary radio shadow, and the receiver on Earth records signals transformed by the planetary atmosphere. The radio sounding method uses a relation of the radio wave frequency and amplitude changes caused by the medium to the refraction angle, which is in turn related to the altitude profile of the ionosphere refractive index and hence to the electron concentration. To realize two-frequency radio sounding, centimeter- and decimeter-range transmitters ($\lambda_1 = 8$ cm and $\lambda_1 = 32$ cm) were installed on Mars-2 (-4) and Venera-9 (-10,-15,-16) spacecraft, and the reduced frequency difference and the amplitude variations of the mutually coherent signals were registered on Earth.

For the first time, a two-frequency radio sounding experiment was carried out to investigate the Martian ionosphere in 1971 when the Mars-2 spacecraft was covered by the planetary disk. The radio sounding was done on the sunlit side of the planet, the zenith angle Z_0 was 50° at the tangent point. As a result of data processing, the height distribution of the electron concentration $N(h)$ was obtained. The next experiment was conducted in 1974. In this case, the signals of the Mars-4 spacecraft sounded the evening-time ionosphere of Mars at $Z_O = 82°$. The concentration at the maximum was 5.9×10^4 cm^{-3} at the altitude 140 km, and the extent of the ionosphere was about 300 km high. When the Mars-4 spacecraft emerged from radio shadow, radio sounding of the dark side of Mars was done, by which the night-time ionosphere of this planet was detected for the first time. The ionization maximum appeared at the height 110 km, with the concentration $\approx 4.6 \times 10^3$ cm^{-3}, and the half-thickness of the main layer was about 35 km. Figure 4a shows the electron concentration profiles in the Martian ionosphere obtained by the radio sounding method for different conditions of solar illumination. On the daytime side, the ionosphere has the main maximum and lower maximum regions in which the concentration decreases with an increase in the zenith angle of the Sun. The plasma concentration and the height extent of the nighttime ionosphere are much less than those of the daytime one.

The experiments on multiple radio sounding of the Venusian ionosphere were conducted in October–December of 1975 using Venera-9 (-10) satellites. Data processing allowed determining 13 vertical profiles of the electron concentration in the daytime ionosphere and 22 distributions in the night-time one. The obtained results have a priority character, because data on the Venusian ionosphere had been quite scarce before these experiments with the Venus-9 (-10) satellites.

In 1983–1984, another major series of radio occultation experiments was conducted using the Venera-15 (-16) spacecraft: overall, 155 altitude profiles of the electron concentration $N(h)$ (73 profiles for the daytime ionosphere, 62 profiles for the night-time one, and 20 profiles for the terminator region) were obtained. The successful realization of multiple experiments allowed revealing the behavior patterns of the Venusian ionosphere under various illumination conditions. Figure 4b shows three distributions of the electron concentration characterizing the main properties of the daytime ionosphere of Venus. It was established that the concentration at the main ionization maximum naturally decreases with an increase in the solar zenith angle Z_O, from 5×10^5 cm^{-3} at $Z_O \approx 0$ to 2×10^4 cm^{-3} at $Z_O \approx 80° - 90°$. The height of the main maximum slightly depends on Z_O and is about 140 km. At the height 130–135 km, a regular presence of the lower ionization maximum was detected. A regular presence of the lower ionosphere at heights $h < 120$ km was discovered, with the additional maxima of the electron concentration. The distribution $N(h)$ in the upper ionosphere at heights $h > 200$ km is variable, the height of the upper ionosphere boundary tending to increase with increasing Z_O. At small Z_O (line *2*), it is about 270 km, and the upper boundary height increases (line *3*) with increasing Z_O.

Figure 4b also shows the electron concentration distributions in the night-time ionosphere of Venus that characterize its basic properties (curve *1*). The night-time ionosphere consists of one or two thin ionized layers of the half-thickness 5–10 km. The characteristic feature of the night-time ionosphere is its strong variability: the concen-

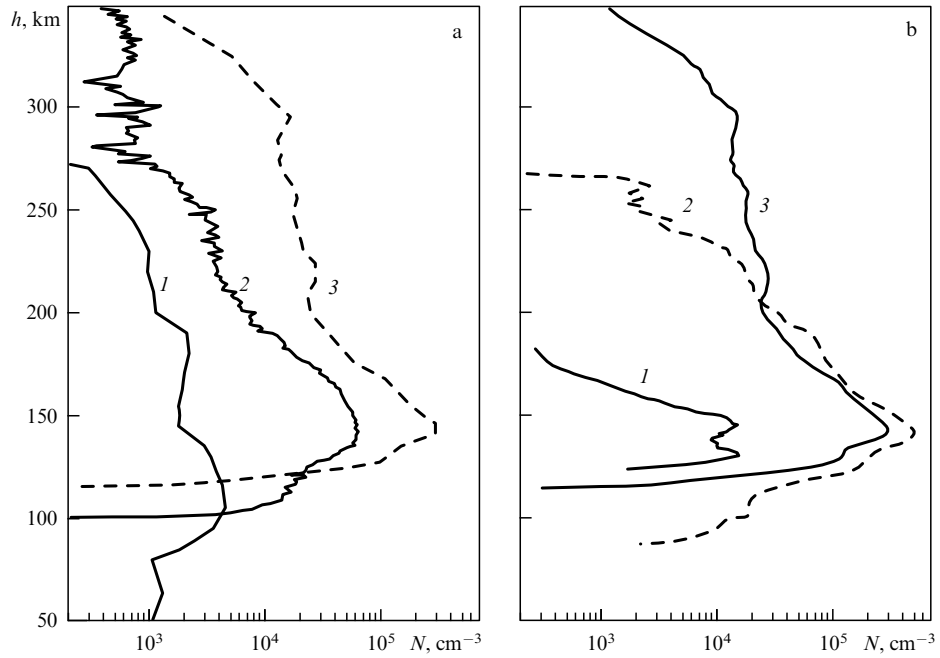

Figure 4. Examples of the electron concentration height distributions $N(h)$ in the Martian and Venusian ionospheres: (a) the distribution $N(h)$ for the night-time (*1*), evening time (*2*), and daytime (*3*) ionosphere of Mars; (b) the distribution $N(h)$ for the night-time ionosphere of Venus (*1*), for the ionosphere at a small zenith angle ($Z_O = 10°$) (*2*), and at a large zenith angle ($Z_O = 72°$) (*3*).

tration in the ionization maximum changes from 3×10^3 cm^{-3} to 2×10^4 cm^{-3}. The shape of the $N(h)$ profile also changes, as do its height extent, the half-thickness of the layers, and the heights of their maxima. The average height of the main ionization maximum is ≈ 140 km, and the values for the upper boundary height of the night-time ionosphere change in the range 140 – 250 km.

The electron concentration height profiles of the Martian and Venusian ionospheres obtained by the radio sounding method, as well as the local measurement data of the atmospheric gas composition, temperature, and ion composition in planetary neighborhoods, created a basis for the theory of ionosphere formation for Earth-group planets. Because the atmospheric gas composition for Mars and Venus is approximately identical, the ionospheric formation processes for these planets are also similar. The regions of the main and lower maximum in the daytime Martian and Venusian ionospheres are formed by photochemical processes, and molecular oxygen ions prevail there. In the upper ionosphere, the dominant role is played by the vertical diffusion of atomic oxygen ions and by the solar wind pressure. The night ionosphere of Venus is probably supported by two ionization sources: one of them is related to superthermal electron fluxes, and the other to the transport of atomic oxygen ions from the day side to the night side of the planet, with their subsequent diffusion downwards. The main results of the Martian and Venusian ionospheric research can be found in Refs [13 – 18].

The high accuracy of the two-frequency method allowed discovering the circumlunar plasma with the electron density 400 – 800 cm^{-3} by using the data of radio occultation experiments with the Luna-19 satellite [19], and discovering the plasma shell of Halley's comet with the electron density $10^3 - 3.6 \times 10^3$ cm^{-3} by using Vega-1 (-2) satellites [20, 21].

4. Development of methods to monitor Earth's ionosphere

We successfully developed two new methods for monitoring Earth's ionosphere. In the first method, the radio communication lines between GPS satellites and points on Earth's surface are used, and in the second one, radio sounding is carried out on a satellite–satellite path. The GPS and GLONASS (Global Navigating Satellite System) navigating systems provide a unique possibility to obtain data on the height distribution of the electron concentration in Earth's ionosphere via the radio translucence method with the use of navigating satellite–Earth point paths (the first method) for various helio- and geophysical conditions at any time in various regions on Earth. The measured parameters of radio signals (phase or delay time) contain information on the integrated characteristics of the medium through which the radio waves propagate. Determining the pseudorange difference, measured at two frequencies, is equivalent to determining the integrated electron concentration in the ionosphere. Variations of the measured ranges and distribution times (the phase or time delay) of radio signals are caused by variations of the radio wave refraction factors in space and time. This method is based on the dependence of the characteristics of received radio waves on the electron concentration distribution of the ionosphere. Mathematically, this dependence is described by a Fredholm integral equation of the first kind that has no analytic solution and requires elaboration of inversion methods for a class of ill-posed problems. The availability of high-speed computers allows using these methods for the inversion of observed data of radio signal parameters and for the prompt determination of the electron concentration height profile. The algorithm for the solution of such inverse problems, unstable by their nature, requires the use of special mathematical methods capable of incorpor-

ating additional information about the problem. Such information is given by models of the electron concentration distribution, for example, IRI (International Reference Ionosphere). Based on this model, we developed an effective solution method for the inverse problem of ionospheric radio translucence on a satellite–Earth path, using the relation between the parameters of sounding signals and the electron concentration height profile. This allowed developing the continuous monitoring technology intended to reconstruct the space and time structure of the ionosphere. The developed method can be used to recover the electron concentration height distribution of the ionosphere in the range of heights from 100 to 1000 km with the error ±0.02 NU (1 NU = 10^6 electrons in 1 cm^3). The electron concentration value at the height of the ionosphere maximum is determined up to ±0.014NU. The use of model assumptions about the ionosphere in the method developed by us leads to an essential decrease in the time needed to compute the determination of the electron concentration profile.

Figures 5a and 5b show examples of the obtained profiles $N(h)$ and, for comparison, the vertical sounding ionosonde data, together with computation results based on the IRI model. In using this method to determine the electron concentration in the ionosphere over a certain territory, it is possible to reveal the presence of peculiar features in the ionospheric plasma spatial distribution, because more than 10,000 altitude profiles of the electron density can be obtained for a site with a radius up to 1000 km from one Earth point within 24 hours. Examples of the profiles for one point are given in Fig. 5c. The radio translucence method allows finding the electron concentration distribution in the ionosphere in real time at any place on the globe by observations from a point located on Earth's surface, which is important for remote regions and those that are difficult to access [22–24]. This method can serve as an element in the global monitoring system of the Earth ionosphere.

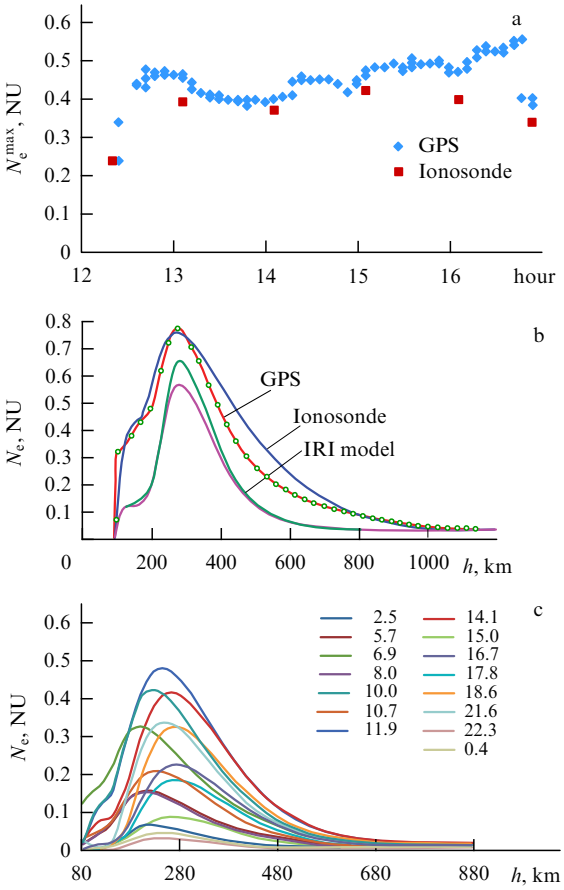

Figure 5. The electron concentration determined from GPS satellite observations, compared with ionosonde data.

For global ionosphere monitoring, a second method also turned out to be effective: radio occultation sounding using satellite–satellite paths. It was shown during the first radio occultation ionospheric experiments conducted on a path between the Mir orbital station and a geostationary satellite that this method gives detailed information on the electron concentration height profile in the lower ionosphere at heights 80–150 km. Signals from GPS satellites received by low-orbiting CHAMP and FORMOSAT-3 spacecraft were used for extensive radio sounding of the lower ionosphere across all regions on Earth at various solar illumination and activity. The ionosphere sounding data on satellite–satellite paths were processed in collaboration with researchers from the Geophysical Center in Germany and the Center for Space and Remote Sensing Research in Taiwan. Sporadic ionospheric formations at heights 85–120 km are especially clear in the radio data. Variations of the radio wave phase and amplitude accurately trace features of the electron concentration height profiles of E_s-structures, and it is therefore possible to determine the upper and lower boundaries of these structures with an error not exceeding ±1 km. Detailed statistical data on the probability of the occurrence of E_s-structures in the equatorial, mid-latitude, and polar regions in daytime and night-time conditions were obtained. By this method, amplitude and phase radio wave fluctuations caused by small-scale plasma inhomogeneity in the F-layer were investigated. The intensity and spectrum of the inhomogeneities are changed under the action of solar wind shock waves. There is a stable connection between two events — the solar wind shock wave arrival on Earth and the occurrence of sporadic formations in the lower night-time polar ionosphere with an increased electron concentration and increased intensity of a small-scale plasma inhomogeneity in the F-layer. The radio sounding method on satellite–satellite paths allowed relating the following phenomena: the solar wind shock wave arrival ⇒ proton and electron precipitation from the radiation belt ⇒ excitation of a small-scale plasma inhomogeneity in the F-layer of the ionosphere ⇒ appearance of intensive E_s-structures in the polar ionosphere. It is known that the occurrence of E_s-structures can be caused by different factors. The radio occultation sounding method confirmed the known fact that the probability of the occurrence of E_s-structures in the equatorial regions is independent of solar activity. According to our data, thin E_s-structures are often observed in these regions during both daytime and night-time, and their parameters do not change, even after the arrival of solar wind shock waves of the highest intensity.

Currently, due to the efforts of American, Taiwanese, and German researchers, an international system of radio occultation monitoring of the atmosphere and ionosphere is being formed that provides more than 2500 radio sounding sessions of Earth's atmosphere and ionosphere every day. At our institute, a radio occultation database has been created and is being continuously replenished. This requires elaboration of an automated processing of primary data methods. In the analysis of E_s-structures, the criterion for the appearance of intensive sporadic structures was formulated, which

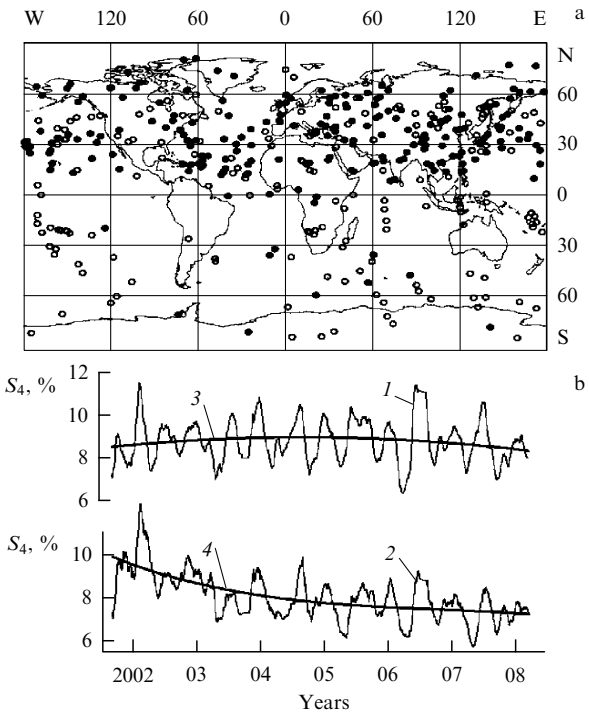

Figure 6. (a) The global distribution of intensive sporadic layers E_s according to FORMOSAT-3 satellites with the factor $S_4 > 0.12$, on June 1, 11, and 12, 2006. Black dots correspond to daytime events, circles to night-time events. (b) Time dependence of the average coefficient S_4 in the period from 2001 to 2008 according to the CHAMP data.

allowed obtaining maps of the geographic distribution of such formations.

Figure 6a shows the distribution chart for intensive sporadic E_s layers obtained according to FORMOSAT-3 satellites during the solar activity minimum for observations on June 1, 11, and 12, 2006. The chart shows an appreciable concentration of intensive sporadic layers at mid-latitudes of Earth's northern hemisphere, where the Sun's height over the horizon is maximal in June and, accordingly, the ionosphere ionization level by UV radiation is also maximal. The night-time sporadic layers are distributed over the globe more uniformly, which points to a different mechanism of their occurrence. The analysis of materials using a large-scale database including about 500,000 radio sounding sessions and created with the aid of the CHAMP satellite during 2001 – 2008 allowed obtaining information on long-term changes in the average coefficient S_4 that characterizes the fluctuation level of sounding signals. The value of the S_4 coefficient for each radio occultation session was determined as an average for the relative variations of the signal intensity, when the height h of the beam perigee exceeded 40 km, where the ionospheric influence prevails over the atmospheric influence. On average, about 200 values of S_4 were obtained within 24 hours for various regions of the globe. The data obtained in the measurement sessions were averaged over the time interval of 27 days and grouped according to latitude zones of Earth. Figure 6b shows the analysis results fot the S_4 coefficient variations in the latitude zone (lower than 55°, lines *1* and *3*), and in the polar regions (latitude higher than 55°, lines *2* and *4*). The smooth lines *3* and *4* correspond to the experimental data approximation by the method of least squares. Variations of the S_4 coefficient correlate among themselves in different geographical zones, pointing to a common mechanism of their origin, related to the effect of solar UV radiation on ionosphere ionization. The slow trend in S_4 depends on the geographical position of the measurement region. In polar regions, S_4 gradually decreases from 10% to 7% from 2001 to 2008, whereas in other regions, its value remains almost constant ($\approx 8.8\%$). The difference in slow changes of S_4 in the specified regions is apparently related to different ionization mechanisms. In the polar regions, an ionization decrease related to a reduced intensity of the solar wind influence on the ionosphere on the descending branch of solar activity is possible. In other regions, the ionization mechanism due to UV radiation of the Sun prevaile. From an analysis of long-term changes in the scintillation coefficient for radio waves sounding the ionosphere, it follows that radio signal scintillations in the high-latitude ionosphere are more sensitive to solar activity changes. The analysis also showed that it is important to study the characteristics of the signal amplitude variations of GPS satellites for investigation of the interrelation mechanism between solar activity and processes in the ionosphere and mesosphere.

The creation, realization, and development of the radio occultation monitoring method for Earth's ionosphere is described in our parers [25 – 33].

5. Conclusion

Simultaneously with foreign researchers, we suggested, realized, developed, and are improving the radio sounding method for studying plasma media of space origin: circumsolar and interplanetary plasma, the ionospheres of Mars, Venus, and Earth, and plasma shells of the Moon and comets. The difficult path of this research is partially described in Refs [1 – 33]. This problem could not be fully solved until the corresponding space-borne and ground-based means were created: long-lived spacecraft equipped with powerful, highly stable sources of radio sounding of space media, high-sensitivity systems of receiving and recording sounding signals, and high-speed information processing systems. The potential for improvement in each of these areas have not been exhausted yet and, consequently, further achievements of new interesting results in the field of Solar System research by radiophysical methods should be expected.

Advances in the development of space radiophysics at the Institute of Radioengineering and Electronics (now named after V A Kotelnikov) are linked to active support from Academician V A Kotelnikov and Professor M A Kolosov, and from numerous experts of industrial organizations that provided spacecraft launches into orbits, and the recording of signals emitted by them at deep-space communication centers.

References

1. Yakovlev O I *Kosmicheskaya Radiofizika* (Space Radiophysics) (Moscow: RFFI, 1998)
2. Yakovlev O I et al. *Astron. Zh.* **57** 790 (1980) [*Sov. Astron.* **24** 454 (1980)]
3. Efimov A I et al. *Radiotech. Elektron.* **26** 311 (1981)
4. Kolosov M A et al. *Radio Sci.* **17** 664 (1982)
5. Rubtsov S N, Yakovlev O I, Efimov A I *Kosmich. Issled.* **25** 620 (1987)
6. Yakovlev O I, Efimov A I, Rubtsov S N *Astron. Zh.* **65** 1290 (1988) [*Sov. Astron.* **32** 672 (1988)]
7. Yakovlev O I, Shishkov V I, Chashei I V *Pis'ma Astron. Zh.* **16** 163 (1990) [*Sov. Astron. Lett.* **16** 70 (1990)]

8. Efimov A I et al. *Astron. Zh.* **70** 1075 (1993) [*Astron. Rep.* **37** 542 (1993)]
9. Efimov A I et al. *Adv. Space Res.* **14** 93 (1994)
10. Efimov A I et al. *Pis'ma Astron. Zh.* **26** 630 (2000) [*Astron. Lett.* **26** 544 (2000)]
11. Efimov A I et al. *Radiotekh. Elektron.* **54** 773 (2009) [*J. Commun. Technol. Electron.* **54** 733 (2009)]
12. Efimov A I et al. *Astron. Zh.* **79** 640 (2002) [*Astron. Rep.* **46** 579 (2002)]
13. Kolosov M A et al. *Radiotech. Elektron.* **18** 2009 (1973)
14. Alexandrov Yu N et al. *Kosmich. Issled.* **14** 824 (1976)
15. Vasil'ev M B et al. *Dokl. Akad. Nauk SSSR* **218** 1298 (1974) [*Sov. Phys. Dokl.* **19** 629 (1975)]
16. Savich N A et al. *Radiotech. Elektron.* **31** 433 (1986)
17. Savich N A et al. *Radiotech. Elektron.* **31** 2113 (1986)
18. Gavrik A L, Gavrik Yu A, Samaznaev L N *Radiotekh. Elektron.* **53** 1104 (2008) [*J. Commun. Technol. Electron.* **53** 1044 (2008)]
19. Vasil'ev M B et al. *Dokl. Akad. Nauk SSSR* **212** 67 (1973) [*Sov. Phys. Dokl.* **18** 566 (1974)]
20. Savich N A et al. *Pis'ma Astron. Zh.* **12** 675 (1986) [*Sov. Astron. Lett.* **12** 283 (1986)]
21. Andreev V E, Gavrilik A L *Pis'ma Astron. Zh.* **19** 1081 (1993) [*Astron. Lett.* **19** 437 (1993)]
22. Andrianov V A, Smirnov V M *Radiotech. Elektron.* **38** 1326 (1993)
23. Smirnov V M *Radiotekh. Electron.* **46** 47 (2001) [*J. Commun. Technol. Electron.* **46** 41 (2001)]
24. Smirnov V M et al. *Radiotekh. Electron.* **53** 1112 (2008) [*J. Commun. Technol. Electron.* **53** 1052 (2008)]
25. Kucheryavenkov A I, Yakovlev O I, Kucheryavenkova I L, Samaznaev L N *Radiotekh. Electron.* **43** 945 (1998) [*J. Commun. Technol. Electron.* **43** 880 (1998)]
26. Pavelyev A et al. *Radio Sci.* **37** 1043 (2002)
27. Pavelyev A G et al. *J. Geophys. Res.* **112** A06326 (2007)
28. Pavelyev A G, Wickert J, Lion Y *Izv. Vyssh. Uchebn. Zaved. Radiofiz.* **51** 1 (2008) [*Radiophys. Quantum Electron.* **51** 1 (2008)]
29. Pavelyev A G et al. *Geophys. Res. Lett.* **36** L21807 (2009)
30. Pavelyev A G, Matyugov S S, Yakovlev O I *Radiotekh. Elektron.* **53** 1081 (2008) [*J. Commun. Technol. Electron.* **53** 1021 (2008)]
31. Yakovlev A G, Matyugov S S, Anufriev V A *Izv. Vyssh. Uchebn. Zaved. Radiofiz.* **52** 181 (2009) [*Radiophys. Quantum Electron.* **52** 165 (2009)]
32. Yakovlev O I, Wickert J, Anufriev V A *Dokl. Ross. Akad. Nauk* **427** 624 (2009) [*Dokl. Phys.* **54** 363 (2009)]
33. Yakovlev O I et al. *Acta Astronaut.* **63** 1350 (2008)

PACS numbers: 41.20.Jb, **94.20.–y**, **94.80.+g**
DOI: 10.3367/UFNe.0180.201005k.0548

Satellite radio probing and radio tomography of the ionosphere

V E Kunitsyn, E D Tereshchenko,
E S Andreeva, I A Nesterov

1. Introduction

Investigations of ionospheric spatial plasma distributions are necessary in order to study the ionosphere and the physics of its processes. The ionosphere, as a medium for radio wave propagation, essentially influences the operation of various navigation, positioning, and communication systems. Therefore, investigations of the ionosphere structure are of interest for many geophysical and radiophysical applications. The existing radars and ionosondes allow only local diagnostics of the ionosphere. The creation of a sufficiently dense network of traditional means of ionospheric sounding is quite difficult and expensive. Low-orbit (like the Russian Cicada and the American Transit systems) and high-orbit (GPS/GLONASS) satellite navigation systems and the network of receivers on Earth's surface allow conducting ionosphere sounding in various directions and using tomographic methods, i.e., allow revealing the spatial structure of the ionospheric electron concentration. Currently, satellite radio tomography (RT) methods for the ionosphere are being successfully developed [1–7]. Since the early 1990s, RT systems have been operating on the basis of low-orbit (LO) navigation systems. Recently, there have been active RT studies based on the data of high-orbit (HO) navigation systems [6, 7]. To identify the different RT types, the terms 'Low-Orbit RT' and 'High-Orbit RT' are used here (LORT and HORT).

V E Kunitsyn, E S Andreeva, I A Nesterov Lomonosov Moscow State University, Physics Faculty, Moscow, Russian Federation
E-mail: kunitsyn@phys.msu.ru
E D Tereschenko Polar Geophysical Institute, Kola Scientific Center, Russian Academy of Sciences, Murmansk, Russian Federation

Uspekhi Fizicheskikh Nauk **180** (5) 548–553 (2010)
DOI: 10.3367/UFNr.0180.201005k.0548
Translated by S V Vladimirov; edited by A M Semikhatov

2. Low-orbit radio tomography of the ionosphere

Low-orbit navigation systems, having an almost circular orbit at the height about 1000–1150 km, and ground-based receiver chains give the opportunity to obtain series of RT data over various rays. In RT experiments, the reception of two coherent satellite signals at frequencies 150 and 400 MHz and recording of the phase difference between them (the reduced phase) is carried out on a network of several ground-based receiving stations located along a trajectory of satellites at distances of a few hundred kilometers. Measurements of the reduced phase φ at the receiving points are the data for the RT reconstruction. Integrals of the electron concentration N over the rays between a ground-based receiver and a satellite transmitter are proportional to the absolute (total) phase Φ [1, 2] that includes the unknown initial phase φ_0,

$$\alpha\lambda r_e \int N \, d\sigma = \Phi = \varphi_0 + \varphi \,, \tag{1}$$

where λ is the sounding wave length, $d\sigma$ is the ray length element, r_e is the classical electron radius, and the proportionality coefficient α (of the order of unity) is determined by the selection of sounding frequencies.

We rewrite Eqn (1) in the operational form [4], taking a typical noncorrelated experimental noise ξ into account:

$$PN = \Phi + \xi \,. \tag{2}$$

Here, P is the projection operator transforming the two-dimensional distribution N into a set of one-dimensional projections Φ. The problem of tomographic reconstruction thus amounts to finding a solution of the set of linear integral equations (2) and finding the electron concentration N. One of the possible variants is discretization (approximation) of the projection operator P. We then obtain a corresponding set of linear equations with a discrete operator L:

$$LN = \Phi + \xi + E \,, \qquad E = LN - PN \,, \tag{3}$$

where E is the approximation error depending on the solution N. We note that Eqns (2) and (3) are equivalent if the approximation error is known. But in the data reconstruction of a real RT experiment, E is unknown and another

system of linear equations is actually solved:

$$LN = \Phi + \xi\,. \tag{4}$$

System (4) is not equivalent to (3). In other words, the difference between the solutions of (3) and (4) is determined by a different quasinoise component ξ and by a correlated (in time and rays) approximation error E. To solve (4), the absolute phase Φ should be known together with φ_0. Estimation errors of φ_0 for different receivers can lead to contradictions and inconsistencies in data and, as a result, to poor quality of the RT reconstruction. Therefore, a phase difference RT method, or an RT of the difference of linear integrals on close rays [8], was developed that does not require finding the initial phase φ_0. The system of linear equations for the phase difference RT is determined by the corresponding difference:

$$AN = LN - L'N = \Phi - \Phi' = D + \xi\,, \tag{5}$$

where $LN = \Phi$ is the initial linear system, $L'N = \Phi'$ is the linear system formed in the set of close rays, and D is the difference in integrals (1) for close rays.

There are numerous direct and iterative algorithms to solve the systems of linear equations in (4) and (5). Currently, iterative algorithms are most often used for ionospheric RT ray problems, but noniterative algorithms are also used: the singular decomposition method and its modifications, regularization methods of root-mean-square deviation, orthogonal decomposition, maximum entropy, quadratic programming and its various versions, the Bayesian approach, and so on [3 – 7]. In the process of modeling and carrying out numerous experimental LORT reconstructions, effective combinations of various methods and algorithms have been found that provide the highest-quality reconstructions.

The phase difference LORT gives considerably better results and has a higher sensitivity in comparison with phase methods, which is confirmed by modeling results and experimental data [4, 7, 9]. The resolution in the LORT problem in the linear formulation is 20 – 30 km horizontally and 30 – 40 km vertically. If we take the refraction of sounding rays into account, the spatial resolution of the ionospheric LORT method can be improved up to 10 – 20 km [7].

The world's first LORT reconstructions were obtained during March–April 1990, by researchers from Moscow State University and the Polar Geophysical Institute (PGI) of the Kola Scientific Center, Russian Academy of Sciences [10]. As an example, Fig. 1 shows, in geographical latitude–altitude coordinates (in kilometers), one of the first RT sections of the ionosphere obtained, the ionospheric RT section (in units of 10^{12} m^{-3}) between Moscow and Murmansk with a well visible ionization trough at the latitudes 63° – 65° containing a local extremum inside. Numerous subsequent experiments showed the complexity and the structural and dynamical variety of the trough [1 – 7]. Later, in 1992, preliminary results of the RT reconstruction of the ionosphere were obtained by foreign colleagues [11]. In 1994, experiments began on the Moscow–Arkhangelsk RT system created by the Pushkov Institute of Terrestrial Magnetism, Ionosphere and Radio Wave Propagation, Russian Academy of Sciences (IZMIRAN) [12].

Studies on the ionosphere LORT and its applications attract appreciable interest throughout the world, with more than ten scientific groups in leading countries currently working in this area [3 – 7]. Within the last twenty years, series of successful LORT experiments [3 – 7] were conducted

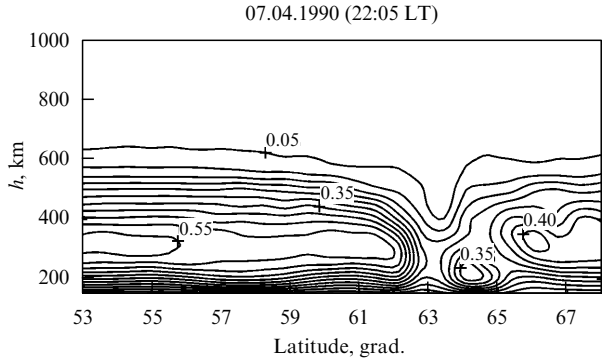

Figure 1. An example of one of the first LORT reconstructions of the ionospheric electron density (Moscow–Murmansk) in units of 10^{12} m^{-3} according to the data of April 7, 1990, 22 : 05 LT (local time).

in various regions of Europe, America, and Southeast Asia that demonstrated the wide opportunities of RT methods for the investigations of various ionospheric structures.

In RT cross sections in various regions, the known wave structures such as traveling ionospheric disturbances (TIDs) [3 – 7] were repeatedly observed. As an example, Fig. 2 presents the ionospheric RT reconstruction in which TIDs are clearly seen with the characteristic tilt angle about 45°, revealed over the Moscow–Arkhangelsk chain [12].

In the process of RT experiments in Southeast Asia on the low-latitude Manila–Shanghai chain, a number of structural features of the equatorial anomaly (EA) were revealed: the orientation of the formed EA 'core' (a region of the electron concentration close to the maximum level) at midday along Earth's magnetic field direction, an essential asymmetry of EA borders, and characteristic alternations of 'expansion and contraction' of the ionospheric F-layer [13 – 15]. The observable stable EA structural features can be interpreted by analyzing plasma fluxes and velocities in the EA region caused by the so-called fountain effect [7]. Reconstructing the ionospheric E-layer structure by RT methods is much more difficult, because the E-layer contribution to registered data is much smaller than the F-layer contribution. But if the RT system size allows the formation of a system of intersecting rays in the ionospheric F- and E-layers, it is possible to reconstruct the E-layer structure [16]. An example of the RT reconstruction of the F- and E-layer EA structures is given in Fig. 3. Terrestrial magnetic field lines are shown by dashed lines. The formed EA core is oriented along the direction of

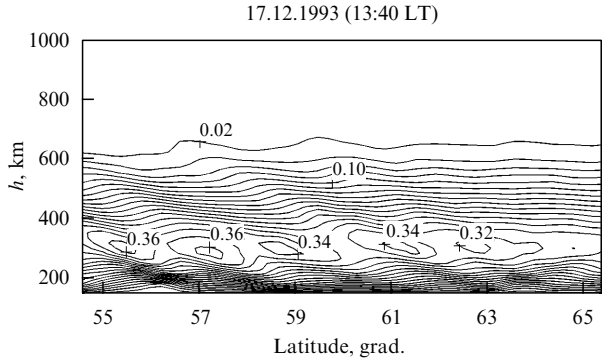

Figure 2. LORT reconstruction of traveling ionospheric disturbances (Moscow–Arkhangelsk) in units of 10^{12} m^{-3} according to the data of December 17, 1993, 13 : 40 LT.

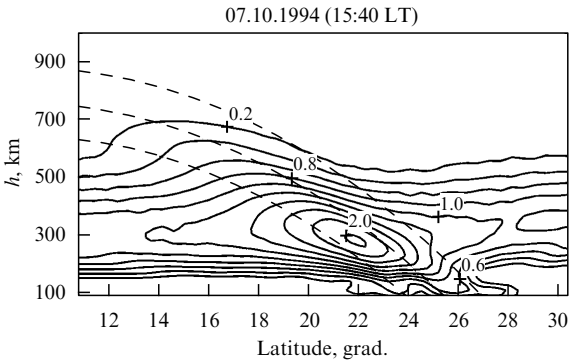

Figure 3. LORT reconstruction of the equatorial anomaly (Manila–Shanghai) in units of 10^{12} m^{-3} according to the data of October 7, 1994, 15 : 40 LT. Terrestrial magnetic field lines are shown by dashed lines.

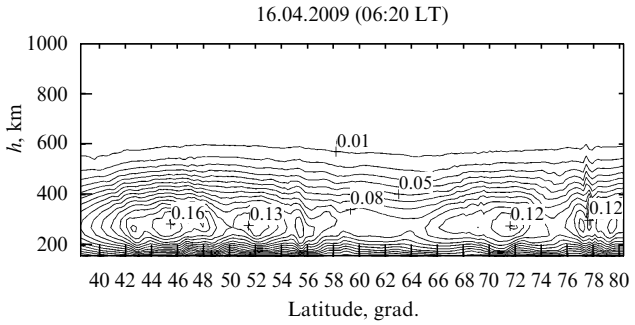

Figure 4. LORT reconstruction of the ionospheric electron density (Sochi — the Spitsbergen archipelago) in units of 10^{12} m^{-3} according to the data of April 16, 2009, 06 : 20 LT.

Earth's magnetic field; the asymmetry of the EA crest borders and the F-layer thickness variations are clearly seen. The 'forcing through' the F-layer bottom edge by the plasma flux along the field line is also observed, i.e., the plasma flow penetration from the F-layer into the lower layers of the E-region in the latitude range $24° - 26°$. In the region behind the EA core ($\approx 28° - 31°$), a constriction is formed.

In a series of experiments, the testing of ionospheric LORT and comparison of LORT reconstruction results with the incoherent scattering radar and ionosonde data [3 – 7] were done. One of the first such experiments was the 1993 autumnal Russian–American tomographic experiment (RATE'93), comparing the results of the ionospheric LORT cross sections with the incoherent scattering radar data in Millstone Hill (USA). The RATE'93 results demonstrated the high quality of LORT reconstructions and the agreement of results for radar LORT cross sections within the accuracy of both methods [17]. Similarly, the coincidence of the ionosonde and LORT data should be ascertained considering the restrictions of both methods [3 – 7, 14].

Currently, there are about ten operating chains (networks) of LORT receivers in various regions of the world (Russia, USA, Great Britain, Scandinavia and Finland, Alaska, Greenland, the Caribbean [2 – 7, 17 – 19]) that are actively used for research purposes. A LORT system has been created in India, and the LORT system in Southeast Asia is being updated. The Russian transcontinental RT system (Sochi — the Spitsbergen archipelago) consisting of nine receiving stations is the world's longest (about 4000 km) and has no analogues [20]. The uniqueness of the Russian LORT system is that the observation data cover the ionospheric region from auroral (polar cap zones) to low latitudes. This allows exploring the transfer of disturbances between the auroral, subauroral, and low-latitude ionospheres and studying the ionospheric plasma structure in various regions depending on various helio–geophysical conditions. As an example, Fig. 4 shows the ionospheric LORT cross section between Sochi and Spitsbergen for quiet geomagnetic conditions (the geomagnetic activity index $Kp < 1$). Around Spitsbergen ($78° - 79°$), quasiwave perturbations on the scale of the order of 50 km are detected. In the central reconstruction region ($59° - 65°$), the decrease in the electron concentration is appreciable. In the south of the RT cross section ($42° - 55°$), quasiwave structures on the scale of the order of 100 – 150 km are clearly seen, i.e., a complex ionospheric plasma structure is observed even in quiet conditions.

LORT allows not only revealing ionospheric inhomogeneities of a natural origin but also detecting ionospheric disturbances generated by anthropogenic sources, in particular, disturbances caused by rocket launches [7, 21, 22], industrial explosions [23], and powerful HF radiation [24 – 26]. For example, LORT allows the reconstruction of 'instantaneous' (10 – 15 min) two-dimensional cross sections of the electron concentration in the ionosphere. The time span between LORT reconstructions depends on the number of operating satellites and currently varies between 30 and 120 min. The LORT method also allows determining plasma fluxes by analyzing time-successive RT cross sections of the ionosphere [27]. If several receiving chains spaced by several hundred kilometers are available, then the three-dimensional structure of the ionosphere can be reconstructed. An essential limitation of the LORT technique is the necessity of constructing systems with many receiving chains.

3. High-orbit radio tomography of the ionosphere

With the development of global navigation systems in the USA and Russia (GPS, Global Positioning System and GLONASS, Global Navigation Satellite System), it has become possible to conduct continuous measurements of characteristics of ionosphere-propagating radio signals and to solve the inverse radio sounding problems [6, 7]. In the coming years, the development of other systems, in particular, the European (Galileo) and Chinese ones, is planned. We use the standard abbreviation GNSS (Global Navigation Satellite System) for all types of global navigation systems. Currently, the information constantly obtained by networks of GNSS receivers allows formulating the reconstruction problems for ionospheric electronic density distributions. There is a series of regional and global networks of GNSS receivers, in particular, the IGS (International Geodetic Service) network, totaling more than 1,500 receivers. The main feature of the inverse radio sounding problems based on GNSS data, related to the type of tomographic problems with incomplete data, is their high dimensionality. The comparatively low angular velocity of high-orbit GNSS satellites requires taking the temporal variability of the ionosphere into account, which leads to the formulation of a four-dimensional (three spatial coordinates and time) tomographic problem. Because of the four-dimensional character of the problem, the incompleteness of initial data becomes an

essential issue; the satellite–receiver rays do not propagate through all points of space and in zones with a small number of receivers, regions of data absence appear that require the elaboration of special approaches [28].

For the purposes of ionospheric sounding, the measured phase values of radio signals propagating from a satellite to a ground-based receiver for two coherent and multiple operating frequencies are used. For example, for a GPS system, these are the frequencies $f_1 = 1575.42$ MHz and $f_2 = 1227.60$ MHz. The corresponding data — the phase paths of radio signals measured at the wavelengths of the sounding waves — are usually denoted by L_1 and L_2. In addition, the pseudo ranges P_1 and P_2 (group paths of radio signals) measured according to the propagation time for wave trains at frequencies f_1 and f_2, can be used. The phase data L_1 and L_2 allow calculating the total electron content (TEC) — the integral along the ray connecting the transmitter and the receiver:

$$\mathrm{TEC} = \left(\frac{L_1}{f_1} - \frac{L_2}{f_2}\right) \frac{f_1^2 f_2^2}{f_1^2 - f_2^2} \, \frac{c}{K} + \mathrm{const}\,, \tag{6}$$

where the dimensional factor is $K = 40.308$ m^3 s^{-2} and $c = 3 \times 10^8$ m s^{-1} is the speed of light in the vacuum.

We note that by using the phase measurement data L_1 and L_2, it is possible to calculate the TEC only up to an unknown constant, which is specified in Eqn (6) as an extra additive term. Relation (6) is similar to (1) with an unknown constant in the right-hand side of the system of equations.

The pseudo ranges P_1 and P_2 also allow determining the TEC as [29]

$$\mathrm{TEC} = \frac{P_2 - P_1}{1/f_2^2 - 1/f_1^2}\,. \tag{7}$$

However, such data are distorted and are much noisier than the phase data. The noise level in P_1 and P_2 is usually no less than 20% – 30%. At the same time, the noise in the phase data is typically less than 1% and rarely reaches a few percent. Therefore, it seems preferable to use the phase data for HORT.

In an overwhelming majority of studies (see, e.g., [6]), the HORT problems are solved by a set of linear integrals, i.e., it is supposed that TEC sets are determined with sufficient accuracy according to phase and group path data (6) and (7). However, the accuracy of the absolute TEC determination in (7) is low, and only the TEC differences in (6) are measured with high accuracy; therefore, the phase difference approach was also used here [28]. In other words, not the absolute TEC values but the corresponding differences or time derivatives $\mathrm{d(TEC)}/\mathrm{d}t$ were used as input data for the RT problem.

To solve the four-dimensional RT problem according to GNSS data, it is possible to use the approach developed in the two-dimensional LORT. The electron concentration distribution is represented as an expansion with respect to some local basic functions, and then the set of linear integrals or differences between linear integrals is transformed into a system of linear equations. However, the four-dimensional RT, unlike the two-dimensional one, requires an additional interpolation procedure for the solutions found in the region of absent data. Realization of this approach in regions with a dense network of stations (North America, Europe) gave good results on a sufficiently coarse network by choosing suitable splines with various smoothness [28, 30].

Another approach is based on the idea of seeking sufficiently smooth solutions of the problem, for which the algorithms used would provide good interpolation in regions of absent data. For example, we choose a Sobolev norm and seek a solution minimizing this norm over an infinite set of solutions of the initial (underdetermined) tomographic problem (5):

$$AN = D\,, \qquad \min_{AN=D} ||f - f_0||^2_{W_n^2}\,.$$

The difficulties encountered in the realization of this approach are related to the solution of a constrained minimization problem. The direct way to solve this problem, based on the Lagrange multiplier method, leads to a linear system with large-size matrices (due to a large number of rays), which, in addition, do not have a special structure that could simplify finding the solution. Therefore, an iterative method was suggested to solve the minimization problem, which is a variant of the SIRT (simultaneous iterative reconstruction technique) method with additional smoothing by filtration of iterative gains over spatial variables [28]. The method allows taking the a priori information into account expressed both in the initial approach for iterations and in the form of weight coefficients that set relative scales for the electron concentration variations at various heights.

Computer modeling demonstrated a reasonable reconstruction quality for quasistationary structures, although the HORT resolution is considerably lower than the LORT resolution. As a rule, in Europe and on the main part of the territory of the USA, the vertical and horizontal HORT resolutions are no better than 100 km. Only in the regions of the dense networks of southern California and Japan can the resolution reach 30 – 50 km.

To illustrate the results of applying the developed HORT methods, we give examples of reconstructions. In Fig. 5, an example of the ionospheric trough evolution over Europe on the evening of April 17, 2003 is shown. On the TEC maps and the meridional vertical cross sections (along 21° longitude), a trough expansion in the background of the electron concentration decrease during the night is seen. Figure 6 shows an anomalous electron concentration increase (up to 3×10^{12} m^{-3}) over the Arctic during the strongest magnetic storm on October 29 – 31, 2003. The increase in the electron concentration on the night side is related to plasma convection from the day side to the night side. The regions of increased ionization look like 'tongues' with an inhomogeneous spotted structure (Fig. 6a, b), which is also shown in the vertical sections (Fig. 6c, d). The sections are drawn along the lines shown on TEC maps (Fig. 6a, b). Apparently, this structure of inhomogeneities is related to the instability of the ionospheric plasma and the appearance of quasiwave structures.

4. Combination of radio tomography with other sounding methods

Systems using the radio occultation (RO) method (FORMOSAT-3/COSMIC and others registering GNSS signals with low-orbit satellites) allow obtaining quasitangential projections of the electron density N [31 – 33]. The RT method with ground-based reception implies ionospheric sounding in a wide range of various positions of receiving–transmitting systems. In this sense, the RO method giving integrals of N in the family of quasitangential rays (the

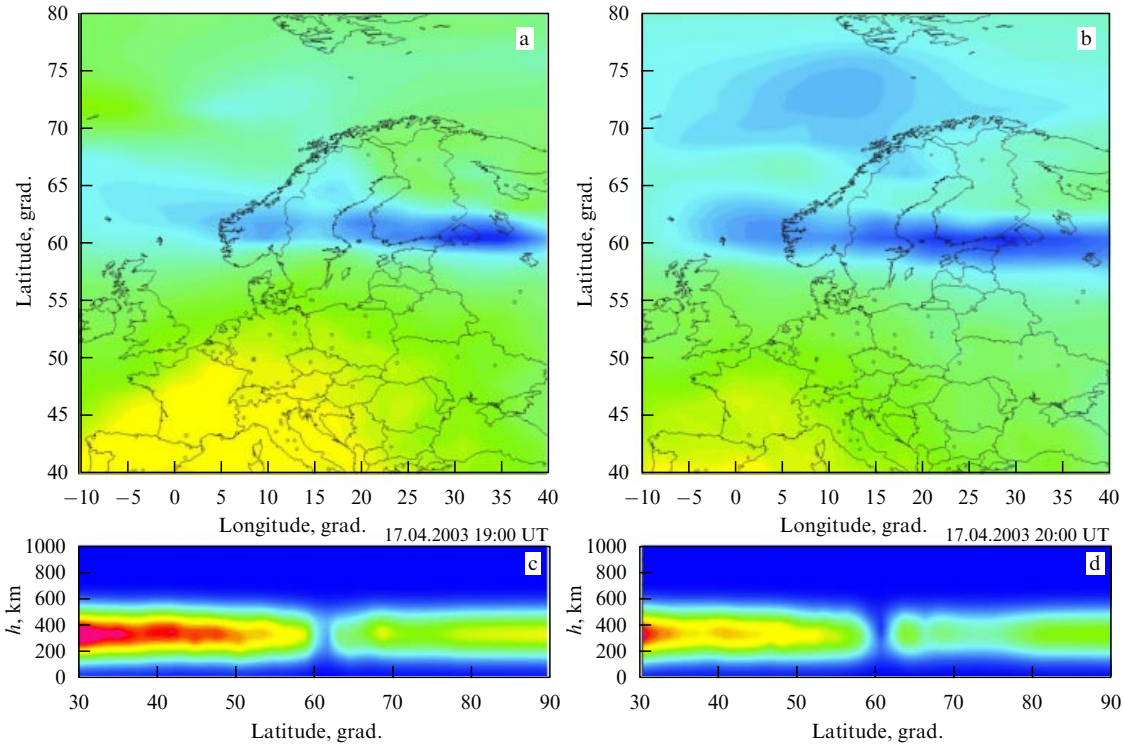

Figure 5. The ionospheric HORT reconstruction over Europe on April 17, 2003: (a, c) 19 : 00 UT, (b, d) 20 : 00 UT. (a, b): TEC maps in the latitude–longitude coordinates; the color scale is from 0 to 35 TECU (1 TECU = 10^{16} m^{-2}). (c, d): Vertical sections of the ionospheric electron density along 21° East in the latitude–altitude coordinates; the color scale is from 0 to 0.6×10^{12} m^{-3}.

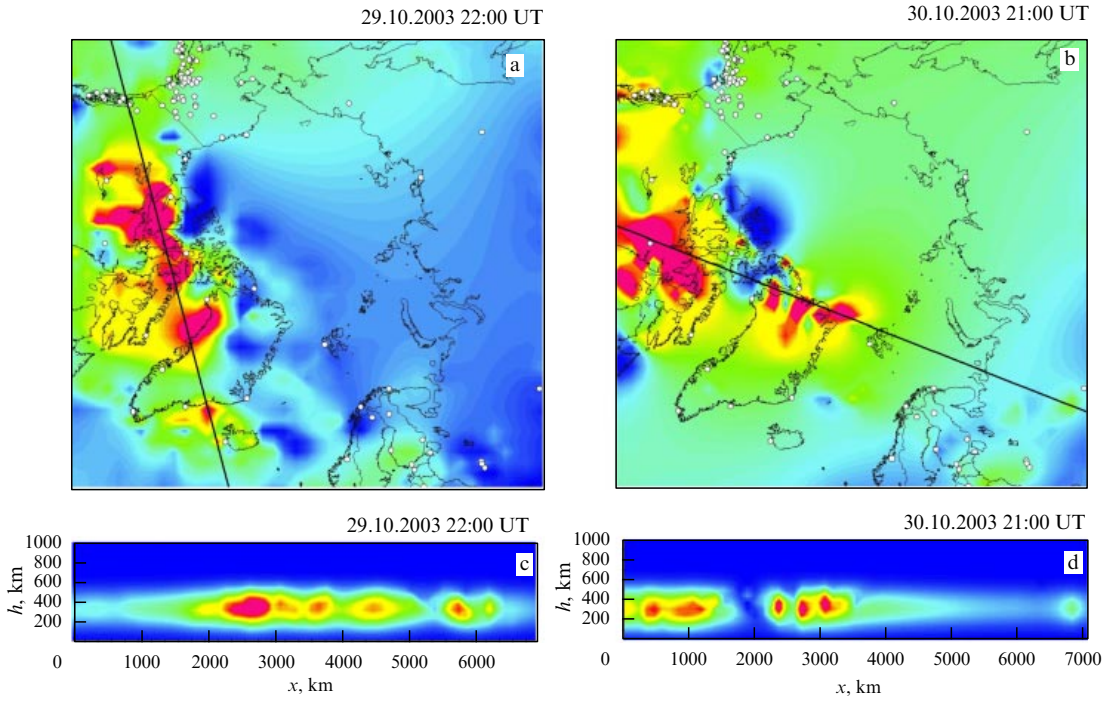

Figure 6. The ionospheric HORT reconstruction over the Arctic on October 29 and 30, 2003. (a, b): TEC maps; the color scale is from 0 to 60 TECU. (c, d): Vertical sections of the ionospheric electron density along lines shown on the TEC chart; x is the distance on Earth's surface along highlighted lines and h is the height; the color scale is from 0 to 2.5×10^{12} m^{-3}.

satellite–satellite paths) is a particular case of the RT method; therefore, a procedure to include RO data into a general tomographic scheme can be constructed [7, 34]. The combined application of the RT and RO methods, in which sounding data on the satellite–satellite paths (RO method data) are added to RT data of ground-based receivers, can lead to a noticeable refinement of the vertical resolution of RT reconstructions.

We note that the presented RT methods are related to ray tomography [1], in which diffraction effects can be neglected.

Earlier, we developed the diffraction and statistical RT methods [1, 2, 7]. The diffraction RT method allows reconstructing the structure of individual localized inhomogeneities with the diffraction effects taken into account. Statistical RT methods give an opportunity to obtain the spatial structure of the statistical characteristics of a stochastically nonuniform ionosphere [7, 35].

5. Conclusion

We have briefly reviewed the main results of tomographic ionospheric studies completed with our participation. A brief description of satellite radio tomography methods of the near-Earth plasma, including LORT and HORT, has been given. During the last two decades, numerous ionospheric RT studies of the near-equatorial, middle, sub-auroral, and auroral latitudes have been carried out in various regions of the world (Europe, USA, Southeast Asia). We have given examples of experimental RT reconstructions of the electron concentration distributions in the ionosphere.

The satellite RT system is a distributed sounding system: the moving artificial Earth satellites and a network of receivers give an opportunity to continuously sound the medium in various directions and to reconstruct the spatial structure of the ionosphere. The LORT systems allow obtaining 'instantaneous' (10 – 15 min) two-dimensional cross sections of the ionosphere at distances of a few thousand kilometers. The HORT systems, based on a network of independent receivers, together with traditional ionospheric sounding methods, allow realizing the regional and global monitoring of the near-Earth plasma.

This work is supported by the RFBR (grant nos 08-05-00676 and 10-05-01126).

References

1. Kunitsyn V E, Tereshchenko E D *Tomografiya Ionosfery* (Tomography of the Ionosphere) (Moscow: Nauka, 1991)
2. Kunitsyn V E, Tereshchenko E D *IEEE Antennas Propag. Mag.* **34** (5) 22 (1992)
3. Leitinger R, in *Review Radio Science. 1996 – 1999* (Eds W R Stone) (Oxford: Science Publications, 1999) p. 581
4. Kunitsyn V, Tereshchenko E *Ionospheric Tomography* (Berlin: Springer-Verlag, 2003)
5. Pryse S E *Surv. Geophys.* **24** 1 (2003)
6. Bust G S, Mitchell C N *Rev. Geophys.* **46** RG1003 (2008)
7. Kunitsyn V E, Tereshchenko E D, Andreeva E S *Radiotomografiya Ionosfery* (Radio Tomography of the Ionosphere) (Moscow: Fizmatlit, 2007)
8. Andreeva E S, Kunitsyn V E, Tereshchenko E D *Ann. Geophys.* **10** 849 (1992)
9. Kunitsyn V E et al. *Ann. Geophys.* **13** 1263 (1995)
10. Andreeva E S et al. *Pis'ma Zh. Eksp. Teor. Fiz.* **52** 783 (1990) [*JETP Lett.* **52** 145 (1990)]
11. Pryse S E, Kersley L *J. Atm. Terr. Phys.* **54** 1007 (1992)
12. Oraevsky V N et al. *Geomagn. Aeron.* **35** (1) 117 (1995)
13. Andreeva E S et al. *Geophys. Res. Lett.* **27** 2465 (2000)
14. Franke S J et al. *Radio Sci.* **38** 1011 (2003)
15. Yeh K C et al. *Geophys. Res. Lett.* **20** 4517 (2001)
16. Andreeva E S *Vestn. Mosk. Gos. Univ. Ser. 3. Fiz. Astron.* (2) **62** (2004) [*Moscow Univ. Phys. Bull.* **59** 67 (2004)]
17. Foster J C et al. *Int. J. Imaging Syst. Technol.* **5** 148 (1994)
18. Nygrén T et al. *Radio Sci.* **32** 2359 (1997)
19. Pakula W A et al. *Radio Sci.* **30** 89 (1995)
20. Kunitsyn V E et al. *Vestn. Mosk. Gos. Univ. Ser. 3. Fiz. Astron.* (6) 102 (2009) [*Moscow Univ. Phys. Bull.* **64** 661 (2009)]
21. Kunitsyn V E et al. *Ann. Geophys.* **13** 1351 (1995)
22. Ahmadov R R, Kunitsyn V E *Int. J. Geomagn. Aeron.* **5** GI2002 (2004)
23. Andreeva E S et al. *Kosmich. Issled.* **39** (1) 13 (2001) [*Cosmic Res.* **39** 10 (2001)]
24. Tereshchenko E D et al. *Ann. Geophys.* **16** 812 (1998)
25. Tereshchenko E D et al. *Phys. Lett. A* **325** 381 (2004)
26. Frolov V L et al. *Usp. Fiz. Nauk* **177** 330 (2007) [*Phys. Usp.* **50** 315 (2007)]
27. Kunitsyn V E et al. *Geophys. Res. Lett.* **30** 1851 (2003)
28. Kunitsyn V E at al. *Vestn. Mosk. Gos. Univ. Ser. 3. Fiz. Astron.* (1) 74 (2005) [*Moscow Univ. Phys. Bull.* **60** 94 (2005)]
29. Hofmann-Wellenhof B, Lichtenegger H, Collins J *Global Positioning System: Theory and Practice* (Wien: Springer-Verlag, 1992)
30. Kunitsyn V E et al. *Vestn. Mosk. Gos. Univ. Ser. 3. Fiz. Astron.* (6) 67 (2004)
31. Hajj G A et al. *Int. J. Imaging Syst. Technol.* **5** 174 (1994)
32. Kursinski E R et al. *Science* **271** 1107 (1996)
33. Yakovlev O I, Pavel'ev A G, Matyugov S S *Sputnikovyi Monitoring Zemli: Radiozatmennyi Monitoring Atmosfery i Ionosfery* (Satellite Monitoring of the Earth: Radio Eclipse Monitoring of the Atmosphere and Ionosphere) (Moscow: Librokom, 2009)
34. Andreeva E S, Berbeneva N A, Kunitsyn V E *Geomagn. Aeron.* **39** (6) 109 (1999) [*Geomagn. Aeron.* **39** 776 (1999)]
35. Tereshchenko E D et al. *Radio Sci.* **39** RS1S35 (2004)

PACS numbers: **07.87.+v**, **94.20.–y**, **94.80.+g**
DOI: 10.3367/UFNe.0180.2010051.0554

Space research at the Pushkov Institute of Terrestrial Magnetism, Ionosphere and Radio Wave Propagation, Russian Academy of Sciences

V D Kuznetsov

1. Introduction

The space research at the Pushkov Institute of Terrestrial Magnetism, Ionosphere and Radio Wave Propagation, RAS (IZMIRAN) covers all the main areas of the institute activities: the study of the ionosphere and wave propagation, terrestrial and planetary magnetism, and solar–terrestrial physics. During the 70 years of its history, 50 of which are related to space research, IZMIRAN has participated in more than 50 space projects and conducted space research from the first artificial Earth satellite (AES) to modern complex space observatories like Interkosmos-19, APEX, CORONAS-F, and Compass-2. Substantial progress in the investigations pursued by the institute in recent years has been inseparably linked with spacecraft-borne measurements. Space research is an important constituent in the complex approach to the study of diversified and complex phenomena and physical processes in the Sun–Earth system, objects like the Sun, the terrestrial magnetosphere, the ionosphere, etc., which require dedicated experiments and a comprehensive analysis of observational data and their comparison with theoretical models.

V D Kuznetsov Pushkov Institute of Terrestrial Magnetism, Ionosphere and Radio Wave Propagation, Russian Academy of Sciences, Troitsk, Moscow region, Russian Federation
E-mail: kvd@izmiran.ru

Uspekhi Fizicheskikh Nauk **180** (5) 554 – 560 (2010)
DOI: 10.3367/UFNr.0180.201005l.0554
Translated by E N Ragozin; edited by A M Semikhatov

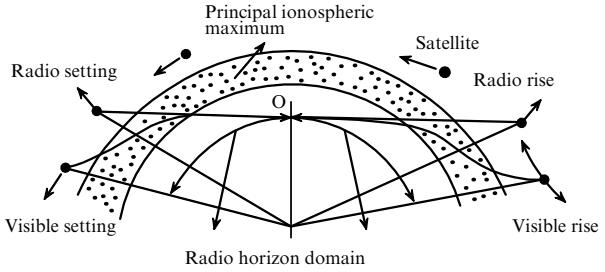

Figure 1. Observation of the radio rising and radio setting of the first AES, which respectively occurred before and after satellite's optical rising and setting behind the horizon owing to the effect of radio wave refraction in the ionosphere. (Adapted picture borrowed from Ref. [3].)

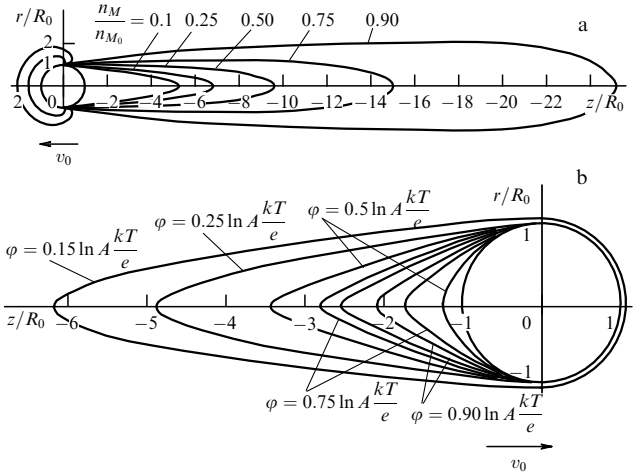

Figure 2. (a) Contours of equal particle density (the plasma rarefaction is indicated with mumbers). (b) Contours of equal potential in the vicinity of a metal satellite. (Borrowed from Refs [4, 5].)

It is noteworthy that in 1957, IZMIRAN carried out the world's first space experiment with the first AES, in which a radio beacon was used to observe the effects of radio rise and radio setting of the satellite, and outer ionospheric layers were studied [1, 2] (Fig. 1). Even prior to the launch of the first AES, A V Gurevich — at that time, a staff member at IZMIRAN — made the first theoretical calculations of the interaction of a metal satellite with rarefied ionospheric plasmas and obtained density and electric potential distributions in the vicinity of the satellite [4, 5] (Fig. 2). These distributions were important for the formulation and interpretation of different satellite-borne experiments and underlay the subsequent more sophisticated investigations of this problem [6, 7].

The main space projects carried out with IZMIRAN's participation are listed in Table 1. They are subdivided into two main groups: projects aimed at studying near-Earth space (NES) — the magnetosphere and the ionosphere — and spacecraft-borne projects to investigate space beyond NES, which involve investigations of the Sun and the planets of the Solar System. Given below is a brief discussion of the main findings that have emerged from the implementation of space projects, the current status of ongoing space research, and the prospects of future research in this area.

2. Space ionospheric research

The structural study of the outer ionosphere, whose smooth electron density distribution at a height above the principal maximum was first determined using the radio beacon of the first AES [1, 2], was continued with the use of the Interkosmos-19 satellite (1979 – 1982) by on-board outer ionosphere probing with an ionosonde developed at IZMIRAN [8]. The probing was effected over a vast terrestrial region and a detailed matching of the inner and outer profiles of the electron density was made (Fig. 3). Interkosmos-19, which was one of the most successful ionospheric research projects, yielded a wealth of data, which underlay the construction of the global parameter distribution for the outer ionosphere for different points in local time and different conditions; new elements of the global ionospheric structure were discovered: an annular ionospheric dip and a low-latitude ionization dip; longitude variations of ionosphere parameters were investigated, the characteristics of the principal ionospheric dip and its dynamics during magnetic storms were found, the effect of the B_z-component of the interplanetary magnetic field on the structural change of the equatorial anomaly was established, the phenomenon of F-scattering in the outer ionosphere and radio wave propagation in the region of structural iono-

Table 1. Space projects with IZMIRAN's participation

Projects	NES magnetosphere, ionosphere	The Sun and solar–terrestrial physics, planets
Realized	First AES, third AES, Cosmos-1 (-12, -26, -49, -321, -381, -1809), Electron-2 (-4), Intercosmos-3 (-5, -10, -13, -18, -19), Intercosmos-24 (Aktivnyi), Intercosmos-25 (APEX), Prognoz-1 (-6, -7, -9), Intasat, ATS-6, Tsikada, Oreol-3, Intercosmos-Bolgariya-1300, Interbol, Compass-2, balloons	Luna-1 (-2, -10), Lunokhod-2, Venera-1 (-2, -4, -9, -10), Mars-2 (-3, -5), Soyuz-Apollo, Vega-1 (-2), Fobos-2, CORONAS-I, CORONAS-F
At realization stage (ongoing)	CE* Impul's (RS ISS**), balloon experiments	CORONAS-Foton (SOKOL experiment)
At preparation stage (development work)	CE Molniya-Gamma (RS ISS), CE Seismoprognoz-SM (RS ISS), CE Gidroksil (RS ISS), Rezonans	Interhelioprobe, Luna-Glob, Luna-Resurs
At development stage (research work)	Ionosat, Geomag, GLONASS-Nauka	PEP, Sistema

* CE, cosmic experiment.

** RS ISS, Russian Segment of the International Space Station.

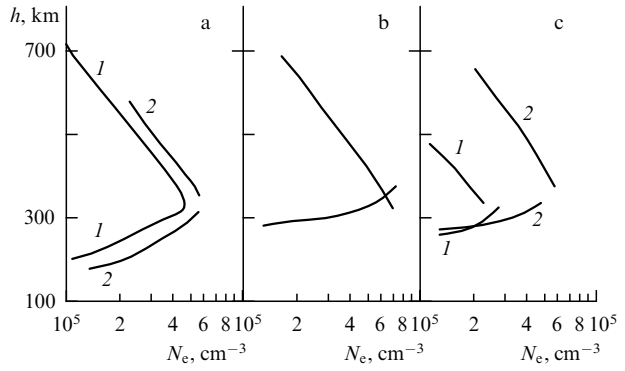

Figure 3. Different versions of the matching of the ionospheric electron density distribution profiles obtained from ground-based measurements (the lower profile, low altitudes) and from Intercosmos-19 satellite data (upper profile). The line pairs 1 and 2 correspond to different observations.

spheric features were studied; the outer $N_e(h)$-profile and the global model of electron temperature were constructed; the ionospheric effects of strong earthquakes were localized; the effects of a high-power internal gravity wave were found to possibly embrace the entire depth of the outer ionosphere up to the satellite altitude ($\approx$ 1000 km).

Satellite-borne investigations of the ionosphere, magnetosphere, and near-Earth plasma were continued in the projects Aktivnyi (Interkosmos-24 AES launched in 1989), APEX (Active Plasma EXperiments) (Interkosmos-25 AES launched in 1991), and Compass-2 (launched in 2006).

The very-low-frequency (VLF) effects of the underground nuclear explosion on Novaya Zemlya Island on October 24, 1990 (broadband data) were discovered with the Interkosmos-24 (Aktivnyi, 1989 – 1991) AES [9]. Observed in the extremely low frequency (ELF) range (narrowband data) were anomalously high absolute values of the electric field component during typhoons, primarily above the subequatorial region of the Pacific Ocean. An analysis of the spectra of whistling atmospherics performed in flight above seismoactive regions under different geophysical conditions enabled separating seismic and geomagnetic effects in the D-region of the ionosphere.

Active experiments involving the injection of plasma beams into ionospheric and magnetospheric plasmas were performed with the Interkosmos-25 (APEX, 1991 – 1999) AES [10]. A series of ground-based and satellite-borne experiments have allowed obtaining real-time tomographic reconstructions of ionospheric profiles, discovering inclined and 'oblique' ionospheric dips (electron density lowerings) in middle and high latitudes of the polar region, and performing the diagnostics of numerous natural ionospheric phenomena: the principal ionospheric dip, plasma bubbles, the equatorial anomaly, and plasma radiation at gyrofrequency harmonics. Ionospheric measurements were made above the site of operation of heating facilities, and the effect of nontunnel radiowave transmission through the wave ionospheric barrier was recorded. The APEX satellite data were used to develop methods of satellite radio tomography with a network of ground-based radiotomographic facilities. A group of authors including V N Oraevskii and Yu Ya Ruzhin were awarded a 1998 State Prize in Science and Technology for this work.

Measurements of the amplitude–frequency characteristics of VLF waves upon injection of plasma beams were also conducted in the framework of the APEX project. The VLF wave excitation was accompanied by the acceleration of high-energy electrons and ions up to 500 – 700 keV; these electron fluxes were detected by the Magion-3 subsatellite. Such generation of high-energy charged particles was discovered for the first time. Lower-energy electron fluxes were also recorded, testifying to resonance mechanisms of the interaction between the excited waves and background plasma particles in the injection of electrons. High-frequency (HF) wave excitation at the point of injection was recorded by the main satellite and by the Magion-3 subsatellite. In the regime of modulated beam injection, it was possible to obtain data related to the formation of special electromagnetic plasma structures that induce electromagnetic fields in the VLF range like a VLF antenna in plasma. Electron injection in an unmodulated regime results in HF pumping in the injection region and further relay-race wave energy transfer to the low-frequency spectral domain, thereby enhancing low-frequency turbulence. The analysis of the data obtained continues.

The procedures for measuring ionospheric parameters and investigating different ionospheric phenomena caused by natural perturbations and anthropogenic factors were elaborated and tested in experiments performed aboard the Compass-2 small satellite (2006 – 2007). In the framework of concerted ground-based and satellite measurements with the Compass-2 small spacecraft (SS) performed jointly with the Institute of Cosmophysical Research and Radio Wave Propagation, Far East Division of the RAS, electric and electromagnetic processes in the near-surface atmosphere of the seismoactive Kamchatka region were investigated experimentally, with the aim to study the lithospheric–atmospheric–ionospheric relation during the preliminary phases of earthquakes. The effects of different sources (of a meteorological, geomagnetic, and seismic nature) were investigated from the measurements of the variations of the quasistatic electric field strength, the intensity of natural VLF radiation ($f = 20 - 20000$ Hz), and the variations of the geomagnetic field. Oscillations in the power-density spectra of these parameters were discovered in a wide range of atmospheric waves: internal gravity waves (with periods $T = 0.5 - 3.3$ h), thermal tidal waves ($T = 4 - 24$ h), and planetary-scale waves ($T > 24$ h), which may be regarded as experimental confirmation of one of the possible lithospheric–ionospheric interaction mechanisms involving internal gravity waves. It was found that the oscillations with $T = 0.5 - 1.5$ h become stronger during the preliminary phase of earthquakes and that their source is localized in the near-surface atmosphere. Waves with such periods are capable of reaching the altitudes of the dynamo region of the ionosphere ($h \approx 120 - 130$ km). Oscillations with $T = 1.5 - 3.0$ h are enhanced for high geomagnetic activity. The source of these oscillations is localized in the dynamo region of the polar ionosphere or higher. In the study of whistler propagation at altitudes of 400 km, it was determined from the Compass-2 SS data that under certain conditions, the low-frequency whistler branch reaches zero frequency in a finite time, rather than tending to a nonzero asymptote.

The cooperation of several scientific institutions (Radiophysical Research Institute, Central Research Institute of Machine Building) under IZMIRAN's coordination resulted in the realization of a series of experiments aboard the Russian segment of the International Space Station (ISS RS) on recording the influence of the Sura radio heating facility on the terrestrial ionosphere. In one of these experiments

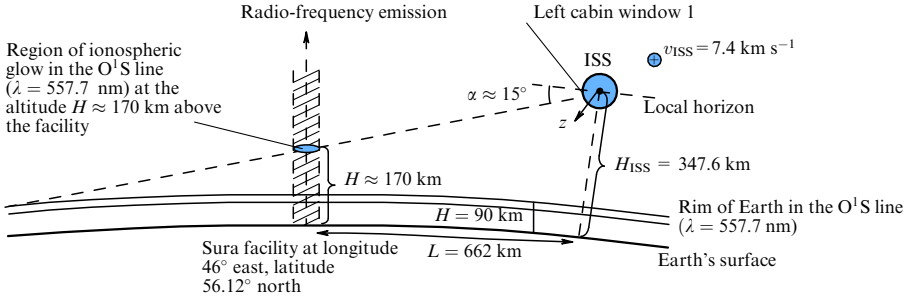

Figure 4. Layout of the experiment aboard the ISS RS for recording the effect of the Sura radio heating facility on the terrestrial ionosphere.

performed on October 2, 2007 using the Relaksatsiya equipment aboard the ISS RS (Fig. 4), a weak atmospheric glow was observed in the O^{1}S line ($\lambda = 557.7$ nm) in the direction of the heating region above the Sura facility. This glow coincided in time with the period of operation of the heating facility [11, 12]. The observed glow could not have been caused directly by the heating effects owing to the low power of the heating radiation, and might have been caused by particle precipitation from a magnetic tube stimulated by the effects of modulated heating, when the modulation period of the heating radiation was close to the period of Alfvén eigenmodes of the tube. The processing and analysis of the resultant data continues, as does the preparation for pursuing new experimental sessions.

In the Impul's experiment aboard the ISS RS, which is being carried out by IZMIRAN in cooperation with Moscow Aviation Institute (MAI) in 2009–2010, a pulsed plasma injector (with the ion velocity about 30–40 km s^{-1}, plasma ionization degree $\beta = 10\%$, injection periodicity 1.8 ± 0.2 Hz, and pulse duration of the order of 10 μs) is being used to study the effects of ionospheric modification. Test injection sessions have been conducted, the equipment is being calibrated, and optimal modes for its operation are being selected. It is planned to record the influence of injection by means of onboard instrumentation and ground-based IZMIRAN facilities in the low-frequency (LF), ultralow-frequency (ULF), ELF, and VLF ranges.

IZMIRAN is developing promising space projects in ionospheric research — a series of experiments on the RS ISS, the Ionosat satellite project, and a project involving the use of the Global Navigation Satellite System (GLONASS).

Three cosmic experiments (CEs) are in the stage of preparation for realization on the RS ISS: 'Molniya-gamma' to study atmospheric gamma-ray and optical radiation bursts in thunderstorm conditions (2010), 'Seismoprognoz-SM' to investigate physical effects in the NES arising from the lead-up to earthquakes and the anthropogenic impact (2011), and 'Gidroksil' to study the optical radiation of the upper atmosphere and its response to anomalous natural and anthropogenic effects (2012).

The Ionosat satellite project is aimed at studies of the ionosphere as an indicator of solar–terrestrial and litho-spheric–atmospheric interactions. This satellite will be a part of a cluster of three closely located satellites intended for studying the small-scale structure and nonuniformity of the ionosphere.

To monitor and diagnose the terrestrial plasmasphere and magnetosphere, IZMIRAN has formulated a proposal to use GLONASS. The heart of this proposal consists in every spacecraft (SC) of the GLONASS system accommodating a

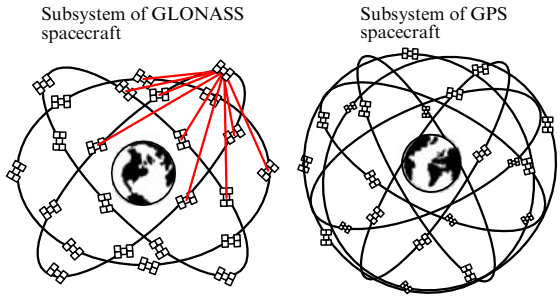

Figure 5. Schematic of using GLONASS for monitoring and diagnosing the terrestrial plasmasphere and magnetosphere.

transmitter–receiver facility to afford continuous measurement of the phase delay of coherent 150/400 MHz signals between any pair of SCs within the line-of-sight range (Fig. 5). The algorithm for processing the measurement data by radiotomographic techniques will enable reconstructing the three-dimensional structure of the inner magnetosphere and its dynamics caused by the influence of natural and anthropogenic sources. The measurement scheme may also incorporate the signals of GPS satellites and other satellite systems.

3. Magnetic measurements on spacecraft

Magnetic fields are one of the most important characteristics of Earth, the interplanetary medium, the planets, and small bodies of the Solar System.

Using the third AES (1958), IZMIRAN performed the first-ever cosmic experiment to measure the geomagnetic field with an SG-45 magnetometer (Fig. 6) [13, 14]. The resultant data for the first time permitted comparing the measured geomagnetic field with different versions of its analytic representation and choosing the most precise one. Also

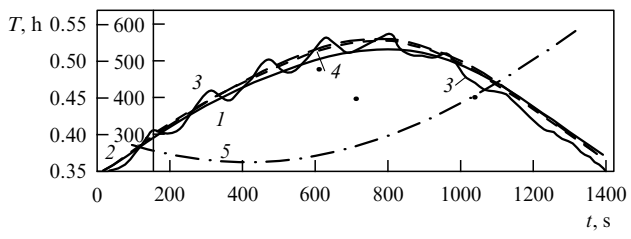

Figure 6. Magnetograms of the measured and calculated values of the magnetic field along the trajectory of the third AES: *1*, *2* — calculated, *3* — measured, *4* (dashed) — measured, allowing for deviation. Line *5* represents the satellite altitude.

shown was the feasibility of using the geomagnetic field for determining spacecraft orientation.

More recently, a world magnetic survey was made in a series of satellite measurements. Measurements made with a proton magnetometer PM-4 developed in IZMIRAN, which was installed on Kosmos-26 (1964) and Kosmos-49 (1964) satellites, covered 75% of the terrestrial surface; the magnetic anomalies related to the structure and tectonics of Earth's crust were determined to stretch to the altitudes of low-orbit satellites [15, 16]. These measurement data became a part of the analytic model for the International Geomagnetic Reference Field for 1965. With the Kosmos-321 satellite (1970), the geomagnetic field was measured over 94% of the terrestrial surface [17]. These data allowed studying the magnetic effects of longitudinal currents in high-latitude regions of the ionosphere and determining the magnetic effects caused by the equatorial current jet. These data became a part of the analytic model for the International Geomagnetic Reference Field for 1970.

The precision with which an analytic model approximates the geomagnetic field and especially the anomalous magnetic field is determined by the satellite magnetic survey density. In the Geomag project developed by IZMIRAN, it is planned to use a system of five small polar-orbit satellites for a global survey of the terrestrial magnetic field. Measurements along these orbits would furnish a substantial improvement of the representation of the anomalous magnetic field.

Magnetic measurements on the Electron-2 and Electron-4 satellites (1964, 1965) for the first time enabled investigating the field topology in the high-latitude outer terrestrial magnetosphere and in the trapped radiation zone, revealing indications of the penetration of solar wind plasmas through the cusp into the magnetosphere, constructing the first model of the terrestrial magnetosphere that includes tail formation, and studying the altitude–time electron density distribution and the nonuniform structures of the outer ionosphere [18]. With the Interkosmos-Bolgariya-1300 satellite (1981), the longitudinal currents in the polar terrestrial ionosphere and strong jumps in electric fields and particle fluxes in the polar ionosphere were investigated [19].

In the framework of the projects Prognoz (1971 – 1985) and Interbol (1995 – 2000) (lead organization: the Institute of Space Research (ISR), RAS), magnetic measurements were performed with the use of IZMIRAN's magnetometers in the outer terrestrial magnetosphere and the interplanetary space [20]. Based on the resultant magnetic data combined with plasma measurements in the Interbol project, the fine structure of the outer boundary and layers of the magnetosphere were investigated that comprise the outgoing shock wave, the magnetopause, the magnetosheath, and the boundary layer [21]. Also investigated were flux transfer events (FTEs) associated with the pulsed reconnection of magnetic field lines of the magnetosheath and magnetosphere, as well as the longitudinal currents flowing along the geomagnetic field lines in the auroral zone of the magnetosphere.

IZMIRAN's experiment in the Rezonans project (ISR, RAS), which is under preparation, is aimed at the pursuance of magnetic measurements in the study of resonance plasma processes in the magnetosphere and the effects of a magnetospheric cyclotron maser, the prerequisites for which may be realized in isolated geomagnetic field tubes [22].

Successful magnetic measurements in the near-Earth space have allowed conducting similar measurements on interplanetary stations in the study of the planets and small bodies of the Solar System. Proceeding from the analysis of the first magnetic measurements performed by IZMIRAN with Luna-2 (1959) and Luna-10 (1966) unmanned interplanetary probes, the Moon was found to have no dipole magnetic field of appreciable strength [23].

For the first magnetic measurements in space, a group of invstigators, including IZMIRAN's Director N V Pushkov and the leading magnetologist Sh Sh Dolginov, were awarded one of the first Lenin Prizes in the area of space research (1960).

Magnetic measurements on Lunokhod-2 (1973) permitted determining the correlation between local magnetic fields (6 – 300 nT) and tectonic relief features (craters, fractures, etc.) [24].

Discovered in the samples of lunar soil brought to Earth was a relatively strong magnetization the rock acquired in fields up to 100,000 nT. The study of the nature of this heretofore unknown magnetization is one of the fundamental issues in lunar investigations that remains to be solved. IZMIRAN's participation with magnetic measurements in the Luna-Glob (lunar orbital satellite) and Luna-Resurs (landing module) projects under preparation is aimed at solving this important question of lunar origin.

Magnetic measurements in the study of Venus and Mars in the series of projects Venera-4 (1967), Venera-9, and Venera-10 (1975) and Mars-2 (-3, -5) (1972 – 1974) have shown that Venus and Mars have no intrinsic dipole field and that their magnetospheres, like the cometary ones, are induced. Venus and Mars were discovered to have a bow shock wave and a magnetic plasma tail, which have been investigated [25, 26]. In the Phobos-2 (1989) and Vega-1 (-2) (1986) projects, the interaction of solar wind with Halley's Comet and the environment of the Mars satellite Phobos was studied [27, 28].

Magnetic measurements with balloons enable obtaining data about the low-altitude geomagnetic field, comprehensively studying magnetic anomalies on the terrestrial surface, and refining models of the geomagnetic field subject to continuous changes. In 2007 – 2009, IZMIRAN performed pioneering balloon-borne experiments in measuring and using vertical geomagnetic field gradients in the stratosphere with the aid of a balloon-borne magnetic gradiometer developed in [29]. This instrument is an exclusive IZMIRAN product and is unprecedented in the world's practice of geomagnetic research. Techniques have been devised for extracting the field of magnetic anomalies from the data of balloon-borne gradient magnetic surveys and the amplitude spectrum of magnetic anomalies was studied along the trajectory of a balloon flight from Kamchatka to Povolzh'e, which revealed regional and long-wavelength magnetic anomalies. The parameters of the sources of these anomalies were studied by different methods, including spectral ones. The findings of this research permitted improving the spatial accuracy of the data on the depth structure of Earth's crust and improving its magnetic model.

Combining modern satellite- and balloon-borne geomagnetic measurements allows achieving a satisfactory agreement of experimental data with the theoretical models of geomagnetic field generation and advancing the studies of the magnetic properties of Earth's crust, magnetic anomalies, and other features of geomagnetic field distribution.

4. Solar and solar–terrestrial physics

In recent years, beginning from the 1990s, IZMIRAN has broadened the scope of its space research: with IZMIRAN as the lead organization, two major space projects involving solar research, CORONAS-I and CORONAS-F have been carried out, which are constituents of the CORONAS (complex orbital near-Earth observations of Solar activity) program [30, 31].

With the use of data from the CORONAS-F satellite, coronal mass ejections (CMEs) and their related manifestations of solar activity, which have a high degree of geoefficiency, were investigated [32]. It was determined that the eruption of large CMEs involves global solar magnetospheric structures with a spatial scale far exceeding the size of active regions and ordinary activity systems. The large-scale regions of low brightness in extreme ultraviolet and soft X-ray regions (dimmings) observed in this case visualize the structures involved in the CMEs, which are supposedly produced due to the opening (extension) of magnetic field lines and the plasma outflow from transient coronal holes. The substantial rearrangement of the magnetic field, the partial opening of field lines, and the matter outflow that occur in a CME take place in the corona, but also affect the cold plasma of the transition layer.

On the CORONAS-I and CORONAS-F satellites, solar brightness variations at wavelengths ranging from ultraviolet to infrared were observed and global solar oscillations were studied with the use of the DIFOS (Differential Solar Oscillation Photometer) instrument. Power-density spectra were constructed for global low-l ($l = 0, 1, 2$) p-mode oscillations (Fig. 7) [33, 34]. It was experimentally determined that the p-modes exhibited frequency splitting due to solar rotation. Out-of-phase long-period p-mode amplitude variations of global solar oscillations were found to occur, which reflect internal solar dynamics, and an appreciable increase in the amplitude of global oscillations was observed in the ultraviolet spectral range. Observations of global solar oscillations were continued in the SOKOL experiment (Solar Oscillations) aboard the CORONAS-Foton satellite (launched on January 30, 2009). The work on the CORONAS-F project was awarded a 2008 Russian Federation Government Science and Technology Prize.

Over the last several years, IZMIRAN has been developing promising solar space projects: the Interhelioprobe project for investigating the Sun at close distances, and the Polar–Ecliptic Patrol (PEP) for observing global solar activity and studying the solar sources of cosmic weather [22, 35]. In the Interhelioprobe project, it is planned to approach the Sun using multiple gravitational maneuvers near Venus due to the commensurability of spacecraft's and Venus's periods of revolution around the Sun. The gravitational maneuvers also enable inclining the spacecraft orbital plane relative to the ecliptic plane. In the PEP project, it is planned to position two spacecraft in two oppositely inclined heliocentric orbits at the distance 0.5 a.u. from the Sun and shift them in orbit by a quarter period relative to each other, such that the Sun–Earth line and the plane of the ecliptic, in which most of mass ejection events and other active phenomena occur, will be uninterruptedly controlled from out-of-ecliptic positions (Fig. 8).

In connection with the projected flights to Mars, during which it will be necessary to ensure the radiation safety of the astronauts and accordingly observe the activity of the side of the Sun invisible from Earth, IZMIRAN is developing the Sistema project, in which three spacecraft spaced at 120° orbit the Sun in the plane of the ecliptic and one spacecraft is in an inclined orbit. This configuration of a system of spacecraft would allow realizing the global monitoring of solar activity, and the Interhelioprobe and PEP projects are regarded as the first steps on the path to the formation of this system.

5. Summary

This report is only a brief review of IZMIRAN's space research, beginning with the world's first space experiment involving the radio beacon of the first AES (1957) and ending with those space projects that are presently operating in space

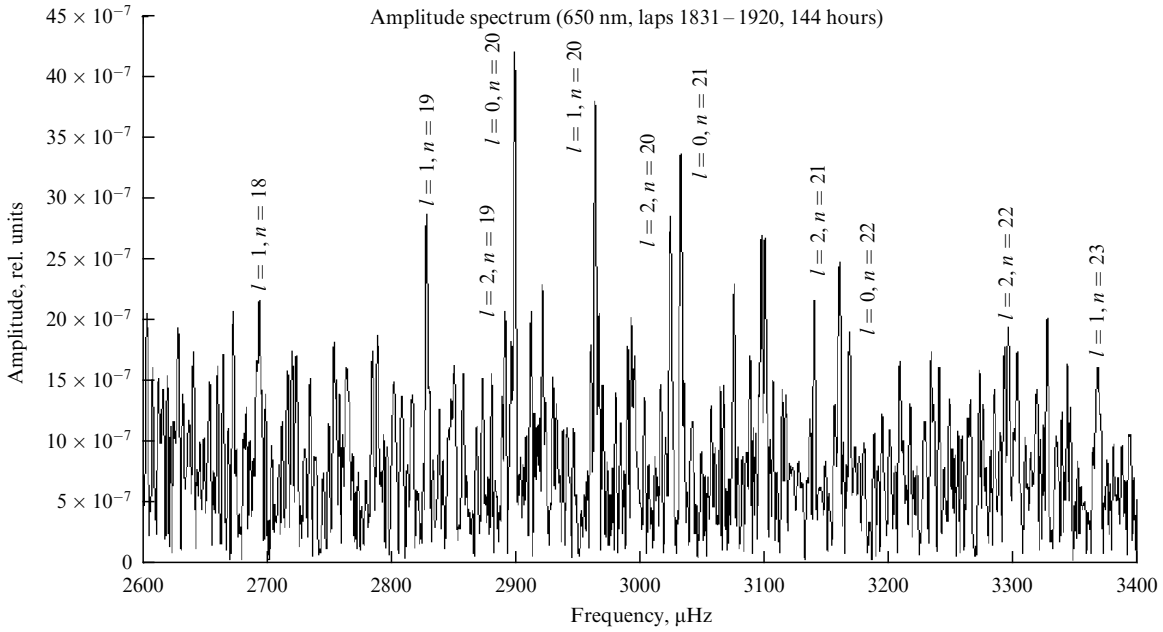

Figure 7. Amplitude spectrum of global solar oscillations derived from the data of the DIFOS experiment aboard the CORONAS-F satellite.

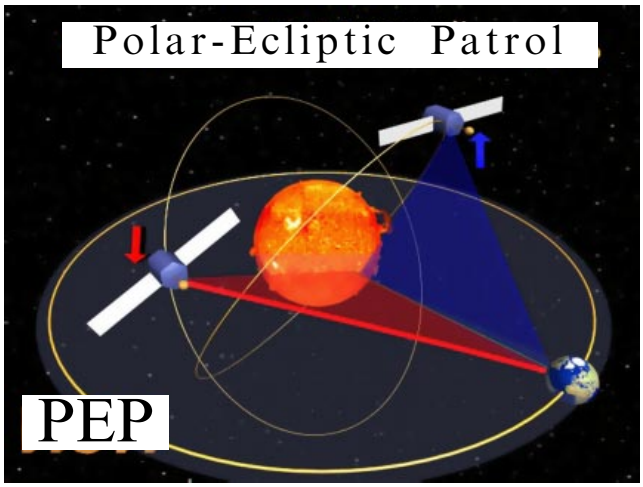

Figure 8. Ballistic scheme of the Polar–Ecliptic Patrol project intended for global solar activity observations and studies of the solar sources of cosmic weather.

or are being developed for the future. These projects are listed in Table 1. The space projects under development are aimed at solving a series of scientific questions posed by contemporary research into the terrestrial ionosphere and magnetosphere, the planets and small bodies of the Solar System, and the Sun and the influence of its activity on the near-Earth space. In the years to come, space investigations in IZMIRAN's research area will grow in importance due to the further broadening of human activity in space and a greater dependence of the space technologies being elaborated on space weather (the state of near-Earth space), the ionosphere, and the geomagnetic field.

References

1. Al'pert Ya L *Usp. Fiz. Nauk* **64** 3 (1958)
2. Al'pert Ya L et al. *Usp. Fiz. Nauk* **65** 161 (1958)
3. Alpert Ya *Making Waves: Stories from My Life* (New Haven: Yale Univ. Press, 2000)
4. Gurevich A V, in *Trudy IZMIRAN* **17** (27) 173 (1960)
5. Gurevich A V *Iskusstvennye Sputniki Zemli* (7) 101 (1961)
6. Al'pert Ya L, Gurevich A V, Pitaevskii L P *Usp. Fiz. Nauk* **79** 23 (1963) [*Sov. Phys. Usp.* **6** 13 (1963)]
7. Al'pert Ya L, Gurevich A V, Pitaevskii L P *Iskusstvennye Sputniki v Razrezhennoi Plazme* (Artificial Satellites in Tenuous Plasma) (Moscow: Nauka, 1964) [Translated into English: *Space Physics with Artificial Satellites* (New York: Consultants Bureau, 1965)]
8. Karpachev A T, in *Entsiklopediya Nizkotemperaturnoi Plazmy* (Encyclopedia of Low Temperature Plasma) Vol. 1–3 *Ionosfernaya Plazma* (Ionospheric Plasma) Pt. 1 (Eds V D Kuznetsov, Yu Ya Ruzhin) (Moscow: Yanus-K, 2008) p. 381
9. Mikhailov Yu M, Mikhailova G A, Kapustina O V *Phys. Chem. Earth C* **25** 93 (2000)
10. Oraevsky V N, Tríska P *Adv. Space Res.* **13** (10) 103 (1993)
11. Ruzhin Yu Ya, Ivanov K G, Kuznetsov V D, Petrov V G *Geomagn. Aeron.* **49** 342 (2009) [*Geomagn. Aeron.* **49** 324 (2009)]
12. Ruzhin Yu Ya et al. *Kosmonavtika Raketostroenie* (4) 66 (2009)
13. Dolginov Sh Sh, Zhuzgov L N, Pushkov N V *Iskusstvennye Sputniki Zemli* (2) 50 (1958)
14. Dolginov Sh Sh, Pushkov N V, in *Uspekhi SSSR v Issledovanii Kosmicheskogo Prostranstva* (Progress of the USSR in Space Research) (Eds A A Blagonravov et al.) (Moscow: Nauka, 1968) p. 173
15. Dolginov Sh Sh et al., in *Itogi Nauki i Tekhniki. Ser. Issledovanie Kosmicheskogo Prostranstva* (Advances in Science and Technology. Ser. Space Research) (Moscow: Nauka, 1965) p. 606
16. Dolginov Sh Sh et al. *Katalog Izmerennykh i Vychislennykh Znachenii Modulya Napryazhennosti Geomagnitnogo Polya Vdol' Orbit Sputnika 'Kosmos-49'* (Catalog of the Measured and Calculated Values of the Modulus of Geomagnetic Field Intensity along the Orbits of 'Kosmos-49') Pt. 1–3 (Moscow: IZMIRAN, 1967)
17. Dolginov Sh Sh et al. *Katalog Izmerennykh i Vychislennykh Znachenii Modulya Napryazhennosti Geomagnitnogo Polya Vdol' Orbit Sputnika 'Kosmos-321'* (Catalog of the Measured and Calculated Values of the Modulus of Geomagnetic Field Intensity along the Orbits of 'Kosmos-321' Satellite) (Moscow: Nauka, 1976)
18. Al'pert Ya L, Sinel'nikov V M *Geomagn. Aeron.* **5** 209 (1965)
19. Chmyrev V M et al. *Geomagn. Aeron.* **26** 2 275 (1986)
20. Ivanov K G, Styazhkin V A, Kharshiladze A F *Geomagn. Aeron.* **29** 304 (1989) [*Geomagn. Aeron.* **29** 265 (1989)]
21. Styazhkin V A et al. *Kosmicheskie Issledovaniya* **36** (1) 108 (1998) [*Cosmic Res.* **36** 103 (1998)]
22. Kuznetsov V D, Zelenyi L M, in *Solnechno-Zemnaya Fizika* (Solar-Terrestrial Physics) Issue 12 *Trudy Mezhdunar. Simpoziuma 'Mezhdunarodnyi Geliofizicheskii God' — 2007: Novyi Vzgluad na Solnechno-Zemnuyu Fiziku, Zvenigorod, 5–11 Noyabrya 2007 g.* (Proc. Intern. Symp. 'International Heliophysical Year' — 2007: New Glance at Solar-Terrestrial Physics, Zvenigorod, 5–11 November 2007) Vol. 1 (Novosibirsk: Inst. Solnechno-Zemnoi Fiziki RAN, 2008) p. 83
23. Dolginov Sh Sh et al. *Geomagn. Aeron.* **1** (1) 21 (1961)
24. Dolginov Sh Sh et al., in *Kosmokhimiya Luny i Planet: Trudy Sovetsko-Amerikanskoi Konf. po Kosmokhimii Luny i Planet* (Lunar and Planetary Cosmochemistry: Proc. Soviet-American Conf. on the Cosmochemistry of the Moon and Planets) (Executive Ed. A P Vinogradov) (M: Nauka, 1975) p. 314
25. Dolginov Sh Sh, Eroshenko E G, Zhuzgov L N *Kosmicheskie Issledovaniya* **6** 561 (1968) [*Cosmic Res.* **6** 469 (1968)]
26. Dolginov Sh Sh et al. *Dokl. Akad. Nauk SSSR* **218** 795 (1974) [*Sov. Phys. Dokl.* **19** 618 (1974)]
27. Riedler W et al. *Nature* **341** 604 (1989)
28. Riedler W et al. *Nature* **321** 288 (1986)
29. Chernikov S P et al. *Datchiki Sistemy* (6) 20 (2009)
30. Kuznetsov V D, Zhitnik I A, Sobel'man I I *Vestn. Ross. Akad. Nauk* **75** 704 (2005) [*Herald Russ. Acad. Sci.* **75** 370 (2005)]
31. Kuznetsov V D, in *Solnechno-Zemnaya Fizika: Resul'taty Eksperimentov na Sputnike KORONAS-F* (Solar-Terrestrial Physics: Results of CORONAS-F Satellite-Borne Experiments) (Ed. V D Kuznetsov) (Moscow: Fizmatlit, 2009) p. 10
32. Chertok I M et al. *Astron. Vestn.* **39** 517 (2005) [*Solar Syst. Res.* **39** 462 (2005)]
33. Kuznetsov V D *Usp. Fiz. Nauk* **176** 319 (2006) [*Phys. Usp.* **49** 305 (2006)]
34. Zhugzhda Yu D, Kuznetsov V D, Lebedev N I, in *Solnechno-Zemnaya Fizika: Resul'taty Eksperimentov na Sputnike KORONAS-F* (Solar-Terrestrial Physics: Results of CORONAS-F Satellite-Borne Experiments) (Ed. V D Kuznetsov) (Moscow: Fizmatlit, 2009) p. 34
35. Kuznetsov V D, in *Pyat'desyat Let Kosmicheskikh Issledovanii: po Materialam Mezhdunarodnogo Foruma "Kosmos: Nauka i Problemy XXI Veka", Oktyabr' 2007 Goda, Moskva* (Fifty Years of Space Research: Materials of the International Forum "Space: Science and Problems of the 21st Century", October 2007, Moscow) (Ed. A V Zakharov) (Moscow: Fizmatlit, 2009) p. 60